UNIVERSITÉ DE STRASBOURG

No d'ordre: 1006

Ecole Doctorale de Physique, Chimie-Physique - ED 182

UDS - IPHC - CNRS/IN2P3

THÈSE

présentée pour obtenir le grade de

Docteur de l'Université de Strasbourg

Discipline: Physique subatomique
Spécialité : Physique des particules

par

Renzhuo WAN

Mesure des mésons neutres dans ALICE avec les calorimètres électromagnétiques dans les collisions pp aux énergies du LHC

soutenue publiquement le 3 Juin 2011 devant le jury:

Directeur de thèse :	Christelle ROY	Directeur de Recherches - IPHC, CNRS, France
Co-directeur de thèse :	Daicui ZHOU	Professeur - CCNU, Wuhan, China
Rapporteur :	Yugang MA	Professeur - SINAP, Shanghai, China
Rapporteur :	Yves SCHUTZ	Directeur de Recherches - CNRS, France
Président :	Serge KOX	Directeur de Recherches - LPSC, CNRS, France
Examinateur :	Xu CAI	Professeur - CCNU, Wuhan, China
Examinateur :	Francis CRENNER	Ingénieur de Recherches - IPHC, CNRS, France
Examinateur :	Nu XU	Professeur - LBNL, USA

No d'ordre: 1006

Doctoral School of Physics, Chemistry-Physics - ED 182

UDS - IPHC - CNRS/IN2P3

THESIS

Presented to obtain the degree of

Doctor of Philosophy in University of Strasbourg

Discipline : Subatomic Physics
Specialty : Particle Physics

by

Renzhuo WAN

Neutral meson measurement in ALICE with EM-calorimeters in pp collisions at LHC energies

Submitted publicly before 3 June 2011 to the jury:

Director of thesis:	Christelle ROY	Director of researches - IPHC, CNRS, France
Co-director of thesis:	Daicui ZHOU	Professor - CCNU, Wuhan, China
Referee :	Yugang MA	Professor - SINAP, Shanghai, China
Referee :	Yves SHUTZ	Director of researches - CNRS, France
President :	Serge KOX	Director of researches - LPSC, CNRS, France
Examiner :	Xu CAI	Professor - CCNU, Wuhan, China
Examiner :	Francis CRENNER	Principal research engineer - IPHC, CNRS, France
Examiner :	Nu XU	Professor - LBNL, USA

Résumé

L'Homme a eu de cesse d'explorer les champs vierges afin de comprendre son environnement. Au 20ème siècle, de grands accomplissements ont été obtenus en physique des particules. Notre connaissance sur la matière fondamentale est telle que nous parvenons donner une description de la matière à l'échelle du quark (10^{-18} m) ce qui en retour, permet de compléter notre connaissance à l' échelle de l$'$Univers. Le Modèle Standard est l'une des théories les plus pertinentes pour prédire les phénomènes nouveaux et expliquer les résultats des expériences. Il explique que les particules fondamentales sont composées par trois familles de quarks, trois familles de leptons et par les vecteurs des quatre forces fondamentales (le photon pour l'interaction électromagnétique, le gluon pour l'interaction forte, les bosons Z^0 et $W^{\pm}$ pour l'interaction faible, le graviton pour la gravitation). Cependant, il reste un certain nombre de puzzles dans le Modèle Standard, comme par exemple l'existence du boson de Higgs et de particules dites super-symétriques ou encore la masse du neutrino. Au-delà de cette description du Modèle Standard, existe-t-il de nouvelles particules inattendues? Répondre à ces questions constitue la grande motivation des physiciens des particules aujourd$'$hui.

Faisant partie du Modèle Standard, la ChromoDynamique Quantique (QCD) prédit une transition de phase, d'une matière hadronique vers une matière dans laquelle les quarks et les gluons seraient déconfinés. Cette matière appelée Plasma de Quarks et de Gluons (QGP) existerait à très haute densité d'énergie et à très haute température et aurait é'é celle sous laquelle se trouvait l'Univers quelques fragments de seconde après le Big-Bang. Sonder ce QGP et en explorer ses propriétés thermodynamiques constituent les principaux objectifs des expériences mettant en oeuvre les collisions d'ions lourds ultra-relativistes grce auxquelles on espère le créer en laboratoire.

En revanche, la matière QCD ne pouvant être sondée directement, les informations sont obtenues en étudiant les distributions des hadrons produits lors des collisions. Plusieurs observables sont proposées pour signer la présence du QGP comme la suppression de la production de hadrons de haute impulsion transverse (haut p_T) traduite sous le terme de *jet quenching*, l'augmentation de la production des particules étranges, la suppression de la production de quarkonia ou encore les écoulements collectifs. Parmi ces observables, j'ai utilisé, pour mon étude, la sonde électromagnétique

afin d'établir des connexions avec la matière dense et chaude car l'interaction faible entre le photon et la matière qu'il traverse peut apporter des informations sur les tout premiers instants de sa création.

Jusqu'à présent, beaucoup de résultats ont été obtenus par les expériences auprès du collisionneur RHIC (Relativistic Heavy Ion Collider) au Laboratoire National de Brookhaven fonctionnant à l'énergie nominale de $\sqrt{s}_{NN} = 200\ GeV$. Les résultats constituent une référence prcieuse pour les expériences auprès du collisionneur LHC (Large Hadron Collider) au CERN. L'expérience ALICE (A Large Ion Collider Experiment) est l'une des quatre expériences implantées auprés du LHC et qui est entièrement dédiée à l'étude des collisions d'ions lourds à une énergie nominale de $\sqrt{s}_{NN}$=5.5 TeV. Les premières données venant des collisions proton-proton à 900 GeV (en 2009) et 7 TeV (en 2010) sont des références nécessaires pour les collisions Pb-Pb à 2.76 TeV (en 2010) et 5.5 TeV (en 2013).

Tout d'abord, les taux de production bruts de mésons neutres via le canal $\pi^0(\eta) \rightarrow 2\gamma$ et $\omega(782) \rightarrow \pi^0\gamma \rightarrow 3\gamma$ ont été estimés à partir de simulations incluant une géométrie réaliste des détecteurs d'ALICE. Cela fournit une référence importante avant d'obtenir les données réelles mesurées par notre expérience. Avec PHOS (Photon Spectrometer), le détecteur de photons d'ALICE, l'étude a montré qu'il était possible de mesurer les particules η et $\omega(782)$ malgré l'acceptance limitée de PHOS.

Je tiens à préciser que j'ai été particulièrement privilégié de participer à l'expérience ALICE avec la disponibilité des premières données collectées alors que j'étais en doctorat depuis un an et demi : cela m'a donc permis d'enrichir ma thèse en présentant des analyses avec des données réelles et non pas seulement des données simulées. En outre, en m'investissant lors des prises de données à des postes dédiés à l'acquisition des données (DAQ pour Data Acquisition), à la mise en oeuvre des systèmes de déclenchement (CTP pour Central Trigger Processing) et au système de contrôle des détecteurs (DCS pour Detector Control System), j'ai pu appréhender le mode de fonctionnement du LHC et sa complexité.

Au début des prises de données, il a ensuite été nécessaire de se concentrer sur la compréhension des détecteurs de leur mode de fonctionnement afin d'obtenir des résultats convaincants. Ainsi, la chaine globale de traitement des données, des données brutes aux analyses de physique spécifiques, est présentée, incluant la description des algorithmes de clustérisation, de calibrage des détecteurs ou encore l'identification des particules.

Ce travail de thèse présente la mesure des mésons neutres avec les calorimètres électromagnétiques d'ALICE (PHOS et EMCal). En raison des conceptions différentes des détecteurs, différentes stratégies pour extraire les mésons neutres sont examinées : la technique de la masse invariante, l'analyse de la forme de la gerbe ou encore la méthode d'isolation par coupures. La raison du besoin de méthodes différentes est la granularité du détecteur: lorsque les clusters laissés par le passage de particules commencent à se chevaucher, il n'est plus possible de les séparer et la particule est alors identifiée selon les paramétres de la forme de la gerbe qui en résulte. A très haute impulsion transverse, la méthode d'isolation par coupures a été développée pour identifier les photons directs et ainsi extraire les pions neutres.

Les problèmes de calibrage et de problèmes de géométrie du calorimètre EMCAL ont nécessité des études plus poussées. Davantage de résultats obtenus avec PHOS ont été inclus dans cette analyse. A ce stade, mes résultats ne sont pas définitifs mais je les présente dans leur état actuel, avec l'approbation de la collaboration ALICE.

Avec les statistiques actuelles correspondant aux collisions proton-proton à 7 TeV, environ 390 millions d'événements de biais minimum ont été analysés. En utilisant la technique de la masse invariante, la distribution des pions neutres a été obtenue avec des impulsions transverses atteignant 25 GeV/c mesurées avec PHOS. En revanche, avec EMCal, les pions neutres ont pu être mesurés jusqu'à des impulsions atteignant seulement 15 GeV/c en raison des chevauchements de clusters.

Le pic correspondant aux particules η a pu être extrait et celles-ci ont donc pu être mesurées jusqu'à des impulsions transverses de 10 GeV/c. Toutefois, cette analyse n'est pas incluse dans cette thèse. Pour les particules ω recherchées dans le canal $\pi^0\gamma$, elles n'ont pu être mises en évidence clairement en raison de l'acceptance limitée du détecteur et du dysfonctionnement de canaux électroniques. Les données de EMCal ont pu être exploitées et cette particule identifiée grâce à la mise au point d'une technique particulière. La méthode présentée ici a été mise au point par simulations puis validée avec les données réelles.

Pour la correction des spectres bruts, nous avons pris en compte les effets d'acceptance des détecteurs et d'efficacité de reconstruction à partir de simulations utilisant un méson neutre par événement. Les erreurs systématiques sont estimées selon le calibrage en énergie, la non-linéarité de la réponse des détecteurs, les canaux électroniques défectueux et les pertes de pions neutres. La section efficace finale de production des pions neutres est comparée aux prédictions des modèles.

Je tiens à souligner qu'il s'agit de la première mesure de mésons neutres et qu'elle est cruciale pour le calibrage des calorimètres électromagnétiques. Elle est aussi reliée à beaucoup d'analyses de physique, comme l'accès aux photons directs, les mesures d'écoulement collectif, la physique des jets, etc. Au cours de cette année, ALICE va continuer de prendre des données avec des collisions proton-proton et PbPb à la luminosité nominale.

Enfin, je conclurai en disant que c'est la fin de mes études de doctorat mais juste un commencement de la physique d'ALICE.

Mots-clés

Plasma de Quarks et de Gluons, LHC, Expérience ALICE, Mesure de mésons neutres

摘 要

人类在探索未知领域的步伐从来没有停止过，试图理解人类本身和我们所生活的宇宙。在20世纪，粒子物理领域所取得的巨大成就，使我们对微观世界基本组分的认识已经达到夸克的层次（$r \sim 10^{-18}$m），这种发展反过来也促进了人类对宇宙起源等问题的理解。标准模型（SM）是上个世纪颇为成功的理论之一，它成功的预测了新的唯象，并对诸多实验结果给出了合理的解释。它解释了宇宙中的基本组分粒子是由3代夸克，3代轻子和4个传递相互作用的粒子（光子传递电磁相互作用，胶子传递强相互作用，$W^{\pm}$，Z^0玻色子传递电弱相互作用）。然而，仍然有许多困惑，比如是否存在希格子玻色子和超对称粒子，中微子质量之谜等标准模型框架之内或之外问题，有待解决。此外，宇宙中是否存在我们没有预测到的新的粒子，夸克或轻子？这些问题是当前理论和实验物理学家科研探索的第一推动力。

作为标准模型一部分，格点量子色动力学（LQCD）预测在高温、高密的环境下，会有一个从强子相到解紧闭的夸克胶子等离子（QGP）的相变过程。从而，探寻夸克胶子等离子体存在的证据，并理解其相变热动力学演化过程是当前超相对论重离子碰撞的重要物理目标之一。此外，通过夸克胶子等离子体的研究将会对宇宙天文学的观测发现也起到重要作用。然而，在实验室除了通过末态强子分布的间接研究，并没有直接观察和探测致密的夸克胶子物质的途径。其中，已经发展和建立的观测途径有：通过高横动量强子谱和夸克偶素产额压低，喷注淬火现象，奇异粒子产额增强，动力学演化的集体流行为等。在这些可观测量中，由于光子是电磁粒子，它会弱耦合与致密的夸克胶子等离子体，从而携带其产生时刻的热动力学信息，进而通过中性粒子谱压低，直接光子产额增强，光子-强子关联等物理测量建立与致密物质属性的联系。

目前为止，在美国布鲁克海文国家实验室（BNL）的相对论重离子对撞机实验（RHIC），最高能量为200 *GeV*，已经发表了大量的关于致密物质的研究成果，为正在运行的欧洲核子中心（CERN）上的大型强子对撞机（LHC）实验提供了重要的理论和实验参考。大型重离子对撞机实验（ALICE）是LHC上的四大重要实验之一，致力于在最高质心能量为5.5 *TeV* 下的重离子碰撞物理研究。实验运行早期的900 *GeV*（2009年底）和7 *TeV*（2010年）的质子-质子碰撞数据是重离子铅-铅在质心能量为2.76 *TeV*（2010年底）和5.5 *TeV* 碰撞的必要条件。在实验运行之前，结合探测器真实的几何配置，我们首先估算了中性粒子谱的产额，该分析为ALICE电磁量能器（光子谱仪PHOS和电磁量能器EMCAL）的物理分析提供了依据。同时也证明了PHOS通过光子衰变道重建η和ω的可行性。

可以说我很幸运能够在博士期间的最后一年半时间里参与ALICE数据获取和物理分析，也使得该博士论文不再是完美的模拟结果，而是充满实验气息的物理分析。同时，参加ALICE的数据获取（DAQ），中心触发选判处理（CTP）和探测器控制系统（DCS）值班的经历，也使我更多的接触实验控制过程，从而理解LHC是如何工作以及它的复杂性。

然而，实验毕竟也不像唯象研究，通过一系列近似和参数调整，唯象研究总能得到预期想要的结果去解释实验结果。尤其在实验的早期阶段，我们应该投入更多的精力去磨合和理解探测器，进而得到令人信服的物理结果。因此，从探测器获取的原始数据到物理分析数据这样的数据处理过程，通过比较模拟和实验数据，我们进行了认真的检查和研究，包括簇射重建，探测器校正，粒子鉴别等。

本论文研究了利用ALICE电磁量能器来重建中性粒子谱。由于PHOS和EMCAL不同的探测技术和设计参数，依赖于所探测的中性粒子的横动量大小，我们研究了三种分析策略：不变质量分析，簇射形状分析和孤立截断。在低的横动量区间，从中性粒子的衰变光子能够很好的区分，从而用可以用不变质量分析重建中性粒子谱；在中间横动量区域，衰变光子开始叠加，借助于簇射形状仍然能够鉴别；在很高的横动量区间，衰变光子开始完全叠加，而不能展开，运用孤立截断这种间接方法可以提取中性粒子谱。

由于EMCAL探测器仍然存在校正和几何方面的问题，该论文更多的包含了关于PHOS的物理分析。我不打算声称所有的结果都是最终的物理结果，只是呈现我的科研贡献和收获。

从目前的质子-质子在7 *TeV* 下的碰撞数据，我们分析了大约390兆的最小无偏事件。运用不变质量分析，对PHOS来说，我们可以提取到横动量为25 *GeV/c* 的π^0谱，而对EMCAL由于簇射叠加和展开算法的限制，目前只能提取到横动量为15 *GeV/c*。同时我们也测量到η的分布到10 *GeV/c*，本论文并没包含更多具体的分析。关于衰变道ω->π^0γ，对PHOS由于统计量和接受度的原因，仅仅在横动量>4 *GeV/C*观察到明显的信号。对于EMCAL，借助于特殊的簇射展开算法，在横动量区间[4, 6] *GeV/c*和[6, 8] *GeV/c*观察到清晰信号存在，但欲提取ω谱仍需要更深一步的研究。新的ω->π^0γ重建方法假定高横动量的簇射为π^0，而不借助与簇射的展开算法，在模拟研究中证明了其可行性。

在对原始中性粒子谱的修正中，我们将探测器的接收度和重建效率结合在一起，用均匀分布的单π^0事件进行完整的模拟。从探测器的绝对能量校正以及非线性响应，坏道挑选的不确定性，由于光子转化造成π^0丢失以及来自顶点外的非物理效应的π^0等方面估算系统误差，最终给出实验上的不变散射截面分布，并和理论进行了比较。

我想强调的是，中性粒子谱（比如：π^0）的测量对早期的探测器校正至关重要。并且是任何光子物理分析的基础，比如直接光子提取，集体流，喷注物理等都直接相关。接下来，ALICE将达到预期设计的亮度，并继续采集质子-质子和铅-铅碰撞数据，更多的物理结果即将发表。

“完成该博士论文意味着博士生涯的结束，但却是整个ALICE物理分析的开始”。

关键词

夸克胶子等离子 大型强子对撞机， ALICE实验，中性粒子谱测量

Abstract

Our human being has never been stopping in the exploration of the virgin field in understanding ourselves and our surroundings. In the 20^{th} century, great achievements have been obtained in particle physics. Our knowledge on the fundamental matter has reached the quark level ($r \sim 10^{-18} m$), which in turn improve our understanding on the origin of universe. Standard Model is one of the best theories to predict the new phenomena and explain the experiment results in these fields. It explains that the fundamental particles are 3 generations of quarks, 3 generations of leptons and four force carriers (γ-electromagnetic interaction; gluon-strong interaction; Z^0 and $W^{\pm}$-weak interaction). However, there are also still a number of puzzles remaining, such as existence of Higgs boson and super-symmetry particles, neutrino mass puzzle, which within or beyond the Standard Model, need to be answered. Besides, whether there are new particles/quarks/leptons unexpected? These questions are the first driving force to motivate physics scientists.

As a part of Standard Model, Lattice Quantum ChromoDynamics (lQCD) predicts a phase transition from hadronic matter to the deconfined QCD matter called Quark Gluon Plasma (QGP) at extreme high energy and density. Probing of the QGP and exploring its thermal properties and dynamic evolution are the main objectives in ultra-relativistic heavy-ion collisions. In addition, the probe of QGP also plays an important role in direction of astrophysical observation. However, there are no direct way to measure the QCD matter except for the measurement of final hadron spectrum. Several observables have been well built, such as the high p_T hadron suppression and jet quenching, enhancement of the strangeness particles, suppression of the quarkonia production and the hydrodynamic collective flow etc. Among these observables, in this study, electromagnetic probe is employed to build the connections to the hot-dense matter. Because the interaction between the photon and medium is weak when the photon goes through thus can carry the origin information when it was created.

Up to now, a great of results have been obtained at the Relativistic Heavy Ion Collider (RHIC) at Brookhaven National Laboratory with a top center-of-mass energy 200 GeV. The results are critical reference for the experiments at Large Hadron Collider (LHC) at CERN. A Large Ion Collider Experiment (ALICE) is one of the four main experiments at the LHC, which is dedicated on the heavy-ion collisions at

a top center-of-mass energy $\sqrt{S_{NN}} = 5.5\ TeV$. The initial runs with proton-proton collisions at 900 GeV (2009) and 7 TeV (2010) are useful reference points for the Pb-Pb collisions at a $\sqrt{S_{NN}}$ of 2.76 TeV (2010) and 5.5 TeV (2013). Firstly, the raw yield of neutral mesons by $\pi^0(\eta) \rightarrow 2\gamma$ and $\omega(782) \rightarrow \pi^0\gamma \rightarrow 3\gamma$ with the realistic geometrical configuration were estimated. It gives us an important reference before the ALICE data-taking at different LHC energies. For PHOS, the study proves the possibility to measure the η and $\omega(782)$ despite of its limited acceptance.

I would like to say it was my fortunate that I caught the moment of ALICE data-taking in the course of my PhD, which makes the thesis a bit rich of "EXPERIMENTAL", and not only of "SIMULATION". Besides, from the experience of shifts on Data Acquisition (DAQ), Central Trigger Processing (CTP) and Detector Control System (DCS) I get to know how the LHC works and its complexity.

However, the experiment is not like phenomenology which can get the expected results as they want by adjusting the parameters properly. Especially at the early stage of experiment, we need to understand the detectors and then to get the convincing physics results. Thus the data processing chain from raw data to physics analysis oriented are studied and presented, which includes the clusterization, detector calibration and particle identification.

In this thesis, the neutral mesons measurement with ALICE electromagnetic calorimeters (PHOS and EMCAL) at the LHC is presented. Depending on the different technical design of PHOS and EMCAL and their momentum reach, the strategies of the neutral mesons extraction by invariant mass analysis, shower shape analysis and isolation cut method are studied. The main reason is due to the detector granularity. Clusters start to merge and maybe misidentified as single cluster in high multiplicity environment, as well as for high p_T π^0. Cluster unfolding algorithm and shower shape parameters allow us to separate γ and π^0 at intermediate p_T. At very high p_T, the isolation cut method was developed to identify the direct photons, and also used for the extraction of neutral pion indirectly.

For EMCAL, we need further investigations on the calibration and geometrical problems at the moment. More results with PHOS are included in the current analysis. Here I do not intent to claim that all the results are final results, but present my contributions and what I obtained.

From current statistics with pp collisions at 7 TeV, $\sim$ 390 million min-bias events are analyzed. By using the invariant mass analysis, π^0 spectrum is extracted to a p_T range of 25 GeV/c with PHOS. While for EMCAL, due to the cluster overlap it can measure the π^0 spectrum with p_T range to 15 GeV/c. The η peak is also can be observed and measured up to 10 GeV/c, but not included in this analysis. As for the $\omega \rightarrow \pi^0\gamma$, clear peaks can be observed at $p_T > 4\ GeV/c$ in PHOS. While for EMCAL it can be seen at high $4 < p_T < 8\ GeV/c$ with the help of special unfolding algorithm. An additional method with the assumption that high p_T clusters are π_0 without cluster unfolding was developed for ω measurement, which had been studied in simulation and being validated in real data.

For the corrections of the raw spectrum, we take into account the geometrical

acceptance and the reconstruction efficiency together by a full simulation with an uniform single π^0 per event. The systematic uncertainties are estimated due to the absolute energy scale calibration, non-linearity response of the detector, bad channels and π^0 loss. The final π^0 production yield are obtained. The scaling behavior of x_T and m_T are studied by comparing the world-wide data set. Finally, π^0 cross section are compared with QCD next-leading-order calculation.

What I want to emphasis is that the first measurement of the neutral mesons are crucial for the calibration of electromagnetic calorimeters. It is also related to almost all the photon physics, such as direct photon excess, flow measurement and jet physics etc. In the coming years, ALICE will continue with the data taking with pp and PbPb collision and the LHC will reach the designed luminosity. More statistics and rich physics results will come forth.

Finally, I would like to say "it is an accomplishment of my PhD study, but just a beginning of ALICE physics activities."

Keywords

Quark Gluon Plasma, LHC, ALICE experiment, Neutral meson measurement

Contents

List of Figures

List of Tables

Chapter 1

Introduction of high energy physics

The Large Hadron Collider (LHC) experiment at CERN is opening a new TeV energy era. The physics orientation is to challenge key existing unsolved problems and, meanwhile, to explore new physics. In the introduction, the theory background in particle physics is shortly introduced. Various observables are summarized, which will lead us to the conclusion of understanding to the QCD matter. Finally, the scope of the thesis is presented.

1.1 Standard model

In the past century, the development of theories and experiments in particle physics has resulted in a remarkable insight into fundamental structure of matter and the connection with our early universe [1–5]. To our current knowledge, these fundamental particles are twelve building blocks of six quarks and six leptons, which are governed by four fundamental forces (Fig.1.1). The Standard Model [6–9] built in the early 70s, is a theoretical framework to describe the elementary building blocks and their interactions. It has successfully explained considerable set of experimental results and predicted a lot of phenomena. One of the great achievements is the unification of the electromagnetic and the weak forces into the electroweak force. However, there still are some open issues to be answered, such as the origin of the Gravity, the existence of the Higgs boson, finding of super-symmetry particles, the neutrino mass puzzle etc. The ongoing experiments at the Fermilab, RHIC, LHC etc, are now dedicating on these measurements. Within or beyond the framework of Standard Model, a theory of everything is being developed [3].

1.2 Quantum ChromoDynamics (QCD)

As a part of Standard Model, QCD [10] is the best theory describing the behavior of nuclear matter and explaining how the quark and gluon make up a hadron and their interactions via the strong color force. It obeys to the principles of a relativistic Quantum Field Theory (QFT) with a non-abelian gauge invariance SU(3). In QCD,

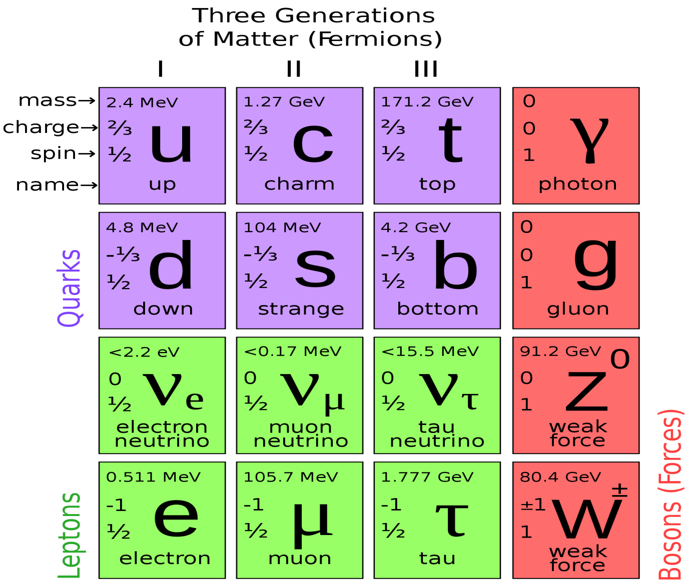

Figure 1.1: Six quarks, six leptons and four force carriers are the elementary particles in our current universe.

the Lagrangian is defined as:

$$\mathcal{L} = -\frac{1}{4}F^a_{\mu\nu}F^{\mu\nu}_a - \sum_f \bar{\psi}^f_\alpha(i\gamma^\mu\partial_\mu + m_f - g\gamma^\mu A_\mu)^{\alpha\beta}\psi^f_\beta, \tag{1.1}$$

with

$$F^a_{\mu\nu} = \partial_\mu A^a_\nu - \partial_\nu A^a_\mu - g f^a_{bc} A^b_\mu A^c_\nu, \tag{1.2}$$

where A^a_μ is the gluon field of color a (1, 2, ..., 8); ψ^f_α is the quark field of color α (1, 2, 3) and flavor f; while the input bare quark masses are given by m_f. Different techniques have been developed to deal with it, such as perturbative QCD (pQCD), lattice QCD, Ads/CFT, effective field theory etc.

A number of evidences have presented some interesting properties, such as the confinement and asymptotic freedom, phase transition from hadronic matter to quarks and gluons, chiral symmetry restoration.

1.2.1 Confinement and asymptotic freedom

In QCD theory, at low-energy any strongly interaction system at zero temperature and density must be a color singlet at distance scale larger than $1/\Lambda_{QCD}$. Also no individual quark has been observed experimentally yet so far. It was concluded that all quarks are confined into hadronic matter and interact by exchanging gluons. This is so called the color-confinement. Correspondingly, when the distance between two quarks increase, the interaction force will increase infinitely so that at some stages new quark pairs are formed. And they never get away from the bound of nucleon. Under the extremely high temperature and pressure, the force between the quarks becomes weak. This is the asymptotic freedom [11, 12], which was discovered by David Gross, Frank Wilczek, and David Politzer in 1973 (Winners of the Nobel prize in Physics in 2004). It describes the strong interaction by a running coupling constant α_s,

$$\alpha_s(Q) = \frac{12\pi}{(33 - 2N_f)lnQ^2/\Lambda^2_{QCD}} \tag{1.3}$$

where N_f is the number of flavors and Λ is QCD scale which strong depend on the four-momentum transfer Q^2. Under larger four-momentum transfer $Q^2 \gg \Lambda^2$, the interaction between quarks and gluons becomes weak.

1.2.2 Chiral symmetry restoration

In QCD Largrangian, Chiral symmetry is an axial vector symmetry of left-handed and right-handed parts of Dirac field in the limit of vanishing quark masses. Due to finite u, d quark masses, Chiral symmetry is spontaneously broken in nature. As a consequence, it leads to the production of Goldstone-boson as pion, and splitting of scalar/pseudo-scalar and vector/axial-vector particles. At extreme high energy and density environment, the chiral symmetry restoration is expected in Quark Gluon Plasma phase. Creating a system with restored chiral symmetry in heavy ion collisions is one of the main objectives, as well as a significant condition to locate the phase transition.

1.2.3 Phase transition from hadrons to quarks and gluons

As a consequence of quark asymptotic freedom, when the hadronic system lies beyond critical energy and density, the deconfinement from colorless hadronic constituents to colored quarks and gluons will take place. To study this critical behavior, the pQCD regime is not available any more due to the dominant long-range correlations and multi-particle interactions. Within the lattice formulation of QCD, the critical behavior can be studied numerically. The pressure is given in the Stefan-Boltzmann form [14, 15]

$$p = cT^4[1 - a(\frac{m_{th}}{T})^2] = cT^4[1 - ag^2(T)] \tag{1.4}$$

and the energy density

$$\epsilon = 3cT^4[1 - ag^2(T) - \frac{2am_{th}}{3}(\frac{dg}{dT})], \tag{1.5}$$

where c and a are color and flavor dependent and m_{th} is an effective thermal masses of quarks and gluons. As shown in Fig. 1.2(a), the ϵ/T^4 changes sharply at above

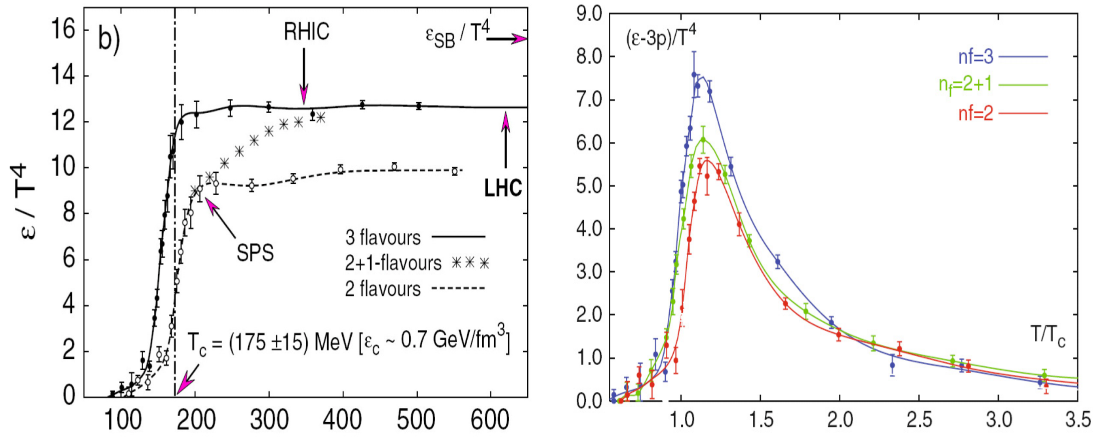

(a) Energy density

(b) Interaction measure ($(\epsilon - 3p)/T^4$)

Figure 1.2: The energy density from lattice QCD calculation. [13]

the critical temperature, and from Fig. 1.2(b) we can see that there are still some strong interaction region between $T_c < T < 2T_c$. Because there are no dimensional parameters in QCD with the limit of massless quarks, the value of transition temperature only can be determined by some other physics observables. Lattice QCD get this value of $T_c = 190 \pm 10\ MeV$ by fine structure charmonium calculation [16]. Latest conclusion from experiment results present the critical temperature for the QCD phase transition is $175\pm^1_7\ MeV$ [17].

So we get the conclusion that above the critical energy $170 \sim 200\ MeV$ and a energy density above $1\ GeV/fm^3$, the deconfinement could occur abruptly [18].

1.2.4 Phase diagram

Fig. 1.3 shows a typical QCD phase diagram state of the art as a function of the system temperature and baryon-chemical potential.

- At low temperature (zero temperature) and high chemical potential (at a few times than nuclear matter), the attractive interactions between quarks will lead to the formation of the colored bosonic diquark pairs and Cooper pairs of QCD from deconfined phase. So that the diquarks condense at low temperature to become a color superconductor.

- At intermediate temperature and low chemical potential, a first order phase transition from hadronic matter to plasma will happen with typical properties of deconfinement and chiral symmetry restoration.

- Critical point is an end point of first order and a start point of second order, which is one of our main goals both for theory and experiment.

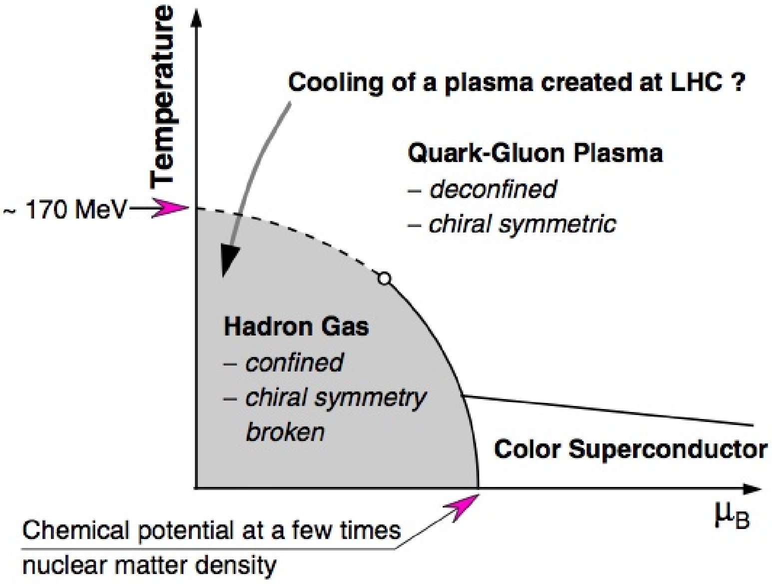

Figure 1.3: QCD phase diagram.

- At extreme high temperature and almost zero chemical potential, some arguments think it as a second order phase transition, while others show the evidences as a crossover with a smooth and continuous transition.

Although a number of results had been obtained by the fluctuation and flow measurements from RHIC since 2000 [19, 20], there are still lots of questions to be addressed. The ongoing STAR experiment at RHIC are now dedicated on the energy scan from several GeV to hundred GeV to locate the critical point and boundary of the first order transition.

The experiments at the LHC (ALICE, ATLAS and CMS) are moving on the TeV era to address the questions above. ALICE is one of the main experiments designed for the heavy-ion collisions at $\sqrt{S_{NN}} = 5.5\ TeV$. It will step into extreme high energy and density with almost zero chemical potential, where the phase transition from hadronic matter to plasma is expected to take place.

1.3 Probe of the QGP

Probing the quark gluon plasma and exploring its properties are among the main physics objects in current high-energy physics field. The matter is also expected to exist in soon after of the big bang of the universe, and could be observed nowadays in the compact neutron stars by astrophysical observation [4]. It drives us to develop the theory and experimental methods, to expand our understanding in the connection between the micro- with macro-world.

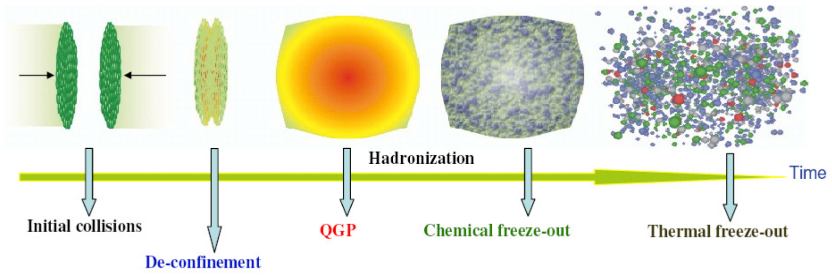

Figure 1.4: Schematic view of the time evolution of the heavy-ion collision system.

1.3.1 The ultra-relativistic heavy-ion collisions

The ultra-relativistic heavy-ion collisions is an unique way to produce the hot and dense matter in laboratory. A schematic view of the time evolution of the heavy-ion collision is shown in Fig. 1.4 and it follows

1) Initial collisions and the formation of the ”fireball” in limited space-time volume;

2) Deconfinement evolved from pre-equilibrium to thermal QGP;

3) Transition from thermal QGP to chemical equilibrium, as well as a mixed phase. It produces transient massive effective quarks, while free gluons are disappearing.

4) Hadronization, when quarks are combined into hadrons with the effective and strong interaction. Then the unstable hadrons will decay into stable and final detectable particles.

Recent surveys from the four experiments at RHIC are unanimous in their conclusion that a new form of matter has been created. This matter is very dense, opaque and exhibits a high level of collectivity which has largely been attributed to the expansion of a partonic phase. It is inconsistent with naive expectations based on a weakly-interacting (gas-like) Quark Gluon Plasma (wQGP), while it is best described in terms of a so-called strongly interacting QGP (sQGP) constituting an almost perfect fluid [21,22]. Thus, a discovery has been made in a qualitative sense, but the properties of this new state of matter remain under intense debate. These arguments are being investigated at the underway experiments at the LHC energy region.

1.3.2 Observable

There is no direct way for the detection of the early dynamic evolution for phase transition, QGP formation and the new particle productions, but by the final physics observables [23]. The most relevant ones are summarized briefly below:

High p_T hadron suppression and jet quenching

One of the most promising signatures of the QGP are the high p_T hadron spectrum suppression and jet quenching measurements [24], which have been discovered at RHIC (for example: [25–27]). By comparing the results for a given observable measured in AA collisions to those measured in pp or pA collisions, thermodynamical properties (such as temperature, energy) and transport properties (such as viscosities, diffusivities and conductivities) of the QCD matter can be deduced theoretically or using phenomenology. For example, the nuclear modification factor is defined as the ratio of yield in AB[1] to pp collisions normalized by the number of binary collisions

$$R_{AB} = \frac{d^2N_{AB}/dp_T dy}{< T_{AB} > d^2\sigma_{pp}/dp_T dy}, \tag{1.6}$$

where $< T_{AB} >$ is the nuclear overlap function [28]. The observation of R_{AB} distribution with suppression or enhancement relative to a reference value of 1 will be directly linked the properties of the QCD matter and the realistic space-time evolution for the collision system.

Especially for the high p_T particles (far larger than the QCD scale $\Lambda_{QCD} \sim 0.2$ GeV) and jet production, those are useful tool for the tomography study of the hot-dense matter for the reasons that

1) they originate from the initial hard processes with large momentum transfer Q^2, and are coupled directly to the fundamental QCD degrees of freedom;

2) they are produced in a short time-scale thus can go through the hot-dense medium and carry its thermal information;

3) the production rate can be theoretically predicted by using of pQCD.

The well established measurements via the suppression of the high p_T hadrons spectrum, the di-hadron azimuthal correlations and $\gamma-$hadron correlation have exhibited a number of interesting results. The nuclear modification factors are shown in Fig. 1.5(a) on various particles measured by PHENIX, and in Fig. 1.5(b) on the latest measurement of inclusive charged particles by ALICE. The suppression at high p_T for hadrons are observed. In central collisions, compared with STAR and PHENIX (in Fig. 1.5(b)), charged particle R_{AA} is smaller than at lower energies, which provide the evidences for the strong parton energy loss and large medium density formed at the LHC.

Fig. 1.6 shows an example of dihadron correlations measured at STAR [31–33] in 0-12% central AuAu collisions with $p_T^{assoc} < 1.0$ GeV/c and $4 < p_T^{trig} < 6$ GeV/c. In near side, the leading/triggered particles shows a strong correlation with a narrow $\Delta\phi$ Gaussian peak to the surrounding hadrons. In the away side the correlation becomes loose due to their original parton jet transverse a larger distance in the hot-dense

---

[1] Here A, B denote proton or heavy nuclei.

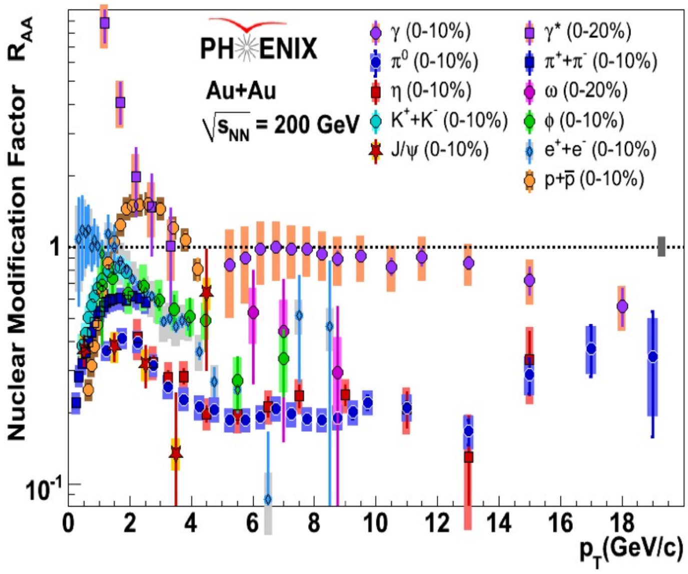

(a) RHIC, R_{AA}

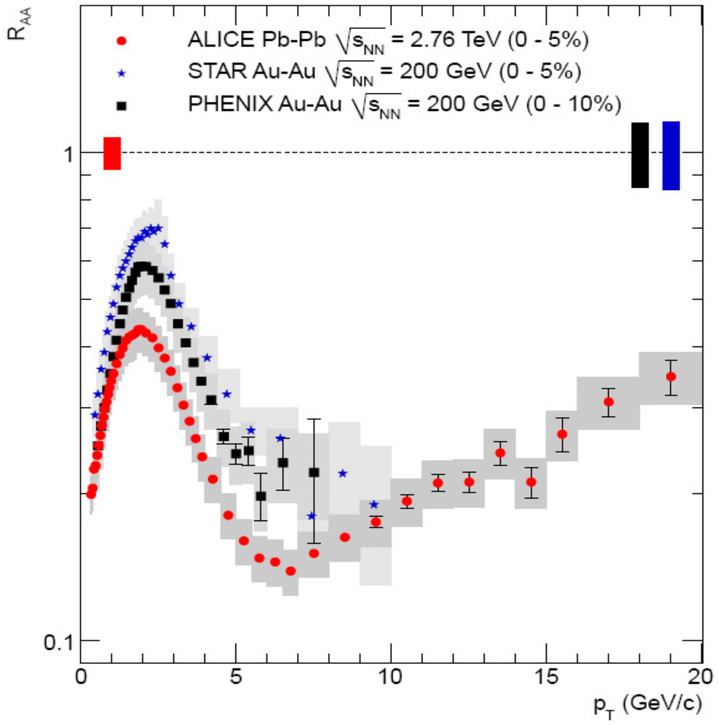

(b) LHC, ALICE R_{AA}

Figure 1.5: Nuclear modification factor from RHIC (a) [29] and the latest results on the inclusive charged particles from ALICE (b) [30], compared to those of STAR and PHENIX experiments.

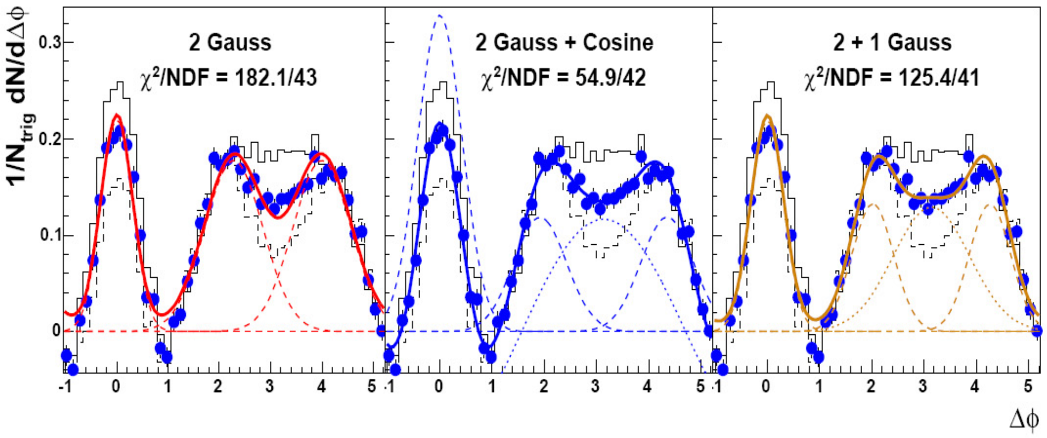

Figure 1.6: The dihadron correlations [31, 32] at STAR in 0-12% central AuAu collisions with $p_T^{assoc} < 1.0$ GeV/c and $4 < p_T^{trig} < 6$ GeV/c. The shapes are fitted by three fitting functions to indicate the uncertainties on the background subtraction.

medium. Mixing events and the mathematical fitting methods were used to subtract the underlying event or flow contribution. In the away side, double-peaked shapes were observed from the measurement (also in [34]). There are hot arguments on the explanation, such as the Mach-cone effect [35], Cerenkov gluon radiation [36], large angle gluon radiation [37] and jet deflection [38].

Besides, by using the high p_T direct photon as a trigger particle to make the $\gamma - hadron$ correlation is also a super relevant probe [39]. But there are great challenges from prompt photon identification and π^0 background subtraction. RHIC has presented their first results [40], however, there are large systematic uncertainties. This would be further improved at the LHC.

The suppression of high p_T hadrons or jet spectra demonstrate that the partons or hadrons will experience the energy loss (ΔE) when going through the QCD matter. The energy loss depends on the particle type (mass m and energy E), medium properties (temperature T, particle-medium coupling α, medium thickness/length L), which usually characterized by the below properties:

- the mean free path of the parton going through the medium $\lambda = 1/(\rho\sigma)$, where ρ is the medium density and σ is the integrated cross section of parton-medium interaction,
- the number of scattering in the medium $N = L/\lambda$;
- the Debye mass $m_D(T) \sim gT$ (g is the coupling parameter), which characterizes the lowest momentum exchange with the medium;
- the transport coefficient $\hat{q} \equiv m_D^2/\lambda$. It stands for the scattering power of the medium by the average transverse momentum squared transfer to the traversing particle per unit path length.

A number of jet quenching models, such as the BDMPS (Baier, Dokshitzer, Muller, Peigne and Shiffer) [41–44], LCPI (Light Cone Path Integral by Zakharov) [45], ASW (Armesto, Salgado and Wiedemann) [46–49], GLV (Gyulassy-Levai-Vitev) [50–54], HT (Higher Twist) [55–58], AMY (Arnold-Moore-Yaffe) [59–62], had been developed for qualitative study of the mechanism of the collision and radiation energy loss.

Direct photon excess

Direct photons originate from the early collision directly and thus they carry the original information of the collision evolution [2]. The excess of direct photon information is a useful tool to investigate the formation of the GQP. The direct photon spectrum at low p_T can reveal the thermal properties of QCD matter. It is a challenge to subtract the hadronic decay photons at low $p_T < 2$ GeV/c, but this can be achieved by the measurement of photon conversion. The overview of the direct photon production and existing experimental results can be found in [63–67].

Hydrodynamic collective flow

The dynamical evolution of the thermal equilibrium is studied by the observables of collective flow, which is expressed by a Fourier series of azimuthal momentum distribution [68, 69]:

$$\frac{dN}{d\phi} = \frac{N}{2\pi}[1 + 2\nu_1 cos(\phi) + 2\nu_2 cos(2\phi) + ...], \tag{1.7}$$

where ϕ is the azimuthal angle measured from the reaction plane[3]. And ν_n are the Fourier coefficients of nth harmonics:

$$\nu_n = \frac{\int d\phi cos(n\phi \frac{dN}{d\phi})}{\int d\phi \frac{dN}{d\phi}} =< cos(n\phi) > . \tag{1.8}$$

These coefficients reflect the initial collisions impact on geometry through the non-isotropies in particle emission created by the partonic pressure gradients. Usually, ν_0 is "radial flow" as Hubble expansion, which is sensitive to the mixed phase conditions characteristic of a first order parton-hadron phase transition. ν_1 is the "directed flow", which is significant near the beam rapidity region but vanish around the mid-rapidity region because of the symmetric collision geometry. Finally, ν_2 is the "elliptic flow", which is measured at the mid-rapidity region and reveal the initial spatial distribution via the final anisotropic momentum distribution.

At RHIC, large elliptic flow has been considered as one of the key experimental discoveries [69, 75]. Theoretical models, based on ideal relativistic hydrodynamics

---

[2] More details in Chapter 2.

[3] There are several methods to measure the reaction plane, such as Lee-Yang Zero method [70–72], event plane method [69, 73], cumulant method [74] etc.

with a QGP equation of state and zero shear viscosity, fail to describe elliptic flow measurements at lower energies but describe RHIC data reasonably well [76]. Theoretical arguments, based on the AdS/CFT conjecture, suggest a universal lower bound of $1/4\pi$ for the ratio of shear viscosity to entropy density. Recent model studies incorporating viscous corrections indicate that the shear viscosity at RHIC is within a factor of ∼5 of this bound [77, 78].

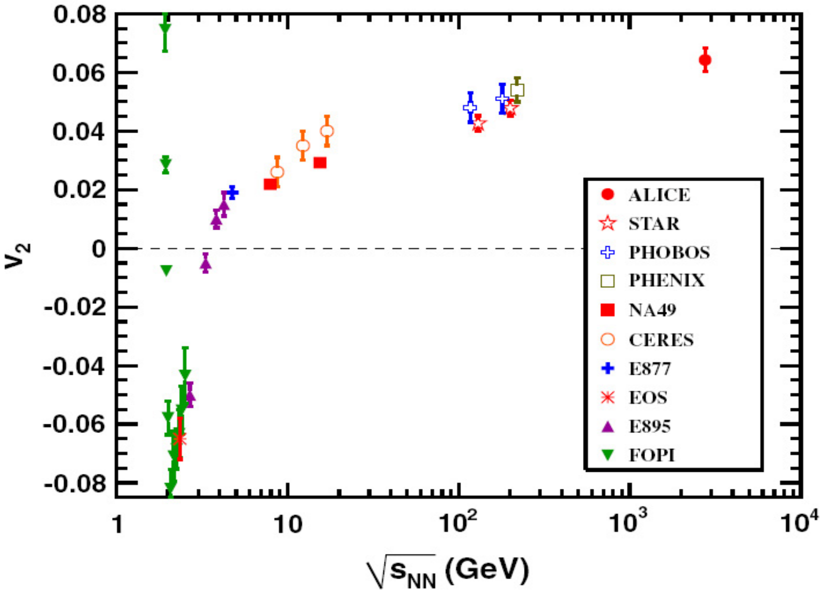

Figure 1.7: Integrated elliptic flow at 2.76 TeV in PbPb 20%-30% centrality with ALICE compared with the results from other experiments at lower energies at similar centralities [79].

The pure hydrodynamic models and models which combine hydrodynamics with a hadron cascade afterburner (hybrid models) that successfully describe flow at RHIC predict an increase of the elliptic flow at the LHC ranging from 10% to 30%, with the largest increase predicted by models which account for viscous corrections at RHIC energies. In models with viscous corrections, ν_2 at RHIC is below the ideal hydrodynamic limit and therefore can show a stronger increase with energy. In hydrodynamic models the charged particle elliptic flow as a function of transverse momentum does not change significantly, while the pt-integrated elliptic flow increases due to the rise in average pt expected from larger radial (azimuthally symmetric) flow. The larger radial flow also leads to a decrease of the elliptic flow at low transverse momentum, which is most pronounced for heavy particles. Models based on a parton cascade, including models that take into account quark recombination for particle production, predict a stronger decrease of the elliptic flow as a function of transverse momentum compared to RHIC energies. Phenomenological extrapolations and models based on final state interactions that have been tuned to describe the RHIC data predict an increase of the elliptic flow of ∼50%, larger than other models. A measurement of elliptic flow at the LHC is therefore crucial to test the validity of a hydrodynamic description of the medium and to measure its thermodynamic properties, in particular, shear viscosity and the equation of state.

The recent measurement of elliptic flow of charged particles in PbPb collisions at $\sqrt{s_{NN}} = 2.76\ TeV$ [79] gave the value of ν_2 to be 0.087±0.002(stat)±0.003(sys.) in the 40%−50% centrality class. And the differential elliptic flow reaches a maximum of 0.2 around $p_T = 3\ GeV/c$, an increase by about 30% comparing with RHIC results with Au-Au collisions at $\sqrt{s_{NN}} = 200\ GeV$. However, the role of radial expansion in the formation of elliptic flow has to be clarified by the further measurements.

Significant strangeness enhancement

Due to the fact that strange quarks have bare mass comparable with the critical temperature, they are expected to be produced abundantly by the thermal parton interactions at high temperature QGP phase. So that the hyperon production containing strange quarks (K^0_S, ϕ) and both singly and doubly strange baryons (Λ and Ξ) should be enhanced. It was confirmed by RHIC in [80] consistent with models of hadron formation based on the quark recombination. The latest measurement with ALICE can be found in [81].

Suppression of quarkonia production

It was predicted by Matsui and Satz [82] that suppression of the quarkonia production was expected to be an unambiguous signature for the formation of a QGP in ultra-relativistic heavy-ion collisions. The prediction has been observed at NA50/CERN-SPS and RHIC.

The measurement of the quarkonia states (such as J/ψ, $\psi^{'}$, χ_c and Υ) provides information on the time scale and dynamics to the quarkonium state ($c\bar{c}$ and $b\bar{b}$, produced involving gluons). The attractive interaction between heavy quarks and antiquarks is foreseen to be reduced because of the dynamic/Debye screening effects in the deconfined state, which will lead the suppression. The strength of the suppression depends not only on the binding energies of the quarkonia, but also the surrounding temperature of the system.

From another side of quarkonia production, more physics effect are involved, such as the initial state energy loss, shadowing, heavy quark energy loss, feed-down corrections from higher mass charmonium states etc, especially at lower $p_T < 2\ GeV/c$. As shown in Fig. 1.5(a), the suppression of J/ψ presents a factor ∼3 at $p_T < 3\ GeV/c$. It matches the models of gluon shadowing, however, the nonlinear gluon saturation effects was suggested to become very important and the gluon densities will be substantial modified [83]. The further investigation is under way.

1.4 Scope of the thesis

In this thesis, the neutral mesons measurement with ALICE electromagnetic calorimeters at the LHC is presented. The arrangement on the thesis is the following:

A short introduction on the high energy physics has been given, including a very brief and basic presentation of the theory and the motivation of the ultra-relativity heavy-ion collisions. Related to the current study, it will be dedicated on the understanding the hot-dense QCD matter. The most relevant and well built observables are presented.

In Chapter 2, in this study we use the photon measurement as a probe to insight into the QCD medium. By recalling the existing results mainly from RHIC, the emphasis is on the objective of the neutral mesons measurement. Then the setup of ALICE experiment is introduced shortly, but the two electromagnetic calorimeters, PHOS and EMCAL, are presented in detail. Then the raw yield of neutral mesons by $\pi^0(\eta) \to 2\gamma$ and $\omega(782) \to \pi^0\gamma \to 3\gamma$ with the realistic geometrical configuration were estimated. It gave us an important reference point before the ALICE data-taking. For PHOS, the study proves the possibility to measure the η and $\omega(782)$ despite of its limited acceptance.

In Chapter 3, depending on the different technical design of PHOS and EMCAL and their momentum reach, the strategies to measure the neutral mesons including invariant mass analysis, shower shape analysis and isolation cut method are presented.

In Chapter 4, the data processing chain from the raw data to physics analysis oriented is presented. It is very important for us a deep understanding of the detector and future physics analysis.

In Chapter 5, we start to analyze the real data to extract the neutral meson spectra. Limited by the statistics and understanding of the detectors, focus is made on the PHOS data analysis. The detailed analysis conditions and the procedures on π^0 are presented.

In Chapter 6, the corrections to the π^0 raw yield are performed. Here we take into account both of the geometrical acceptance and reconstruction efficiency. Then the systematic uncertainties due to the absolute energy scale, non-linearity of the detector response, the bad channels mapping and the π^0 loss are estimated.

In Chapter 7, the production rate is obtained from the analyses described in the two previous chapters analysis. By comparing with the models, discussion and conclusion are presented.

Chapter 2

Photon probes in ALICE experiment with EM-Calorimeters

Photon detection is one of the most promising methods to characterize the medium created at the earliest phase of the collision and its phase of expansion. In this chapter, the processes for photon production are introduced briefly. The motivation to study neutral mesons will also be highlighted. Then two electromagnetic calorimeters in ALICE with PHOS and EMCAL used to measure photons are presented. Finally, we provide the estimation of the expected statistics for neutral mesons production in pp at 900 GeV, 7 TeV, 10 TeV and 14 TeV.

2.1 Photon production

As an electromagnetic particle, photon does not undergo strong interaction with the hot and dense medium produced in hadron-hadron or A-A collisions. Also its mean free path is larger than the typical size of collision system ($\sim 10\ fm$). Thus photon can carry the initial information once they were created during the collision evolution at different stages (pre-equilibrium, thermal QGP, hot hadron gas and hadronic decay) [65]. Depending on their origin, photons are classified into categories as below:

- **Prompt photons** are produced in early stage of collisions in hard or pre-equilibrium partonic cascade processes, Compton scattering ($q(\overline{q}) + g \to \gamma + q(\overline{q})$), annihilation ($q + \overline{q} \to \gamma + g$) from the two incoming partons and quark fragmentation ($q(\overline{q}) \to q(\overline{q}) + \gamma$). The production rate can be calculated through perturbative QCD. Among these processes, Compton scattering is dominant in the leading order calculations. While in next-to-leading order calculation, more complicated processes contribute to the total photon cross section [84]:

$$\frac{d^2\sigma}{d\overrightarrow{p}_T d\eta} = \frac{d^2\sigma^{(D)}}{d\overrightarrow{p}_T d\eta} + \frac{d^2\sigma^{(F)}}{d\overrightarrow{p}_T d\eta}, \tag{2.1}$$

  where D denotes the contribution from Compton scattering and annihilation and F stands for the fragmentation photons. The two terms can be expressed explicitly as [85]

$$\begin{aligned}\frac{d^2\sigma^{(D)}}{d\overrightarrow{p}_T d\eta} = \sum_{i,j=q,\bar{q},g} \int dx_1 dx_2 F_{i/h_1}(x_1, M) F_{j/h_2}(x_j, M) \frac{\alpha_s \mu_R}{2\pi} \\ \times \Big(\frac{d^2\hat{\sigma}_{ij}}{d\overrightarrow{p}_T d\eta} + \frac{\alpha_s(\mu_R)}{2\pi} K_{ij}^{(D)}(\mu_R, M, M_F) \Big),\end{aligned} \tag{2.2}$$

and

$$\begin{aligned}\frac{d\sigma^{(F)}}{d\overrightarrow{p}_T d\eta} = \sum_{i,j,k=q,\bar{q},g} \int dx_1 dx_2 \frac{dz}{z^2} F_{i/h_1}(x_1, M) F_{j/h_2}(x_j, M) D_{\gamma/k}(z, M_F) \\ \times \Big(\frac{\alpha_s \mu_R}{2\pi} \Big)^2 \Big(\frac{d\hat{\sigma}_{ij}^k}{d\overrightarrow{p}_T d\eta} + \frac{\alpha_s(\mu_R)}{2\pi} K_{ij,k}^{(F)}(\mu_R, M, M_F) \Big)\end{aligned} \tag{2.3}$$

where F is the parton distribution function, D is the fragmentation function and $\alpha_s(\mu_R)$ is the strong coupling constant which depends on the normalization scale μ_R. Fig. 2.1(a) presents the world wide inclusive and isolated direct photon production cross sections compared with JETPHOX [86] NLO calculations using CTEQ6M [87] fragmentation function. A good agreement over 9 orders of magnitude in cross sections between the data and theory is observed. Fig. 2.1(b) presents the ratio of data/theory as a function of $x_T = 2p_T/\sqrt{s}$. It exhibits a promising agreement between theory and data in the whole x_T range with the exception of the E706 data.

- **Thermal photons**, which are produced during the QGP thermalization [67, 88–90] phase. The radiation rate of photon with energy E and momentum p is related to the imaginary part of photon self-energy:

$$E\frac{dR}{d^3p} = \frac{-2}{(2\pi)^3} Im \prod_{\mu}^{R,\mu} \frac{1}{e^{E/T} - 1}, \tag{2.4}$$

where $\prod_{\mu}^{R,\mu}$ is the self-energy under finite temperature T. Using the relativistic theory formulation and considering the infrared contribution [91, 92], the final results can be written as:

$$E\frac{dR}{d^3p} = \frac{5}{9}\frac{\alpha\alpha_s}{2\pi^2} T^2 e^{-E/T} ln\Big(\frac{2.912}{g^2}\frac{E}{T}\Big). \tag{2.5}$$

We could note that production rate exhibits a $e^{-E_\gamma/T}$ behavior at low p_T. The thermal photon spectra is important to probe the hot and dense system temperature. However, it is a great challenge to measure it experimentally since the background is huge and this leads to a strong theoretical dependence.

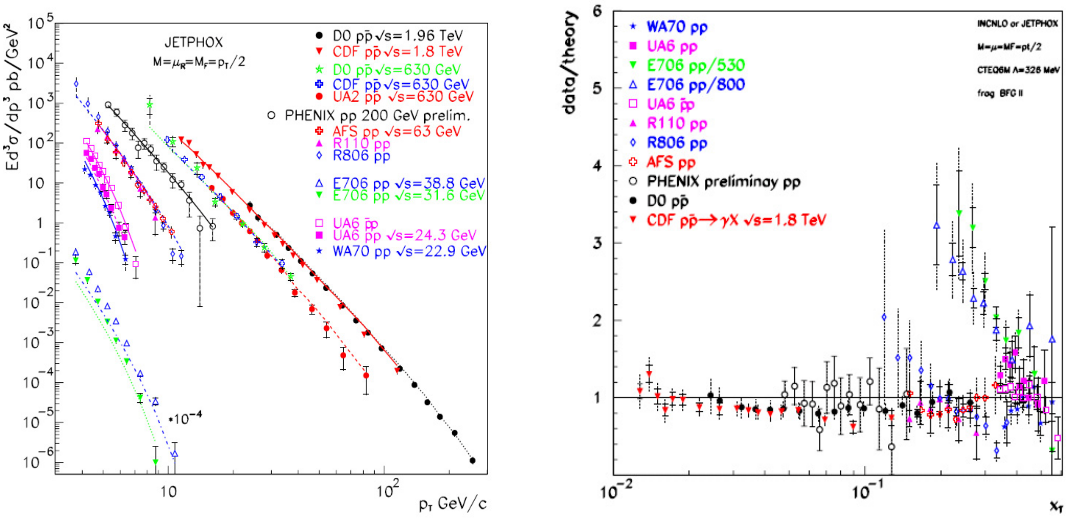

(a) Prompt photons and QGP thermal radiation

(b) Fragmentation photons

Figure 2.1: World-wide inclusive and isolated direct photon cross section (a) and data/theory as a function of $x_T = 2p_T/\sqrt{s}$ (b) in pp and $p\overline{p}$ compared to JETPHOX NLO with CTEQ6M and $M = \mu_R = M_F = \frac{1}{2}p_T$ [84].

- **Jet-photon conversion** [93], produced in secondary interactions of hard parton jets with thermal partons in QGP. The dominant processes are jet-photon conversion ($q_{hard} + \overline{q} \to \gamma + g$ and $q_{hard} + g_{QGP} \to \gamma + g$) and medium induced photon bremsstrahlung. Its contribution can be expressed as:

$$E_\gamma \frac{dN_\gamma^{(anni)}}{d^3p_\gamma d^4x} = E_\gamma \frac{dN_\gamma^{(com)}}{d^3p_\gamma d^4x} = \frac{\alpha\alpha_s}{8\pi^2} \sum_{f=1}^{N_f} (\frac{e_{qf}}{e})^2 [f_q(\mathbf{p}_\gamma) + f_{\overline{q}}(\mathbf{p}_\gamma)] T^2 \times [ln(\frac{4E_\gamma T}{m^2}) - 1.916]. \tag{2.6}$$

  If we include the u, d and s quark flavors, $\sum_f = e_{qf}^2/e^2 = 2/3$. Also here we introduce mass m to shield the infrared divergence. This calculations are well developed to correct the parton energy loss [94].

- **Photons from hot hadron gas.** The hot hadron gas is produced after the freeze-out of quark-gluon plasma. The photons are produced because of the hadronic reactions. The spectrum of these photons dominates at lower p_T (<1 GeV/c). The calculation was performed by Kapusta et al. [90].

- **Decay photons** are the decay products of hadronic resonances. The decay photons from π^0, η, ω etc. are the main contribution (90% more) to the final inclusive photons. Thus experimentally, to extract the direct photon spectra it is crucial to reconstruct the neutral mesons spectra for the background subtraction. In experiment, depending on the detector granularity and the π^0

momentum range, three methods of invariant mass analysis, shower shape analysis and isolation cuts method will be used, and more detailed strategies can be found in Chapter 3.

As for the direct photons [66,67], literally, it means that photons emerged from the collisions directly. Henceforward, so called "direct photon" includes prompt photons, thermal photons and fragmentation photons except for decay photons. From the view of experiment, we can extract direct photon spectrum by subtracting decay photons from inclusive photon spectra. Detailed split of direct photons components is strongly dependent on models.

2.2 The role of neutral mesons measurement

In this thesis, we focus on the neutral mesons measurement with ALICE electromagnetic calorimeters. The measurement is top priority for electromagnetic calorimeters. They will play an **IMPORTANT** role at initial stage of data taking and lead an important role on jet and flow physics. Three neutral mesons π^0 and η as pseudoscalar mesons and $\omega(782)$ as vector meson [1] with their photon decays will be studied in this thesis as shown in Table 2.1. The role of the neutral mesons measurement will be emphasized.

Table 2.1: Neutral mesons measurement by photon decay channels studied in the thesis [95].

Neutral meson	Pdg Mass(GeV/c^2)	Decay channel	Branching ratio
π^0	0.135	2γ	98%
η	0.55	2γ	39%
$\omega(782)$	0.782	$\pi^0\gamma \to 3\gamma$	8.9%

1) **Calibration of the EM-calorimeters**

From the final observed hadrons in pp and AA collisions, about one third are neutral pions. As listed in above table, π^0 with a nominal mass of 135 MeV/c^2 has a 98% branching ratio to 2γ. We can then reconstruct them by 2γ invariant mass analysis to calibrate the electromagnetic calorimeters in an absolute or relative way, especially at early stage of real data analysis in order to understand the detectors [2].

2) **Test of pQCD (theory vs. experiment)**

---

[1] Hereafter in this thesis, the neutral mesons measurement means by π^0, η and $\omega(782)$ with decay channels in Table 2.1

[2] More information on the calibration by π^0 invariant mass can be found in Chapter 4.

The pQCD describes the particle production cross section at large transverse momentum well by considering the factorization holds:

$$\frac{d\sigma^{AB\to C}}{dp_T dy} = \sum_{a,b,c} \int dx_a dx_b \frac{dz}{z^2} F_{a/A}(x_a, M) F_{b/B}(x_b, M) D_{C/c}(z, M_F) \frac{d\widehat{\sigma}^{ab\to c}}{dp_{cT} dy_c}(\mu, M, M_F) \tag{2.7}$$

where F is the parton density function, $D_{C/c}$ is the fragmentation function from the parton c to a hadron C, and $\widehat{\sigma}^{ab\to c}$ is the hard cross section between the partons a and b from A and B respectively to produce a parton c [96–99]. In practice, the next-to-leading order approximation is used to calculate these functions. However, there remain unphysical renormalization factors μ, fragmentation scale M_F and factorization factor M which are adjustable.

3) **Scaling behavior**

The scaling behavior have been found by comparison of the world-wide data from SIS [3] energy to RHIC energy. The implement of LHC data points allow us extend to small x_T range and to explore the system thermal properties by theoretical fit procedure.

4) **Suppression of high p_T spectra**

As shown in Chapter 1 on the nuclear modification factor, the suppression at RHIC is observed for all the neutral mesons. ALICE has the capability to measure them up to higher p_T, which allow to better understand if pQCD holds, and to test the medium properties at extreme high momentum up to 50 GeV/c. In this analysis, the neutral pion spectrum in pp at 7 TeV are analyzed.

2.3 ALICE Experiment

ALICE experiment is one of the four main experiments at the LHC [100–103]. It is dedicated on the heavy ion physics with lead-lead collisions at $\sqrt{S_{NN}} = 5.5\ TeV$, to explore the deconfined state of matter of QGP. The initial pp and pA collisions are significantly involved as a reference for AA collisions to insight the hot-dense medium effects. We entered a new era since Dec. 2009 when the first proton-proton collisions occurred at 900 GeV. Then ALICE delivered to 2.36 TeV and 7 TeV proton-proton collisions, and heavy ion (Pb-Pb) collisions at a center-of-mass energy per nucleon pair $\sqrt{S_{NN}} = 2.76\ TeV$ (see Table: 7.2) [104]. These present an unprecedented high energy region in the laboratory. In the next years, ALICE will go to the designed energy at 10 TeV and 14 TeV for proton-proton collisions and $\sqrt{S_{NN}} = 5.5\ TeV$ for lead-lead collisions.

Fig. 2.2 shows the layout of ALICE detectors, which consist of

---

[3] It has a typical energy of several GeV per nucleon.

Table 2.2: ALICE data taking during the run period 2009∼2010 [104].

Beam types	Energy	Partition	Event statistics
p-p	900 GeV	LHC09d	10 M
p-p	2.36 TeV	LHC09d	50 K
p-p	7 TeV	LHC10b,c,d,e,f	600 M
Pb-Pb	2.76 TeV	LHC10h	50 M

I) Central tracking detectors: Inner Tracking System (ITS) [105], Time Projection Chamber (TPC) [106] and Transition Radiation Detector (TRD) [107], with the objective to measure the charged particles tracks with high momentum resolution and particle identification capability by dE/dx measurement;

II) Electromagnetic calorimeters: PHOton Spectrometer (PHOS) [108] and Electro-Magnetic Calorimeter (EMCAL) [109] for photon detection, neutral mesons and jet related measurements;

III) Muon spectrometer (MUON) [110] for the measurement of heavy quark resonances and decays;

IV) Forward and trigger detectors: Forward Multiplicity Detector (FMD) [111], Photon Multiplicity Detector (PMD) [112] and Zero Degree Calorimeter (ZDC) [113] to measure the global event characteristics. VZERO [111] detector is made of arrays of segmented scintillator counters to provide as a min-bias trigger and beam-gas background rejection. ALICE COsmic Ray DEtector (ACORDE) [114] on top of L3 magnet will trigger the cosmic rays for calibration, alignment and cosmic ray physics. Additional two smaller electromagnetic calorimeters are installed to improve the centrality selection for heavy ion collisions and complement large angle particle detection.

V) The particle identification detectors: Time Of Flight (TOF) [115] as a complement of central tracking detectors for the charged particle identification. A High Momentum Particle IDentification (HMPID) [116] is a Cherenkov ring detector to extend the high momenta particle identification.

During the run period of Nov. 2009∼Dec. 2010, the central barrel detectors ITS, TPC and TOF were fully installed, while 7/18 of TRD, 3/5 of PHOS (without CPV) and 4/10 EMCAL were installed. For each detector, the detailed physics consideration, technical design and physics performance can be found in [117, 118]. The trigger detectors and central tracking detectors, such as VZERO, ITS, TPC and TOF, as well as the electromagnetic calorimeters PHOS and EMCAL, related to the analysis are described as below.

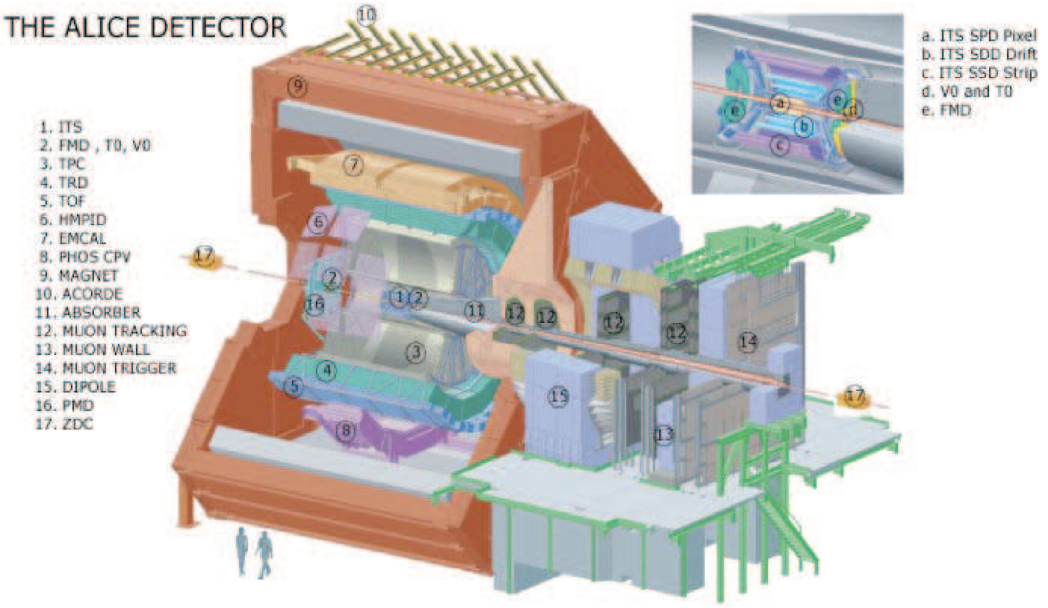

Figure 2.2: ALICE detectors schematic layout at LHC.

ITS

The ITS is designed for charged particle tracking and trigger purpose. To reconstruct the primary vertex and secondary vertex, it requires a rigorous spatial and momentum resolution. It is composed of six cylindrical layers silicon detectors of Silicon Pixel Detector (SPD), Silicon Drift Detector (SDD) and Silicon Strip Detector (SSD) with a radial distance to the beam line from 3.9 to 43 cm.

The first two layers of SPD ($3.9\ cm < r < 7.6\ cm$) lie innermost close to the beam pipe and are equipped by a large amount of pixels, up to 9.8 ($50 \times 425\ \mu m^2$) million by 1200 chips. The chip provides a fast signal if there is at least one pixel fired. The signals from all the chips are combined into a programmable logic unit which supplies a L0-trigger signal. If hits are detected on at least two chips on the outer layer, the SPD will take this into account as a min-bias trigger. The total thickness of SPD amounts to about 2.3% radiation length.

The next two layers of SDD, at a radii of $15\ cm < r < 23.9\ cm$, is made of 260 sensors and allows to measure the drift speed via dedicated triggers. The radiation length is about 2.4% including all the material.

The third two layers of SSD ($38\ cm < r < 43\ cm$) consist of double-sided silicon micro-strip sensors with a readout channels of 2.6 millon. It has a better resolution of $< 20\ \mu m$ in $r - \phi$ direction and 0.8 mm in z direction along the beam line. It contributes to a $\sim 2.2\%$ radiation length in total.

TPC

The ALICE TPC is a cylindrical drift detector with a pseudo-rapidity coverage of $|\Delta\eta| < 0.9$. It has a field cage filled with 90 m^3 of $Ne/CO_2/N_2$ (85.7/9.5/4.8%). The inner and outer radii of the active volume are of 85 cm and 247 cm respectively and the length along the beam direction is of 500 cm. Inside the field cage, ionization electrons produced when charged particles traverse the active volume on either side of the central electrode (a high voltage membrane at -100 kV) migrate to the end plates in less than 94 μs. A total of 72 multi-wire proportional chambers, with cathode pad readout, instrument the two end plates of the TPC which are segmented in 18 sectors and amount to a total of 557, 568 readout pads. The ALICE TPC ReadOut (ALTRO) chip, employing a 10 bit ADC at 10 MHz sampling rate and digital filtering circuits, allows for precise position and linear energy loss measurements with a gas gain of the order of 10^4 .

The position resolution in the $r\phi$ direction varies from 1100 μm to 800 μm when going from the inner to the outer radius whereas the resolution along the beam axis ranges between 1250 μm and 1100 μm.

TOF

It is a cylindrical assembly of Multi-gap Resistive Plate Chambers (MRPC) with an inner radius of 370 cm and an outer radius of 399 cm, a pseudo-rapidity range $|\Delta\eta| < 0.9$ and full azimuth angle, except for the region $260^\circ < \phi < 320^\circ$ at η near zero where no TOF modules were installed to reduce the material in front of the Photon Spectrometer. The basic unit of the TOF system is a 10-gap double-stack MRPC strip 122 cm long and 13 cm wide, with an active area of 120×7.4 cm^2 subdivided into two rows of 48 pads of 3.5×2.5 cm^2. Five modules of three different types are needed to cover the full cylinder along the z direction. All modules have the same structure and width (128 cm) but differ in length. The overall TOF barrel length is 741 cm (active region). It has 152,928 readout channels and an average thickness of 25 - 30% of a radiation length, depending on the detector zone. For pp collisions, such a segmentation leads to an occupancy smaller than 0.02%. Its front-end electronics is designed to comply with the basic characteristics of a MRPC detector, i.e. very fast differential signals from the anode and cathode readout. Test beam results demonstrated a time resolution below 50 ps, dominated by the jitter in the electronic readout.

VZERO

The VZERO detector is made of two arrays of 32 scintillators placed on both sides of interaction point side along the beam line with a distance $z = 3.3$ m (A side) and $z = -0.9$ m (C side). It covers a pseudorapidity region $2.8 < \eta < 5.1$ and $-3.7 < \eta < -1.7$ respectively. The time resolution is < 1 ns and a good timing response about 25 ns around the nominal beam crossing time. The min-bias trigger is determined based on the trigger signals from VZEROR-A, VZEROR-C and SPD, and by the LHC bunch-crossing signal.

Track reconstruction [81]

The reconstruction in the tracking detectors begins with charge cluster finding. The two coordinates of the crossing points (space points) between tracks and detector sensitive elements (pad rows in the TPC, and silicon sensors in the ITS) are calculated as the centres of gravity of the clusters. The errors on the space point positions are parametrized as a function of the cluster size and of the deposited charge. For the TPC, these errors are further corrected during the tracking, using the crossing angles between tracks and the pad rows.

The space points reconstructed at the two innermost ITS layers (pixel detector, SPD) are then used for the reconstruction of the primary vertex. One space point from the first SPD layer and one from the second layer are combined into pairs called ”tracklets”. The primary vertex is consequently reconstructed in 3D as the location that minimizes the sum of the squared distances to all the tracklet extrapolations. If this fails, the algorithm instead reconstructs the z coordinate of the vertex by correlating the z coordinates of the SPD space points, while for x and y the average position of the beam in the transverse plane (measured by a dedicated calibration procedure on a run-by-run basis) is assumed.

Track reconstruction in ALICE is based on the Kalman filter approach [119]. The initial approximations for the track parameters (the ”seeds”) are constructed using pairs of space points taken at two outer TPC pad rows separated by a few pad rows and the primary vertex. The a priori uncertainty of the primary vertex position used in the seeding procedure is considered to be equal to the diameter of the beam pipe (3 cm) to limit the bias for tracks coming from particles decaying inside this volume. The seeds for the secondary tracks are created without using the primary vertex, since such a constraint would unnecessarily reduce the V0 finding efficiency. The additional space points used as a seed are then searched along the straight line segment connecting the pairs of points taken at those two outer TPC pad rows.

Once the track seeds are created, they are sorted according to the estimate of their transverse momentum(p_T). Then they are extended from one pad row to another in the TPC and from one layer to another in the ITS towards the primary vertex. Every time a space point is found within a prolongation path defined by the current estimate of the covariance matrix, the track parameters and the covariance matrix are updated using the Kalman filter. For each tracking step, the estimates of the track parameters and the covariance matrix are also corrected for the mean energy loss and Coulomb multiple scattering in the traversed material. The decision on the particle mass to be used for these corrections is based on the dE/dx information given by the TPC when available. If the information is missing or not conclusive, a pion mass is assumed. Only five particle hypotheses are considered: electrons, muons, pions, kaons and protons.

All the tracks are then propagated outwards, through the ITS and the TPC. When possible, they are matched with the hits reconstructed in the TOF detector. During this tracking phase, the track length and five time-of-flight hypotheses per track (corresponding to the electron, muon, pion, kaon and proton masses) are calculated. This information is later used for the TOF PID procedure. The track parameters are then re-estimated at the distance of closest approach (DCA) to the primary vertex applying the Kalman filter to the space points already attached. Finally, the primary vertex is fitted once again, now using reconstructed tracks and the information about the average position and spread of the beam-beam interaction region estimated for this run.

In pp collisions, the track reconstruction efficiency in the acceptance of TPC saturates at about 90% because of the effect of the dead zones between its sectors. It goes down to about 75% around $p_T = 1$ GeV/c and falls to 45% at 0.15 GeV/c. It is limited by particle decays (for kaons), track bending at low p_T and absorption in the detector material. The amount of material traversed by particles near $\eta = 0$ is about 11% of of the radiation length including the beam pipe, the ITS and the TPC (with service and support).

The overall p_T resolution is at least as good as the TPC-standalone resolution, which is typically 1% for momenta of 1 GeV/c and 7% for momenta of 10 GeV/c, and follows the parameterization: $(\sigma(p_T)/p_T)2 = (0.01)^2 + (0.007p_T)^2$, where p_T is expressed in GeV/c [120].

The resolution of the track transverse impact parameter (the minimal distance between a track and the primary vertex in the transverse plane) depends on the precision of track and primary vertex reconstruction. These in turn depend on the momentum, and, in the case of the vertex, on the number of contributing tracks. As it was estimated from the data, the transverse impact parameter resolution in a typical pp event could be parameterized as $\sigma(p_T) = 50 + 60/(p_T)^{0.9}$ (σ is in μm, and p_T is in GeV/c), which was defined by the level of the ITS alignment achieved in 2009.

The dE/dx resolution of the TPC is estimated to be about 5% for tracks with 159 clusters [121], which is better than the design value [118]. When averaged over all reconstructed tracks, this resolution is about 6.5%.

During the run, the preliminary calibration of the TOF detector corresponds to a resolution of 180 ps, which includes 140 ps due to the jitter in the absolute time of the collisions. This contribution is reduced to about 85 ps for those events with at least 3 tracks reaching the TOF, in which case an independent time zero determination is possible. The matching efficiency with TPC tracks (which includes geometry, decays and interaction with material) is on average 60% for protons and pions and reaches 65% above $p_T = 1$ GeV/c. For kaons, it remains slightly lower [122]. Above p_T = 0.5 GeV/c, the TOF PID has an efficiency larger than 60% with a very small contamination.

2.4 ALICE EM-Calorimeters

2.4.1 PHOS

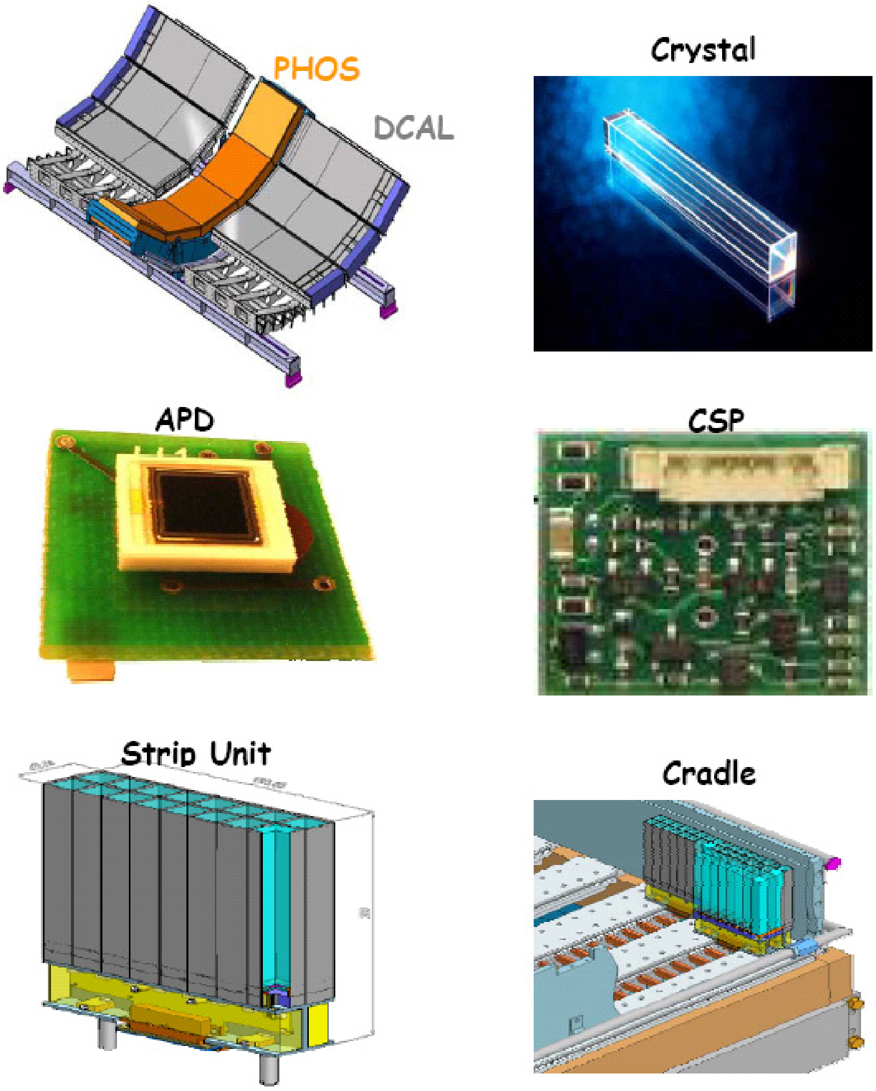

Figure 2.3: ALICE PHOS detector and the components of PbWO4 crystal, APD, CSP, strip unit and a PHOS module.

PHOS was designed to measure π^0, direct photons and study of γ-jet correlations over a large momentum range to probe the properties of QCD matter. It is also expected to measure the soft photon down to 0.3 GeV to explore the dynamics of the thermal medium.

PHOS is a high resolution electro-magnetic calorimeter placed at a radial distance of 460 cm from the interaction point [123]. It consists in 5 identical modules [4] and covers an azimuthal angle from 220° to 320° and a pseudo-rapidity of $|\triangle\eta| < 0.12$, as shown in Fig. 2.3 with the yellow color. Each module consists in a matrix of 56×64 $PbWO_4$ crystals. The $PbWO_4$ [124] is a fast scintillation crystal (high intrinsic time resolution of 0.13 ns) with a light emission of 400 nm to 500 nm. Each crystal has a dimension of $22\times22\times180$ mm^3. The length (180 mm) corresponds to a $20X_0$ radiation length to fully contain high energy electromagnetic shower particles. It provides a fine granularity of $\Delta\phi \times \Delta\eta = 4.8 \cdot 10^{-3} \times 4.3 \cdot 10^{-3}$ to separate the different electromagnetic showers.

The sketch of the PHOS assembly is illustrated in Fig. 2.3. The signal is collected by S8664-55 APDs (Avalanche Photon Diode) with an active area of 5×5 mm^2. They are mounted at the bottom of the $PbWO_4$ crystal and protected by a thin epoxy shield on the top of surface. The typical spectra response is about 600 nm with a quantum efficiency around 85%. The APD gain factor increases with a decreasing temperature to a factor 3 at $-20°C$ compared to the gain at room temperature with a bias voltage of 350 V and an input capacitance of 80 pF.

The low noise Charged Sensitive Preamplifier (CSP) are mounted at the back side of APDs to detect the scintillation light and collect the analog signals. The power supply is ranged from +12 to 6 V with a power consumption of 64 mW. The gain of CSP is measured to be 0.78 $V \cdot pC^{-1}$ with a RMS noise of 200-500 electrons.

Each 8×2 crystals are assembled into a crystal strip unit and two strip units are connected to a FEE (Front-End Electronics) [126,127]. The FEEs are developed and manufactured by ALICE Wuhan-China group to process the electronic signal from CSP. To fit the requirement of ALICE, two 10-bit 10 MHz sampling ADCs are used for two different dynamics ranges from 5 MeV to 5 GeV for high gain channels and 80 MeV to 80 GeV for low gain channels. In addition, FEEs also provide fast 2×2 analog energy sum outputs to TRUs (Trigger Region Unit) for a L0/L1 trigger decision generation. Each FEE has 32 detection readouts with dual gains.

For each module, in total, there are one hundred twelve FEEs, eight Trigger Readout Unit (TRU) and four Readout Control Unit (RCU). The RCU will transmit the ADC samples from the readout buffer to ALICE data acquisition system. The data processing chain from raw data to the physics data at the offline level will be presented in Chapter 4.

Note that the light yield of $PbWO_4$ and the electronic noise level of the APD and CSP will be reduced a factor ~ 3 at a temperature of $-25°C$ as compared to those at in room temperatures. As a consequence PHOS crystals, APDs and CSPs are operated at the temperature of $-25°C$ with a fluctuation of $0.1°C$. It is achieved by a PHOS cooling system based on a liquid coolant Hydrofluoroether. The detector readout and trigger detectors are kept at a temperature of $15°C$. In addition, to keep the system stabilized at low humidity, nitrogen is fluxed through PHOS enclosure interior.

---

[4] Three modules were installed during the data-taking period 2009∼2010 without CPV [125].

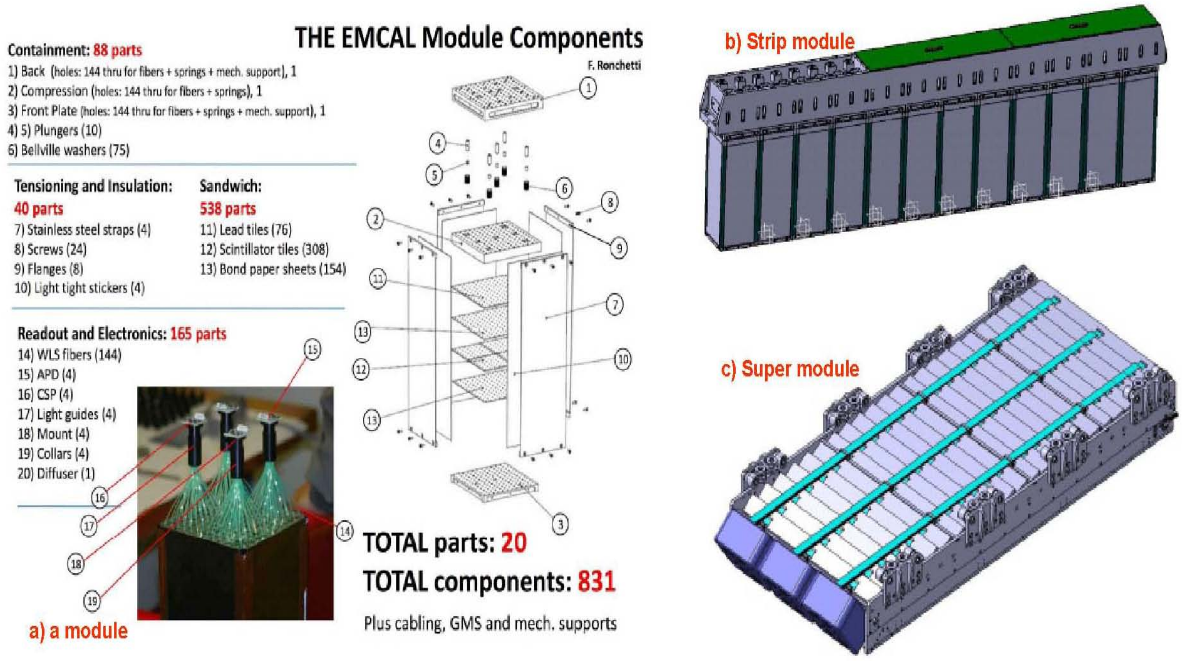

Figure 2.4: EMCAL detector. a) A module component = 2 × 2 modules; b) The strip module = 12 modules; c) A super module = 24 strip modules.

2.4.2 EMCAL

The goal of EMCAL is to study the interaction and energy loss of high energy partons in QCD matter by measuring jets and high-p_T particles (studying the jet quenching phenomenon). It enables triggering on high energy jets, to reduce significantly the measurement bias for jet quenching studies, to improve jet energy resolution, and augments existing ALICE capabilities to measure high momentum photons and electrons. Combined with ALICE excellent capabilities to track and identify particles from very low p_T to high p_T, the EMCal enables an extensive study of jet quenching at the LHC [128].

EMCAL is a lead-scintillator sampling electromagnetic calorimeter with a larger geometrical acceptance of azimuthal angle range of $\Delta\phi = 100°$ and a rapidity of $\triangle\eta| < 0.7$. It is positioned to provide partial back-to-back coverage with PHOS. Small azimuthal gaps ($\sim 3.0\ cm$) are provided between super modules to facilitate installation and alignment. These gaps are positioned in line with the TPC sector boundaries. Along these sector boundaries, there is substantial additional structural material required for the support of the TPC and other ALICE detectors that would significantly degrade any electromagnetic measurements made in these gaps.

The chosen technology is a layered Pb-scintillator sampling calorimeter with a longitudinal pitch of 1.44 mm Pb and 1.76 mm scintillator with longitudinal wave-

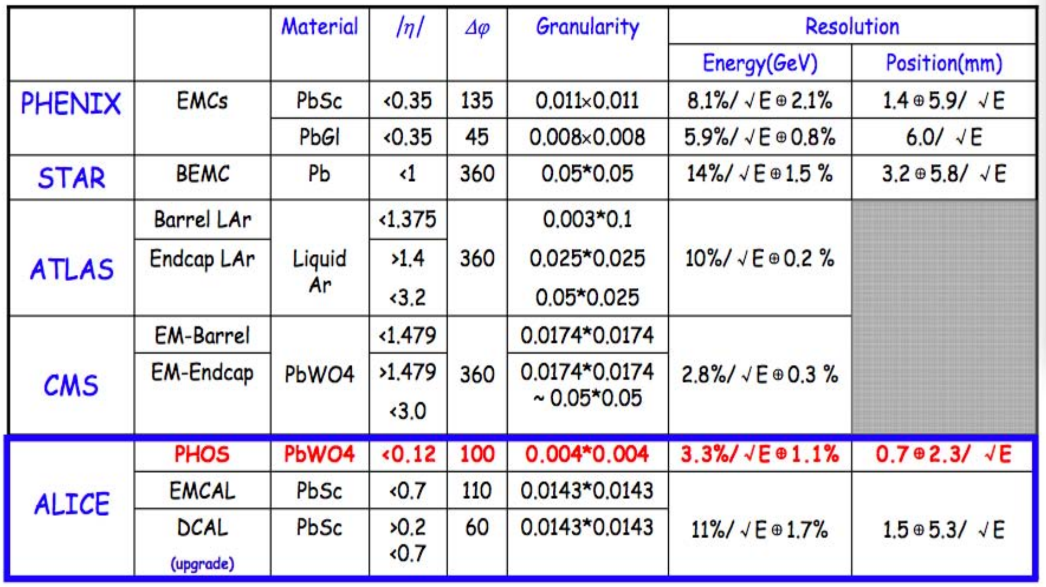

		Material	$/\eta/$	$\Delta\varphi$	Granularity	Resolution	
						Energy(GeV)	Position(mm)
PHENIX	EMCs	PbSc	<0.35	135	0.011×0.011	8.1%/ √E ⊕ 2.1%	1.4 ⊕ 5.9/ √E
		PbGl	<0.35	45	0.008×0.008	5.9%/ √E ⊕ 0.8%	6.0/ √E
STAR	BEMC	Pb	<1	360	0.05*0.05	14%/ √E ⊕ 1.5 %	3.2 ⊕ 5.8/ √E
ATLAS	Barrel LAr	Liquid Ar	<1.375	360	0.003*0.1	10%/ √E ⊕ 0.2 %	
	Endcap LAr		>1.4 <3.2		0.025*0.025 0.05*0.025		
CMS	EM-Barrel	PbWO4	<1.479	360	0.0174*0.0174	2.8%/ √E ⊕ 0.3 %	
	EM-Endcap		>1.479 <3.0		0.0174*0.0174 ~ 0.05*0.05		
ALICE	PHOS	PbWO4	<0.12	100	0.004*0.004	3.3%/ √E ⊕ 1.1%	0.7 ⊕ 2.3/ √E
	EMCAL	PbSc	<0.7	110	0.0143*0.0143	11%/ √E ⊕ 1.7%	1.5 ⊕ 5.3/ √E
	DCAL (upgrade)	PbSc	>0.2 <0.7	60	0.0143*0.0143		

Figure 2.5: ALICE electromagnetic calorimeters PHOS and EMCAL compared with others at PHENIX, STAR, CMS and ATLAS.

length shifting fiber light collection (Shashlik), as shown in Fig. 2.4. The detector is segmented into 12,672 towers, each of which is approximately projective in η and ϕ to the interaction vertex.

The towers are grouped into super modules of two types: full size which span $\Delta\eta$ $=0.7$ and $\Delta\phi = 20°$. The super module is the basic structural units of the calorimeter. These are the units handled as the detector is moved below ground and rigged during installation.

Each super module is assembled from $12 \times 24 = 288$ modules arranged in 24 strip modules of 12×1 modules each. Each module has a rectangular cross section in the ϕ direction and a trapezoidal cross section in the η direction with a full taper of 1.5°. The resultant assembly of stacked strip modules is approximately projective with an average angle of incidence of less than 2° in η and less than 5° in ϕ. EMCAL uses the almost same readout and electronic as PHOS, but with some other improvement due to the two different designs.

As a summary, Fig. 2.5 shows the ALICE electromagnetic calorimeters PHOS and EMCAL. They are also compared with some other calorimeters at PHENIX, STAR, CMS and ATLAS.

Besides, ALICE is a complex system including trigger system, data acquisition, experiment control system (ECS) and detector control system (DCS) [129]. The powerful offline computing provide us with a flexible way to handle the mass data with the middleware of AliEn [130]. The AliRoot [131] software, which uses the ROOT [132] system as a foundation, was developed to deal with these functions and is the tool to simulate, reconstruct and analyze data.

2.5 Yield estimation

Before going to the principal part of the thesis, the neutral mesons production rate with the photon detection channels are estimated, with the purpose to estimate the expected raw yields for a given run picture and evaluate their measurement feasibility [133]. The procedure starts from the well-known and general formula of invariant cross section [95]:

$$E\frac{d^3\sigma}{dp^3} = \frac{1}{2\pi p_T}\frac{d^2\sigma}{dp_T dy} = \frac{1}{2\pi p_T}\frac{d\sigma}{dp_T}|_{\Delta y=1} \tag{2.8}$$

and

$$\frac{dN}{dp_T} = \mathcal{L}_{int}\cdot A\cdot\epsilon\cdot Br\cdot\frac{d\sigma}{dp_T} \tag{2.9}$$

where $\mathcal{L}_{int}$ is the integrated luminosity, A denotes for the geometrical acceptance, $Br.$ is the decay branching ratio and ϵ is the total correction factor (reconstruction efficiency, conversion, trigger efficiency etc.).

Validation of the procedure

The leading-order calculation by PYTHIA [134] event generator is used to estimate the invariant cross section for π^0, η and $\omega(782)$. And their spectra $dN^2/(2\pi p_T dp_T dy)$ in an unity rapidity are normalize by a factor $PARI(1)/N_{events}$ [5] to obtain the invariant cross section. We first validated the procedure and compared the results with the PHENIX results with pp collisions at 200 GeV, as shown in Fig. 2.6. The simulation can be well reproduced to fit the data. The real lines are fitted with a Tsallis function ($f(x) = \alpha\times(1+\frac{\beta\cdot x}{n})^{-n}$, where a, b and c are fit parameters). However, there is a noticeable difference for high p_T ω, probably due to the lower statistics and larger systematic uncertainties.

Invariant cross section

Then the invariant cross section for π^0, η and $\omega(782)$ in pp collisions at 900 GeV, 7 TeV, 10 TeV and 14 TeV are estimated in a similar way by PYTHIA, as shown in Fig. 2.7. The fitting parameters of the invariant cross section for the neutral mesons in pp collisions at 7 TeV are listed in Table: 2.5. They are fitted with a function of $f(x) = \alpha\times(1+\frac{\beta\cdot x}{n})^{-n}$ corresponding to π^0, η and ω.

Geometrical acceptance

Then we calculate the geometrical acceptance, defined as:

$$A = \frac{\frac{d^2N}{dp_T dy}(In\ calorimeter)}{\frac{d^2N}{dp_T dy}(Generated\ in\ |\Delta y| = 1\ and\ \Delta\phi = 2\pi)}, \tag{2.10}$$

---

[5] In PYTHIA, PARI(1) return the total integrated cross section for a given process, in mb.

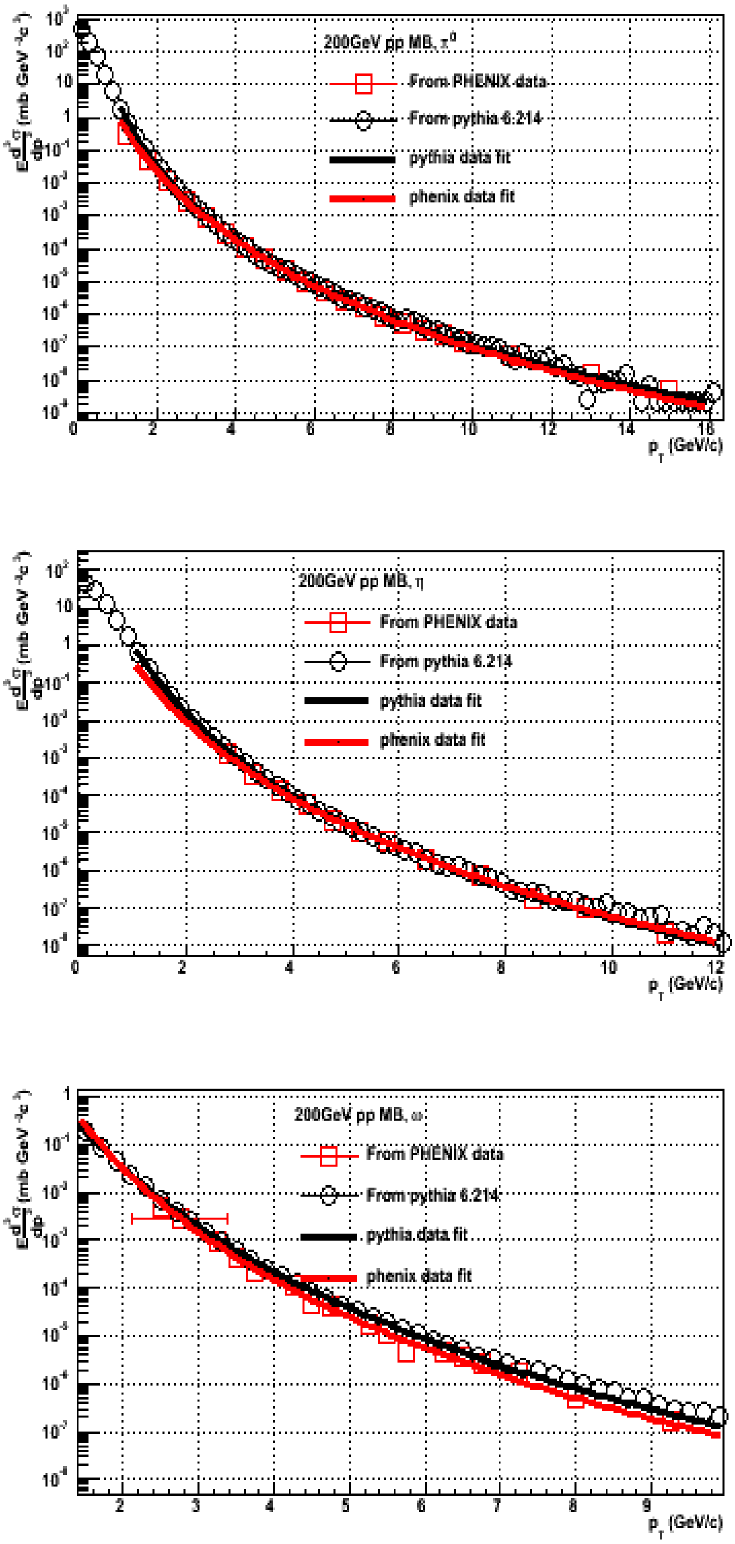

Figure 2.6: The validation of the invariant cross section calculated by PYTHIA. The simulation results are compared with pp collisions at 200 GeV in PHENIX at RHIC [26,149,150].

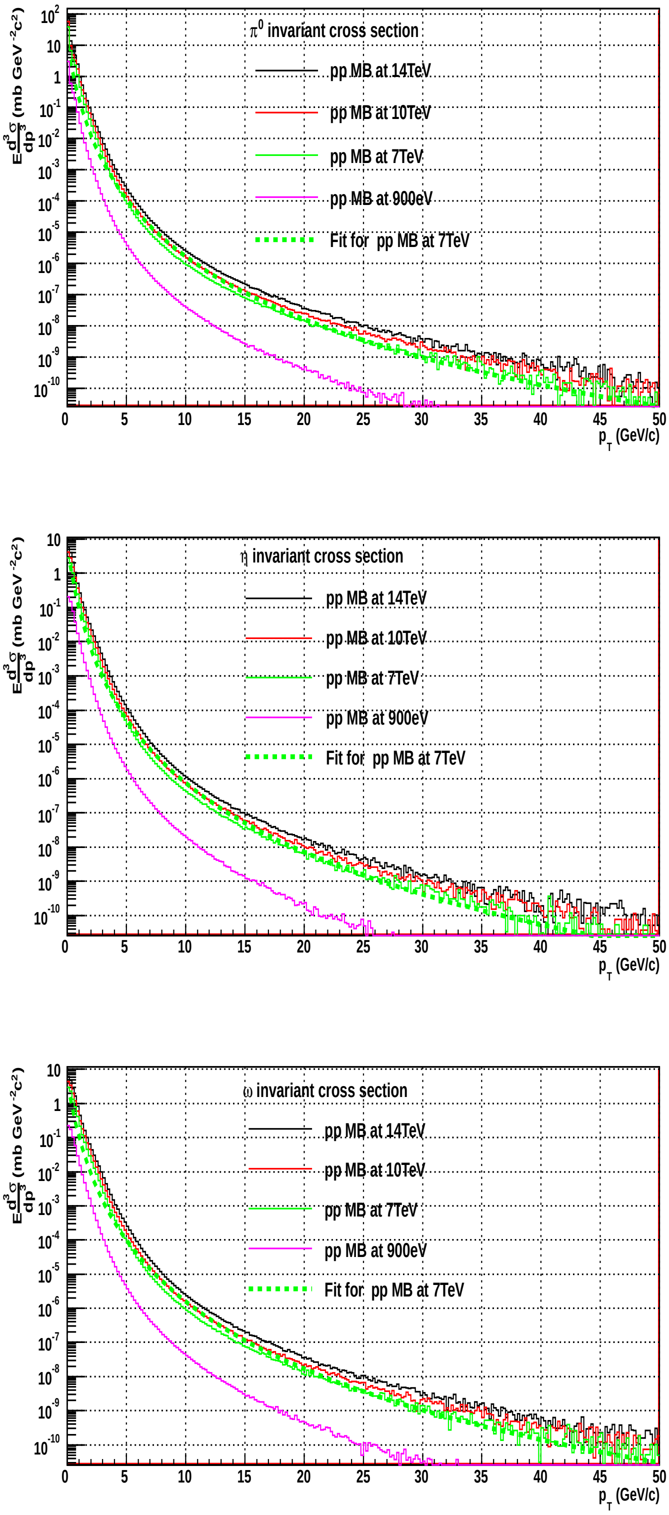

Figure 2.7: The neutral mesons π^0, η and $\omega(782)$ invariant cross-section at 900 GeV, 7 TeV, 10 TeV and 14 TeV. The lines are fitted by a power law function.

Table 2.3: Fitting parameters of the invariant cross section (PYTHIA) for the neutral mesons in pp at 7 TeV with the function of $f(x) = \alpha \times (1 + \frac{\beta \cdot x}{n})^{-n}$.

Neutral meson	α	β	n
π^0	8.28	5.31	7.30
η	5.63	5.47	7.46
$\omega(782)$	5.65	4.88	7.46

where the numerator denotes the accepted neutral mesons with the decay photons in the acceptance of electromagnetic calorimeters.

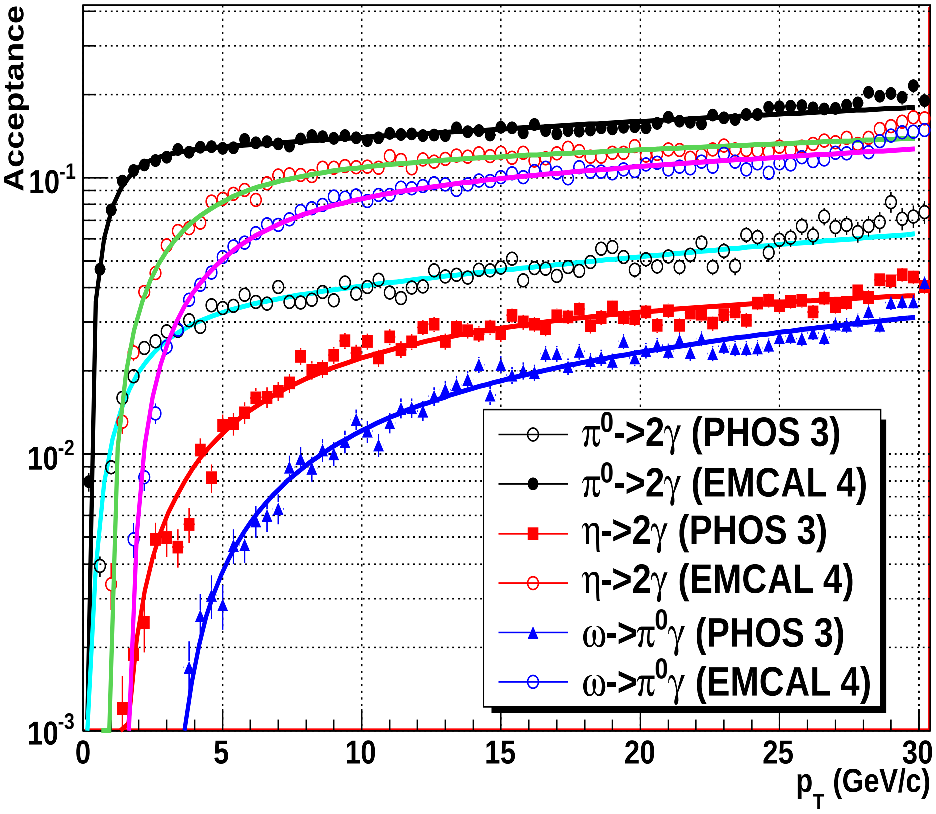

Figure 2.8: PHOS and EMCAL geometry acceptance for $\pi^0 \to 2\gamma$, $\eta \to 2\gamma$ and $\omega(782) \to \pi^0\gamma \to 3\gamma$ by simulation with a flat distribution. The results are fitted by a function of $f(x) = (a + bx)[1 - e^{\frac{-x+c}{d}}]$.

The fast simulation without going through the detectors has been done for detector geometrical acceptance calculation. All the π^0, η and $\omega(782)$ are forced to decay to the channels as we studied with a uniform distribution in p_T, rapidity and azimuthal. The real geometry for 3 PHOS modules and 4 EMCAL super modules are taken into account, as shown in Fig. 2.8. The results are fitted by a function of $f(x) = (a + bx)[1 - e^{\frac{-x+b}{c}}]$ with their fitting parameters listed in Table: 2.4. No doubt that EMCAL has a larger geometrical acceptance 4/7/5 times larger than PHOS corresponding. So that it has a great potential for the neutral mesons measurement.

Table 2.4: Fitting parameters (the errrors are in the bracket) with the function of $f(x) = (a + bx)[1 - e^{\frac{-x+c}{d}}]$ for the acceptance for $\pi^0 \rightarrow 2\gamma$, $\eta \rightarrow 2\gamma$ and $\omega \rightarrow \pi^0\gamma$ with PHOS 3 modules and EMCAL 4 super modules.

		Pi0->2gamma	Eta->2gamma	Omega->pi0+gamma
a	PHOS-3	2.75939e-02 (6.63121e-04)	8.37386e-03 (6.70943e-04)	-3.12325e-03 (1.69649e-04)
	EMCAL-4	1.21973e-01 (1.08269e-03)	7.74654e-02 (1.25589e-03)	5.44142e-02 (1.77314e-03)
b	PHOS-3	1.29376e-03 (4.68215e-05)	1.27250e-03 (3.15068e-05)	1.38718e-03 (1.29792e-05)
	EMCAL-4	1.74697e-03 9.01175e-05	2.69519e-03 (5.87797e-05)	3.04003e-03 (7.22700e-05)
c	PHOS-3	1.94965e-01 7.13297e-03	1.32190e+00 (7.41447e-02)	2.63865e+00 (1.76001e-01)
	EMCAL-4	1.40367e-01 5.37611e-03	9.49731e-01 (1.56332e-02)	1.05509e+00 (7.40067e-03)
d	PHOS-3	1.69608e+00 7.25592e-02	2.48306e+00 (2.06137e-01)	9.12471e-01 (2.52595e-01)
	EMCAL-4	9.12202e-01 2.52924e-02	1.95425e+00 (7.06542e-02)	3.99451e+00 (1.45196e-01)

Reconstruction efficiency

The reconstruction efficiency is defined as:

$$\epsilon = \frac{\frac{d^2N}{dp_T dy}(Reconstructed)}{\frac{d^2N}{dp_T dy}(In\ calorimeter)}. \tag{2.11}$$

To make the reconstruction efficiency close to the reality, the bad channel maps and the real geometry configuration as in the data-taking period 2009~2010 are used. Only PHOS and EMCAL were switched on to save the CPU resources and computing time. Also we use the uniform distributions for π^0, η and $\omega(782)$ with desired decay channels as input for particle transportation in detectors. Considering the edge effect of the detectors, the shotting coverage is a bit larger than the actual: $|\Delta\eta| < 0.13$ and $250° < \phi < 330°$ for PHOS and $|\Delta\eta| < 0.8$ and $70° < \phi < 130°$ for EMCAL.

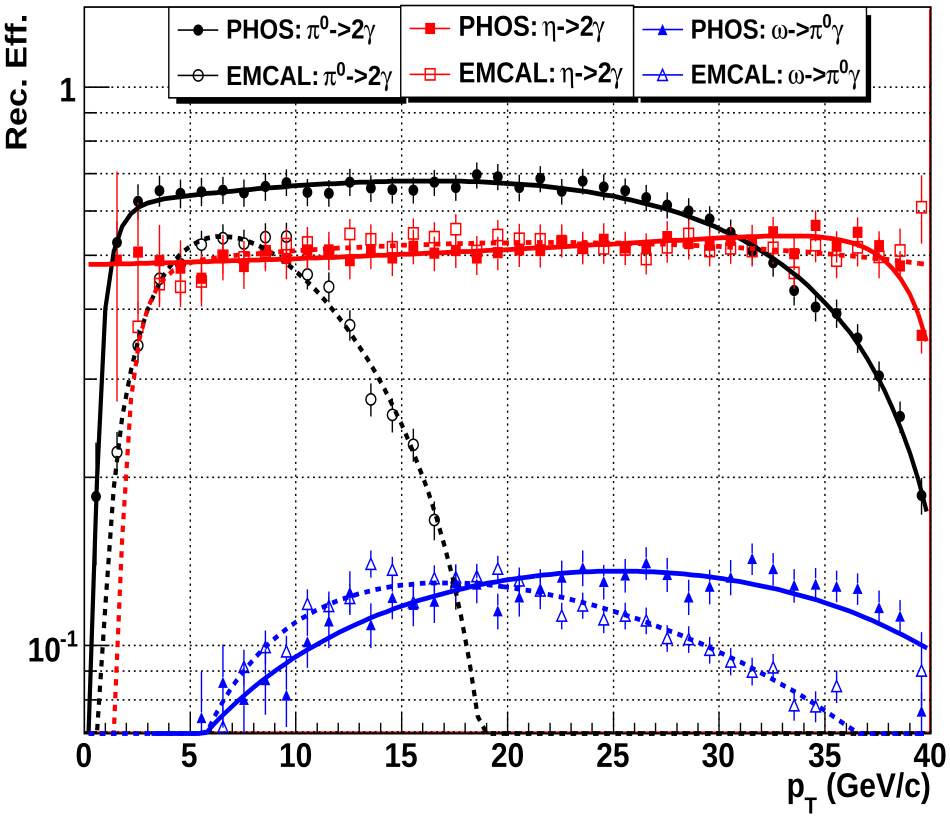

Figure 2.9: The reconstruction efficiencies for the three mesons with PHOS 3 modules and EMCAL 4 modules, which is simulated with the same geometry configuration and conditional data-base as in data-taking period 2009-2010.

Fig. 2.9 shows the reconstruction efficiency for the three mesons with three PHOS modules and four EMCAL modules. The efficiencies are fitted by proper functions to be used for the yield estimation. For PHOS, reconstruction efficiency reaches a value of 70% at the intermediate p_T. While for EMCAL, it reaches the value of about 55% and then goes down because of the cluster overlapping [6]. For η meson, due to the larger opening angle between the two decay photons, the reconstruction efficiency stays at a 50% for PHOS and EMCAL. The reconstruction efficiency of ω (as a three body decay) reaches a saturation or maximum value of about 12%, which can be approximated as ϵ_γ^3 or $\epsilon_{\pi^0} * \epsilon_\gamma$.

---

[6] Due to a relative bigger granularity, the standard algorithm used for PHOS has the limited capability of cluster unfolding for EMCAL. But a new clustering algorithm is being developed.

Estimation of the raw yield

From Eq. 2.8, Eq. 2.9 and the simulation results shown in Fig. 2.7, Fig. 2.8 and Fig 2.9, raw integrated yield estimation with the realistic geometry acceptance and reconstruction conditional data-base are shown in Fig. 2.10. Here we assume the integrated luminosities in the data taking as 10 nb^{-1} and 100 nb^{-1} which correspond about 2 days and 20 days data-taking at a luminosity of $5 \times 10^{28} cm^2 s^{-1}$, respectively.

With the integrated luminosity of 10 nb^{-1}, we could measure the neutral mesons spectra with a transverse momentum up to 20∼25 GeV/c (PHOS) and 15∼20 GeV/c (EMCAL) for $\pi^0 \to 2\gamma$, 10∼15 GeV/c (PHOS) and 15∼20 GeV/c (EMCAL) for $\eta \to 2\gamma$, 5∼10 GeV/c for $\omega(782) \to \pi^0\gamma \to 3\gamma$. However, because of the huge combinatorial background in the lower p_T range for the ω reconstruction, therefore, their low p_T measurement is challenging. At the higher luminosity, we should be able to reach to reach a higher p_T to 40∼50 GeV/c, 20∼30 GeV/c and 15∼20 GeV/c for π^0, η and ω separately.

2.6 The goal of my study

It is expected to measure the neutral mesons up to very high p_T with ALICE electro-magnetic calorimeters. However, it is a long term effort before fully achieve these physics objectives, because the apparatus response understanding and its fine calibration are time consuming tasks. My purpose was to understand the detectors and how to obtain the reliable physics data. Starting from this point, what I want to emphasize are my contributions on the strategy of the neutral mesons measurement, the data processing chain and the real-data analysis to get the π^0 spectrum from the first data with pp collisions at 7 TeV.

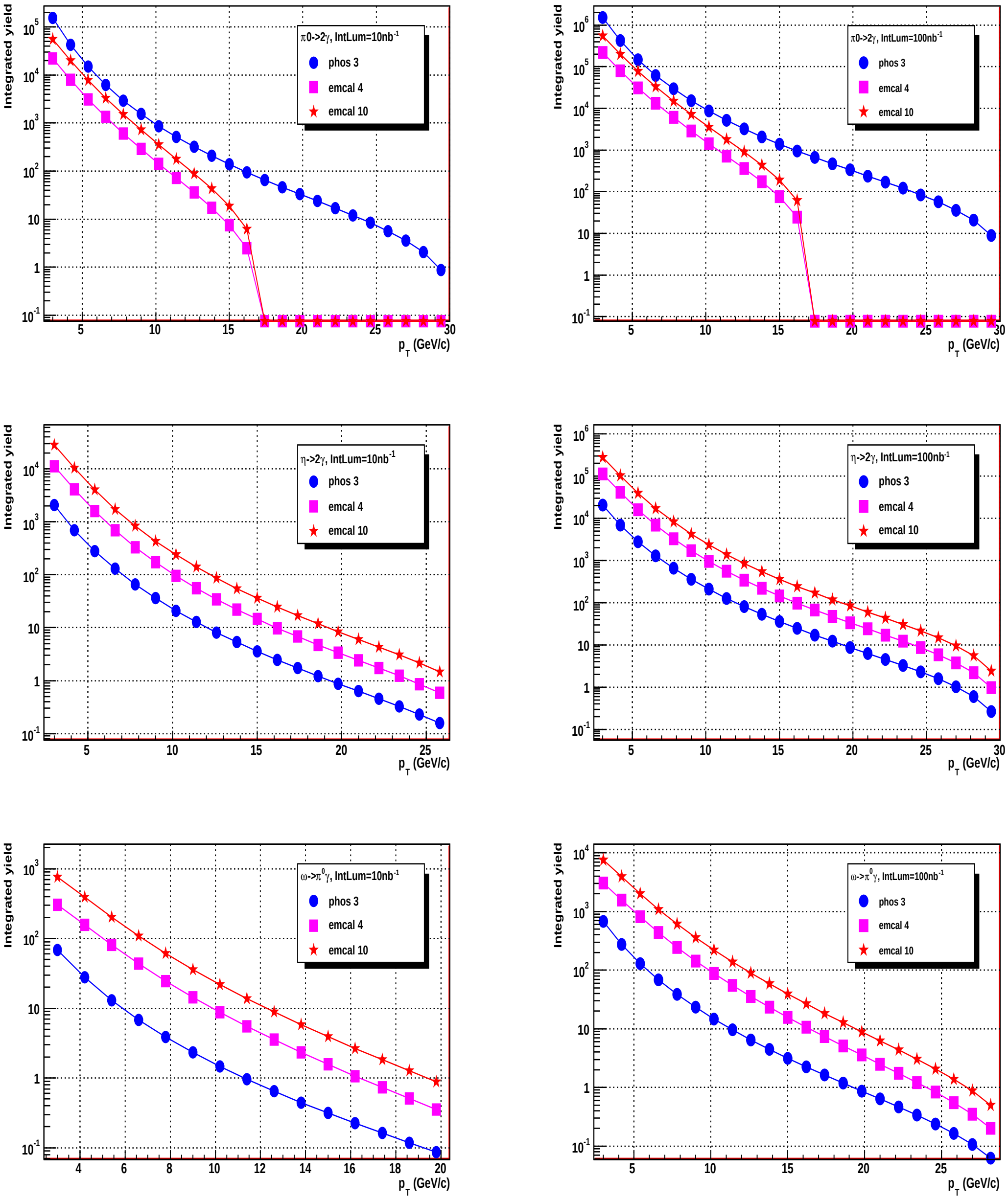

(a) (b)

Figure 2.10: Neutral mesons raw integrated yield estimation with the three detection channels of $\pi^0(\eta) \rightarrow 2\gamma$ and $\omega(782) \rightarrow \pi^0\gamma \rightarrow 3\gamma$ for PHOS and EMCAL under two integrated luminosities: (a) 10 nb^{-1} and (b) 100 nb^{-1}.

Chapter 3

Strategy of neutral meson measurements

As described in previous chapter, thanks to ALICE calorimeters(PHOS and EMCAL), we are able to measure the neutral mesons with $p_T > 50\ GeV/c$ with an integrated luminosity of 100 nb^{-1}. The strategy to measure neutral mesons depends on their p_T. With the increase of the transverse momentum, the opening angle between the decay photons becomes smaller. The decay products start to overlap and thus to be misidentified as a single cluster. Three methods used to extract the neutral mesons are discussed [1] [135]: invariant mass analysis, shower shape analysis and isolation cut method.

3.1 Invariant mass analysis

In particle physics, sometimes it is difficult to identify the particles one-by-one through their decay products. The method of invariant mass analysis in a statistical way is widely used with the formula for two-dody decays:

$$M_{12} = \sqrt{E_1^2 + E_2^2 - (\overrightarrow{p_1} + \overrightarrow{p_2})^2} = \sqrt{m_1^2 + m_2^2 + 2(E_1E_2 - \overrightarrow{p_1} \cdot \overrightarrow{p_2})}, \tag{3.1}$$

where ($\overrightarrow{p_1}$, E_1, m_1) and ($\overrightarrow{p_2}$, E_2, m_2) are the four-momentum, energy and rest mass of the two decay products. At a low transverse momentum of the neutral mesons, the decay photons can be well separated and measured by PHOS and EMCAL. The invariant mass analysis is used in such a context.

3.1.1 $\pi^0(\eta) \to 2\gamma$

For the decay of $\pi^0(\eta) \to 2\gamma$, due to zero rest mass of photon the formula (3.1) can be simplified as

$$M_{\gamma\gamma} = \sqrt{2E_1E_2(1 - \cos\phi_{12})}. \tag{3.2}$$

Practically, we loop the photon pairs in one event. The correlated pairs from the $\pi^0(\eta)$ decay will contribute to the signal, while the uncorrelated photon pairs

---

[1] This work was reported at the conference of hot quark 2010 in France.

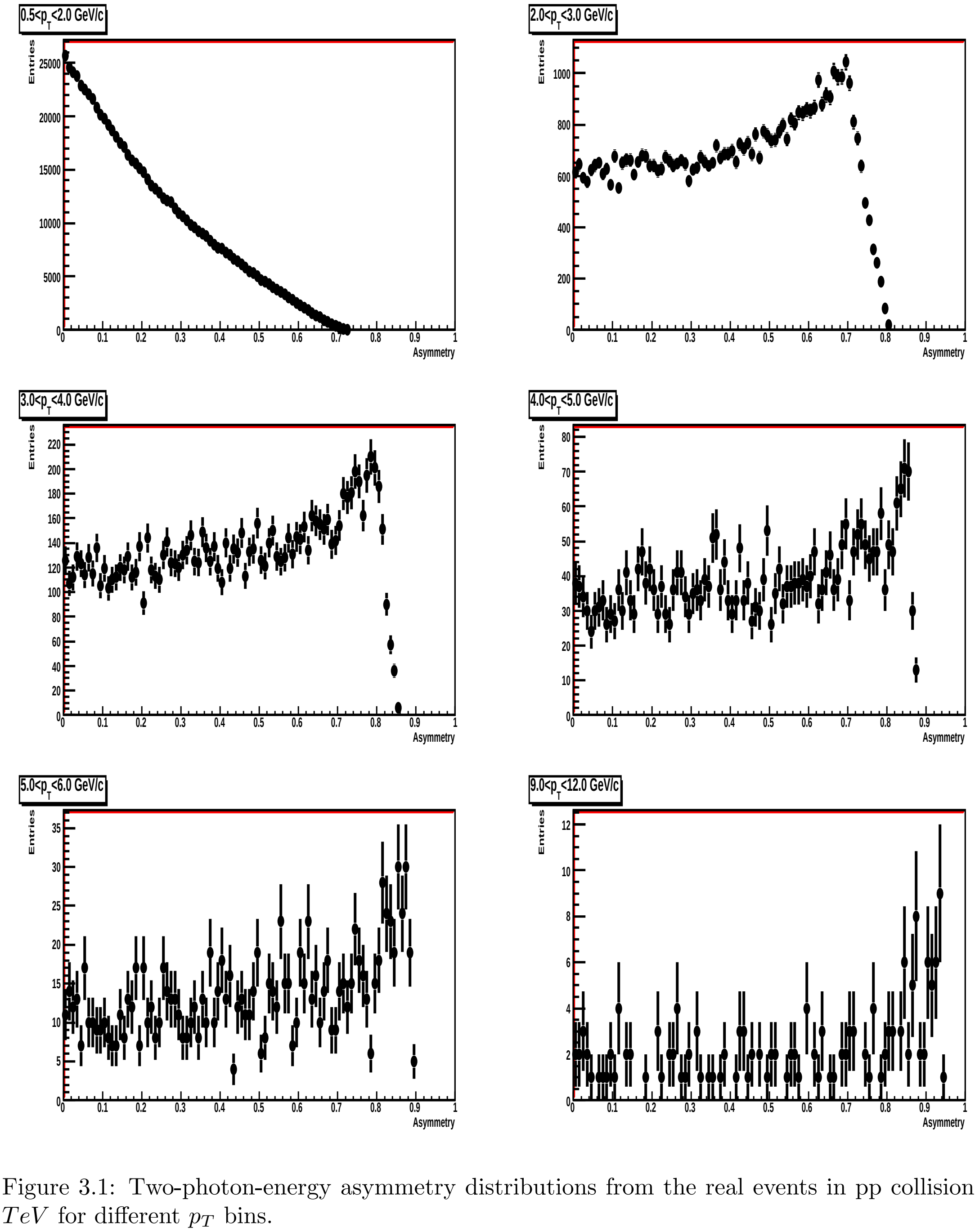

Figure 3.1: Two-photon-energy asymmetry distributions from the real events in pp collisions at 7 TeV for different p_T bins.

which are not originating from the parents of $\pi^0(\eta)$ will produce a combinatorial background. By the mathematical fitting or using the mixing event technique (which construct the uncorrelated photon pairs from adjacent buffer events with the similar features), it allows us to subtract the background as well as to estimate the systematic uncertainty by comparing different extraction methods. Two kinematic cuts of the energy asymmetry cut

$$\alpha = \frac{|E_1 - E_2|}{E_1 + E_2} \tag{3.3}$$

and distance cut

$$\Delta R = \sqrt{(\phi_1 - \phi_2)^2 + (\eta_1 - \eta_2)^2} \tag{3.4}$$

between to the two decay photons can be used for the photon pairs selection. For each decay photon pairs from $\pi^0(\eta)$ the minimum opening angle

$$tan\theta_{12} = \frac{m}{p}, \tag{3.5}$$

where m is the $\pi^0(\eta)$ mass and p its momentum, where $p \simeq p_T$ in ALICE central calorimeters. These cuts will improve the signal-to-background ratio, especially in heavy-ion collisions. In current pp analysis, only the two-photon energy asymmetry cuts are used and its dependence on p_T from the real data in pp collisions at 7 TeV are shown in Fig. 3.1.

Mathematical fitting

A direct way to extract the signal from the real events consists in using mathematical fit. However, the method is only valid under two prerequisites: a) the signal over background (S/B) or the significance ($S/\sqrt{S+B}$) stays at an acceptable level; b) the shape of the background has been well understood.

As show in Fig. 3.2(a), the π^0 peak and its combinatorial background can be fitted by a Gaussian plus a polynomial function

$$f(m) = A \cdot e^{\frac{-(m-\overline{m})^2}{2\sigma}} + a_0 + a_1 m + a_2 m^2 + a_3 m^3 + ..., \tag{3.6}$$

where the Gaussian function describes the signal, while the polynomial function describes the background. The number of $\pi^0(\eta)$ is counted by the integration of the Gaussian fitting function as:

$$N = \frac{A \cdot \sigma \cdot \sqrt{2\pi}}{\Delta m} \tag{3.7}$$

and the error is calculated by propagating the errors from the above formula:

$$N_{error} = N \cdot \sqrt{(\frac{eA}{A})^2 + (\frac{e\sigma}{\sigma})^2}, \tag{3.8}$$

where eA and $e\sigma$ denote the fit uncertainties of A and σ separately. An additional Crystal Ball parameterization includes a Gaussian core portion and a power-law tail below a certain threshold as:

$$f(x) = N \begin{cases} exp(-\frac{(x-\bar{x})^2}{2\sigma^2}), & \frac{x-\bar{x}}{\sigma} > -\alpha \\ A(B - \frac{x-\bar{x}}{\sigma})^{-n}, & \frac{x-\bar{x}}{\sigma} \leq -\alpha \end{cases}$$

where $A = (\frac{n}{|\alpha|})^n \cdot exp(-\frac{\alpha^2}{2})$ and $B = \frac{n}{|\alpha|} - |\alpha|$. With this fitting function plus a polynomial function, as shown in Fig. 3.2(b), the distribution can be fitted quite well. It offers us a crosscheck to other methods.

Mixing event procedure

Another way to subtract the background is by using of mixing event procedure. This becomes crucial in heavy-ion collisions due to the smaller signal-over-background ratio. The general procedure is shown in Fig. 3.3 and described as below:

- Real events: Loop the photon pairs in one event to get the signal+background $f_{real}(p_T, m_{2\gamma})$.
- Mixing events: Select events with similar properties (centrality, event plane etc.). Then pick up a photon from the current event and a photon from the other events to construct the uncorrelated photon pairs $f_{mix}(p_T, m_{2\gamma})$. Usually the size of event buffer is about 10 $\sim$ 100 and 5 $\sim$ 10 in pp and AA collisions separately depending on the computing resource.
- Normalization of the mixed background. Because of the two multiple photon pair combinations, it is necessary to normalize the mixed background properly to be subtract from the real events. Based on the fact that the background outside of the $\pi^0(\eta)$ nominal mass should have a similar shape. In each p_T bin, we first fit the ratio of the two invariant mass distributions

  $$f_{ratio}(m_{2\gamma}) = \frac{f_{real}(m_{2\gamma})}{f_{mix}(m_{2\gamma})} \tag{3.9}$$

  by a first/second order polynomial function in a range which should be outside of the $\pi^0(\eta)$ nominal mass. Then we use this function to normalize the mixed background.
- Counting the numbers: The background is subtracted as:

  $$f_{sig}(m_{2\gamma}) = f_{real}(m_{2\gamma}) - f_{ratio}(m_{2\gamma}) * f_{mix}(m_{2\gamma}). \tag{3.10}$$

  The number of $\pi^0(\eta)$ is calculated by the integration of $f_{Sig}(m_{2\gamma})$ in their nominal mass window ($\overline{m} \pm n\sigma$):

  $$N = \int_{m_0-3\sigma}^{m_0+3\sigma} f_{Sig}(m_{2\gamma}) dm_{2\gamma}. \tag{3.11}$$

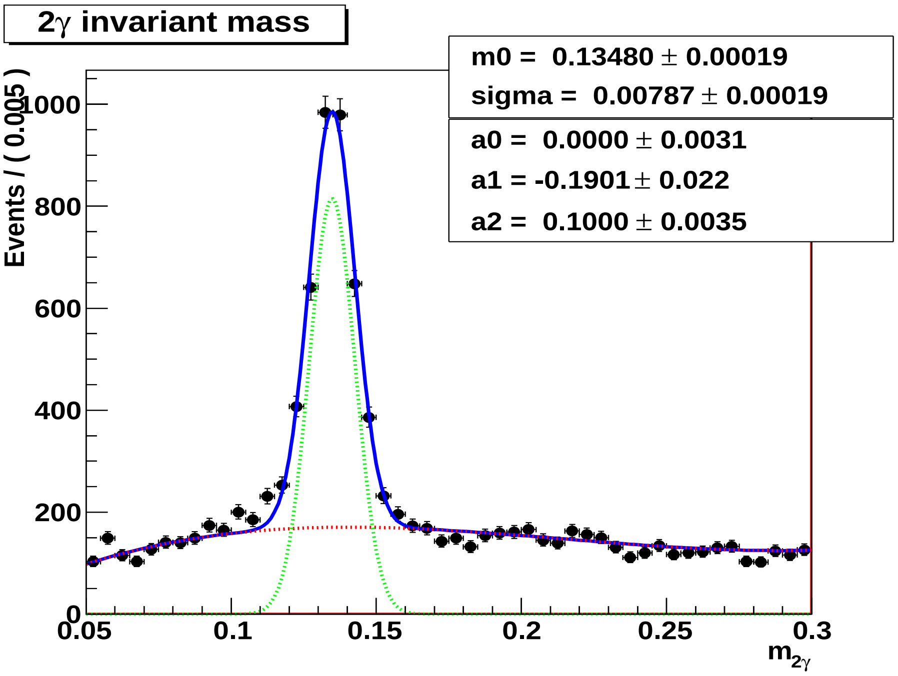

(a) Gaussian + Pol2

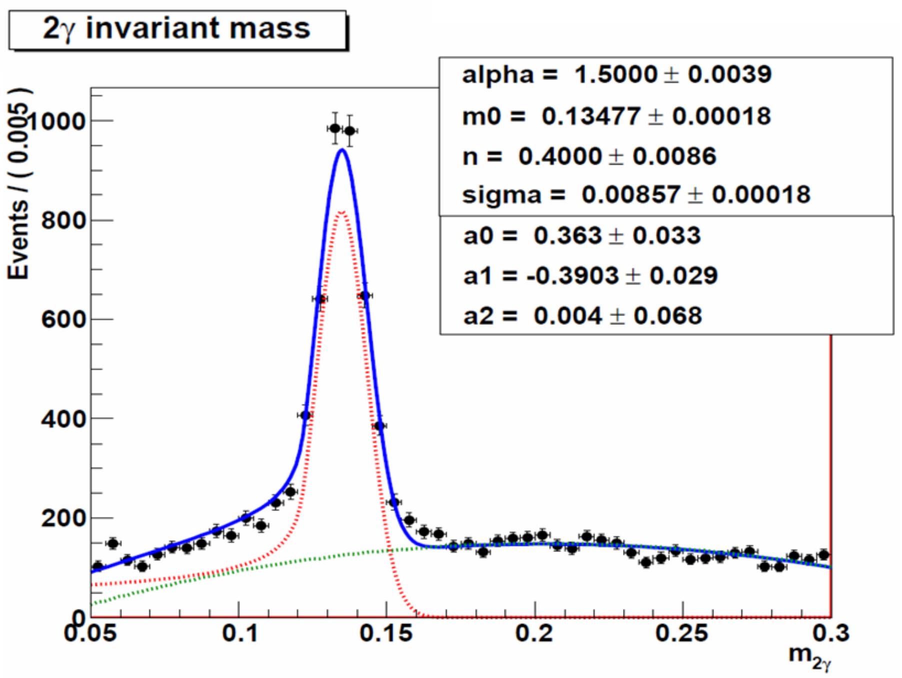

(b) Crystal ball + Pol2

Figure 3.2: Signal extraction for 2γ real distribution by using two fitting functions 1) Gaussian and second order polynomial, b) Crystal Ball and second order polynomial.

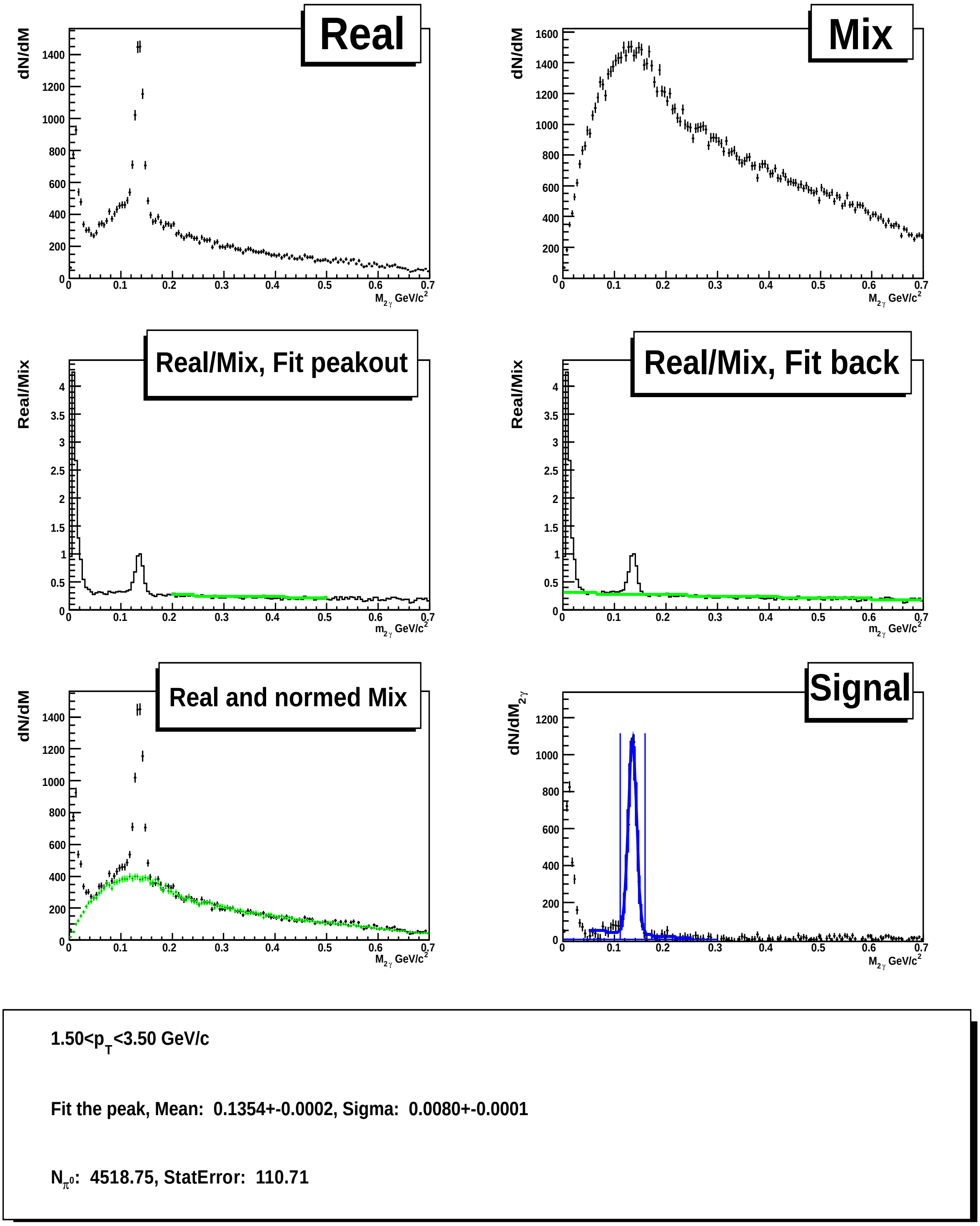

$1.50<p_T<3.50$ GeV/c

Fit the peak, Mean: 0.1354+-0.0002, Sigma: 0.0080+-0.0001

N_{π^0}: 4518.75, StatError: 110.71

Figure 3.3: The procedure of the signal extraction at $1.5\ GeV/c < p_T < 3.5\ GeV/c$ by mixing event technique. The data sample is taken from pp collisions at $7\ TeV$ with PHOS.

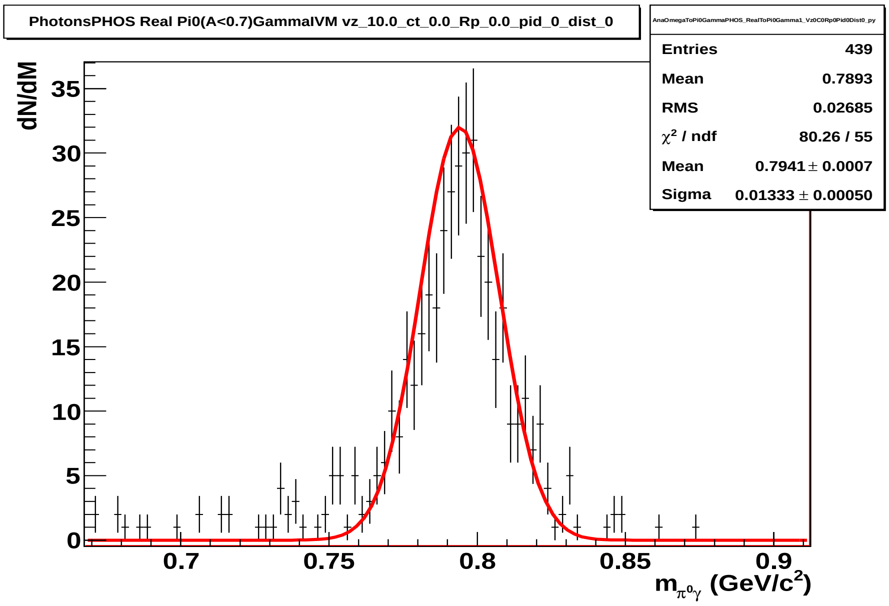

Figure 3.4: The reconstruction of the $\omega(782) \to \pi^0\gamma$ with the single particle event simulation going through the PHOS detector.

3.1.2 $\omega(782) \to \pi^0\gamma$

The reconstruction of $\omega(782) \to \pi^0\gamma \to 3\gamma$ follows two steps:

1) Select the π^0 candidates (the invariant mass of the photon pair in the range $[m_0 - n\sigma, m_0 + n\sigma]$) in one event by using the invariant mass analysis described in the previous section.

2) Loop on the third photon with the π^0 candidates to construct the invariant mass of $m_{\pi^0\gamma}$.

Fig 3.4 shows the validation of the reconstruction procedure with the single $\omega(782)$ particle event with PHOS. However in pp collisions, the $\omega(782) \to \pi^0\gamma$ channel S/B is worse than for $\pi^0(\eta) \to 2\gamma$. Besides, due to their three body decay, the background is complicate to be described by the mixing event technique. In my study, three different methods were examined based on the mixing event:

- $\gamma_{im} + \gamma_{in} + \gamma_{jl} = \pi^0_i + \gamma_{jl}$.
- $\gamma_{im} + \gamma_{jn} + \gamma_{jl} = \pi^0_{ij} + \gamma_j$
- $\gamma_i + \gamma_j + \gamma_k = \pi^0_{ij} + \gamma_k$

Note that in the above three items, i, j, k denote the nth event and m, n, l denote n photon from a event. Unfortunately, they are not yet enough to extract the signal. Thus the raw yields will be extracted by fitting the slices of the invariant mass distribution as describe for π^0 (η).

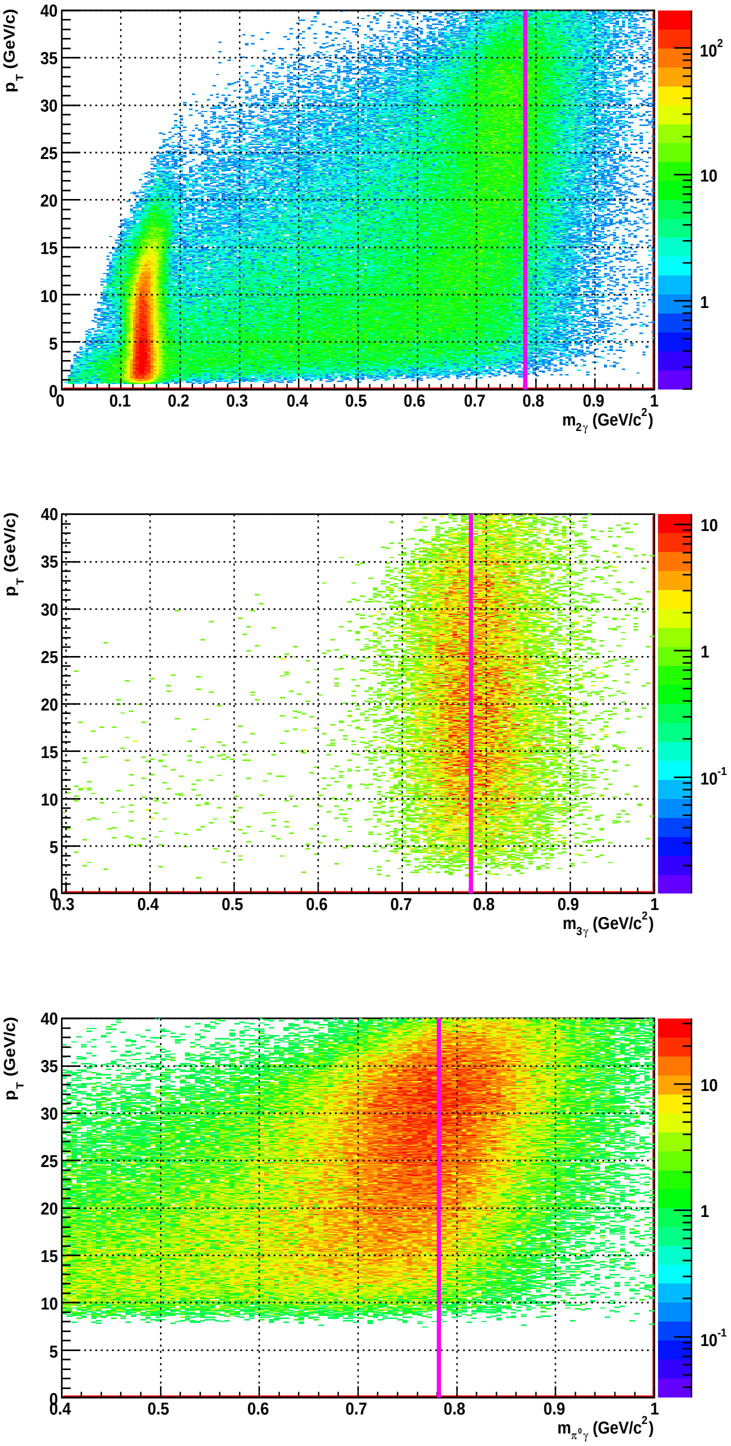

Figure 3.5: The reconstruction of the $\omega(782) \rightarrow \pi^0\gamma$ with the single particle event simulation going through the EMCAL detector. Top: 2γ invariant mass distribution; Middle: $\pi^0\gamma$ invariant mass; Bottom: 2γ invariant mass distribution with an assumption that clusters $p_T > 8\ GeV/c$ are overlapped π^0s

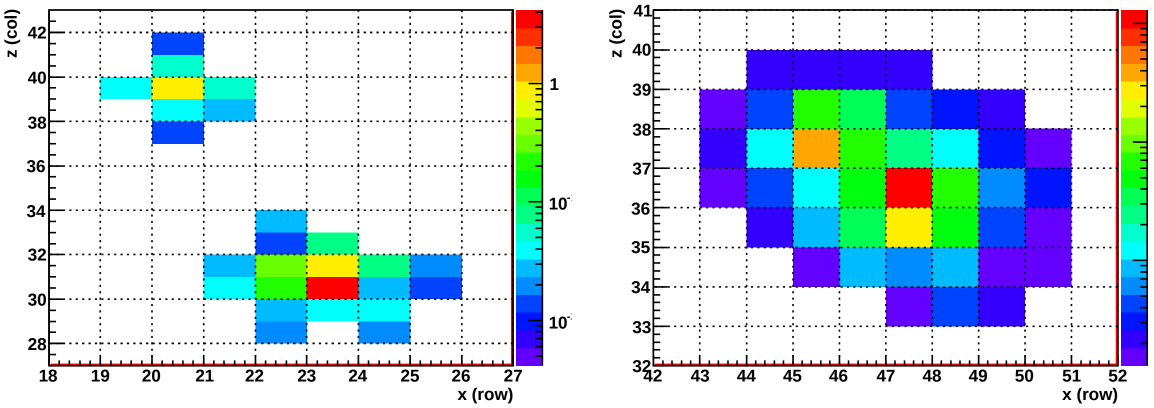

Figure 3.6: The simulation of the clusters from $\pi^0 \to 2\gamma$ at 4 GeV/c (left) and 32 GeV/c (right) in PHOS (x, z) plane. At lower p_T the two decay photons can be well separated while at higher p_T the two decay photons are merged as single cluster.

Additional method has been developed to construct the invariant mass of $\pi^0\gamma$ based on the fact that the two decay photons from high p_T π^0 are overlapped to be a single cluster. Thus we can assume that high p_T clusters are overlapped π^0s when the cluster unfolding algorithms and shower shape parameters do not disentangle. Then we loop it with a second cluster to reconstruct the invariant mass. The simulation was done with a single $\omega(782)$ per event going through EMCAL detector. As shown in Fig. 3.5, top: the 2γ invariant mass distribution as a function p_T; middle: the $\pi^0\gamma \to 3\gamma$ invariant mass distribution; bottom: the 2γ invariant mass distribution with an assumption that the clusters $p_T > 8$ GeV/c are overlapped π^0. The combinatorial background will be improved with the help of the shower shape analysis. This method is weakly dependent on the cluster unfolding algorithm for ω at $p_T > 10$ GeV/c, especially for EMCAL.

3.2 Shower shape analysis

When going to higher p_T, > 20 GeV/c for PHOS and > 5 GeV/c for EMCAL, the two decay photons start to overlap and may be misidentified as single cluster as shown in Fig. 3.6 for π^0 at 4 GeV/c (left) and 32 GeV/c (right). The unfolding algorithm (see more details in next chapter) becomes thus essential to separate the two clusters. However, it's still not enough to unfold the overlapping clusters in the whole momentum range. At the intermediate p_T, with such overlapping clusters, the shower shape parameters become measurable evolving from a circular shape when a single photon presents to an elliptic shape when a π^0 is produced.

Based on the shower topology, the shower shape parameters, such as the shower

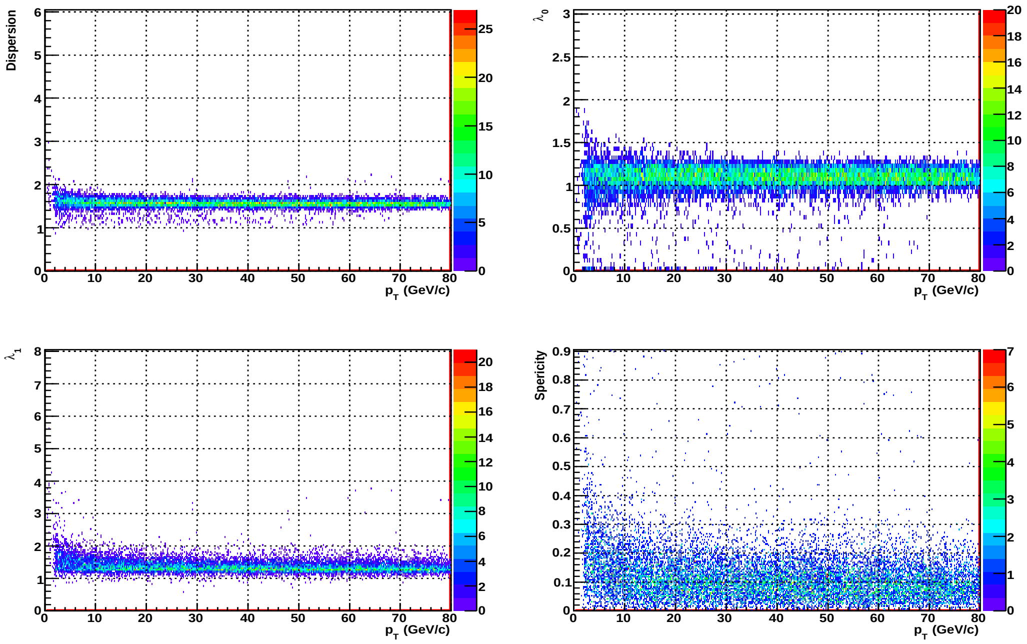

Figure 3.7: γ: The shower shape parameters behavior simulated by the single particle event with $2\ GeV/c < p_T < 80\ GeV/c$ going through PHOS detector.

dispersion(disp), the two principal axes(λ_0 and λ_1) and the shower spericity ($\varepsilon = \frac{|\lambda_0 - \lambda 1|}{\lambda_0 + \lambda_1}$), are defined and employed for the particle identification. More details on cluster reconstruction and shower shape shape parameters definition can be found in next chapter. Here the simulation studies of shower shape with different kind of particle in a wider p_T range [2, 80] GeV/c is presented.

We use the AliGenBox [136] generator to produce the particles shotting the calorimeter coverage of $\eta = [-0.1, 0.1]$ and $\phi = [270°, 310°]$ which are narrower than the actual geometrical acceptance to reduce the geometrical edge effect. At a first step, to minimize the influence from the conversions caused by the ahead materials and magnetic field, all the other detectors and L3 magnet are switched off except for PHOS and EMCAL with the real geometry configuration as in the data-taking period 2009∼2010.

The charged hadrons contamination for the photon measurement is mainly from the charged pion, proton, muon and neutron. Here we just simulate shower shape by simulation with the γ, π^0 and π^+.

Fig. 3.7, 3.8 and 3.9 show the shower shape parameters behavior simulated by the single particle event at a wider p_T range [2, 80] GeV/c going through the PHOS detector. Because of the strong interaction between the charged hadrons and electromagnetic calorimeters, larger hadron showers are produced with a fraction of their original energy deposition at $p_T < 20\ GeV/c$. Combining the track matching and the shower shape will allow to reject the charged hadron contamination. Here we focus

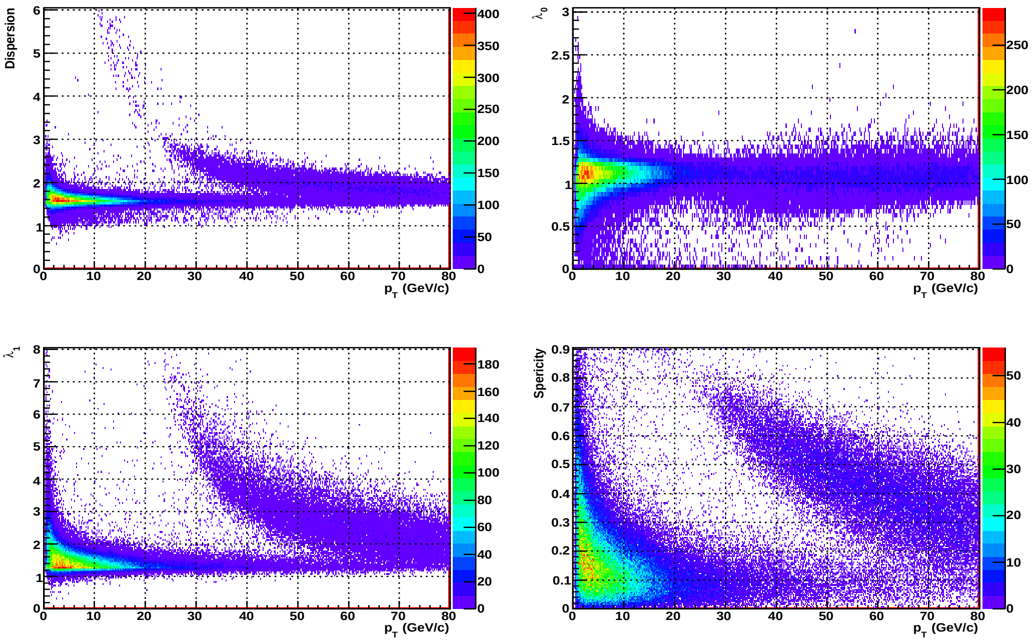

Figure 3.8: π^0: The shower shape parameters behavior simulated by the single particle event with $2\ GeV/c < p_T < 80\ GeV/c$ going through PHOS detector.

on the identification of γ and π^0.

For γ, shower shape parameters show a weak p_T dependence, while there is an obvious dependence for π^0. The mean value of parameters for γ are: $\overline{D^\gamma} \sim 1.56\pm0.06$, $\overline{\lambda_0^\gamma} \sim 1.09\pm0.09$, $\overline{\lambda_1^\gamma} \sim 1.32\pm0.09$, and $\overline{\epsilon^\gamma} \sim 0.10\pm0.06$. While for π^0, a well separation from the D, λ_1 and ϵ can be seen in Fig. 3.10. In this way, it allows us to identify the overlapped π^0 to a p_T range of 40 GeV/c with a dispersion cut >1.7, 50 GeV/c with a λ_1 cut>1.6 and 70 GeV/c with the shower eccentricity cut >0.15 for PHOS.

3.3 Isolation cut method

When the p_T of $\pi^0(\eta)$ increase further, the two decay photons are completely overlapped to a single cluster and this becomes a challenge for $\pi^0(\eta)$ identification at higher p_T, $> 50\ GeV/c$ for PHOS and $> 30\ GeV/c$ for EMCAL. It will cause the main source of systematic uncertainty for direct photon and $\gamma - hadron$ correlation measurements.

The isolation cut method [137,138] originates from topology consideration induced by the initial hard processes at leading order of Compton scattering ($q(\overline{q})+g \rightarrow \gamma+g$) and annihilation ($q+\overline{q} \rightarrow \gamma+g$). Ideally, the γ is isolated in one side without other hadrons around, in its opposite the parton jet then fragment to hadrons. In this way, the photon which is isolated can be tagged as prompt photon. While for the

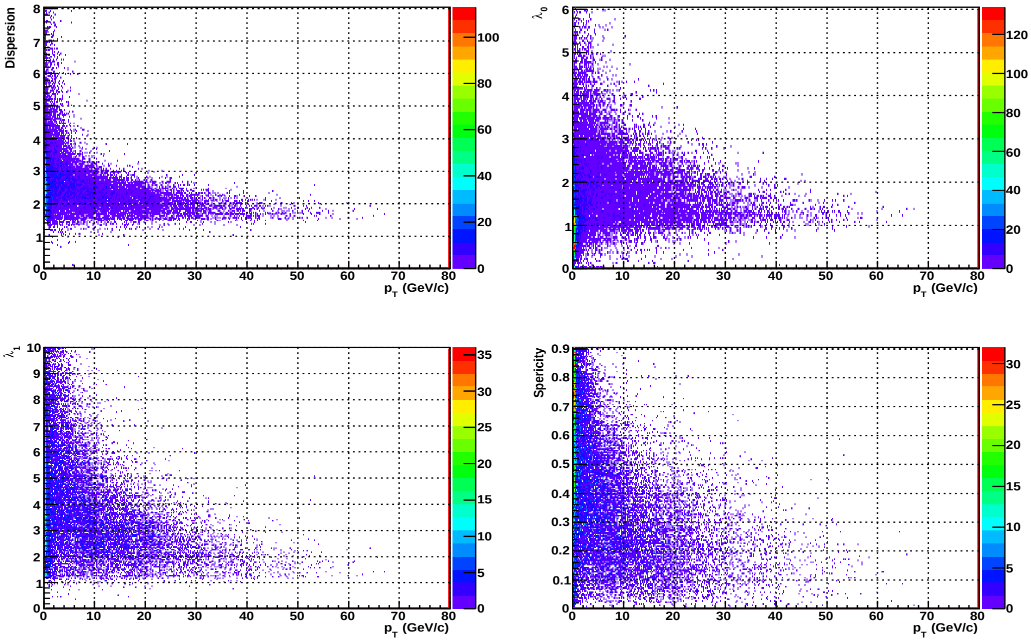

Figure 3.9: π^+: The shower shape parameters behavior simulated by the single particle event with $2\ GeV/c < p_T < 80\ GeV/c$ going through PHOS detector.

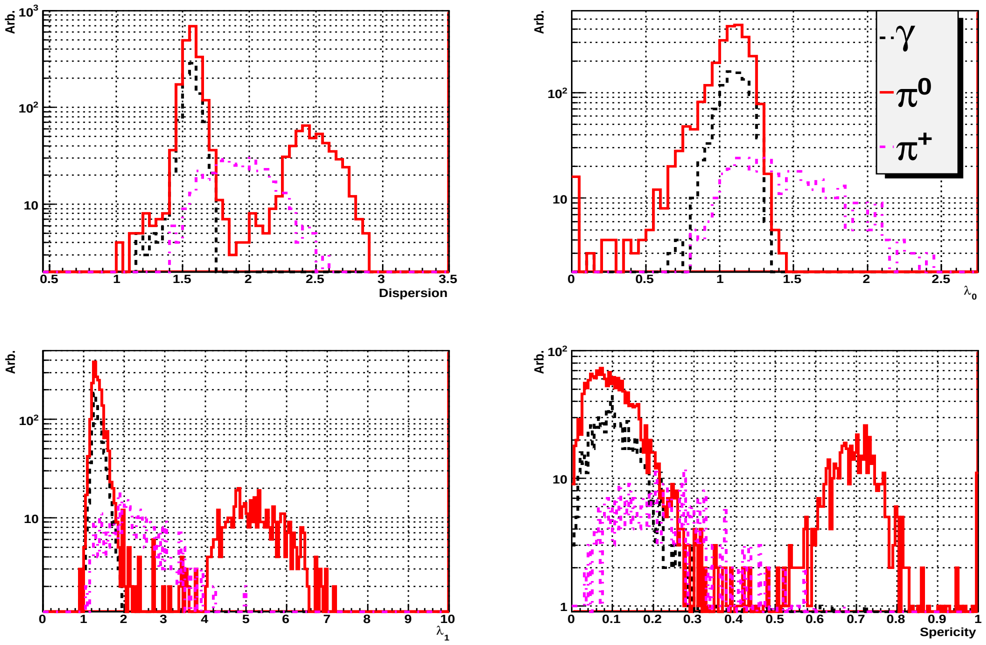

Figure 3.10: Comparison of the shower shape parameters behavior with γ, π^0 and π^+ at $28\ GeV/c < p_T < 32\ GeV/c$ simulated by the single particle event going through PHOS detector.

next leading order such as bremsstrahlung photons are always accompanied by nearly collinear hadrons on the same side. However, the underlying events may disturb this perfect scheme even more violently in heavy ion collisions and additional corrections need to be taken into account.

The starting point to tag the isolated photon is to study its surrounding hadrons kinematics within a cone $R = \sqrt{(\phi - \phi_\gamma)^2 + (\eta - \eta_\gamma)^2}$ of the photon candidate. According to this idea, two different select criteria have been developed:

I) No hadron in the cone of photon candidate with a p_T larger than a given threshold p_T^{th}.

II) The total of the transverse momentum ($\Sigma_{p_T}^h$) of all hadrons inside the cone should be smaller than a given threshold $\Sigma_{p_T}^{th}$.

From the algorithm, three free parameters of R, p_T^{th} and $\Sigma_{p_T}^{th}$ are prior unknown, which were optimized by simulation. A series studies had been taken and validated with ALICE PHOS and EMCAL detectors [142, 143].

By using the isolation cut method, the prompt photons can be tagged. In a indirect way, by subtracting the prompt photons from the inclusive photon spectrum at higher p_T ($> 50\ GeV/c$), the residual photons are overlapped/disentangled $\pi^0(\eta)$. More and exhaustive simulation study is needed for this part.

The combination of the isolation cut method and shower shape analysis simultaneously allows to enhance the γ/π^0 separation at higher p_T to hundred GeV/c.

Chapter 4

Data processing chain

In this chapter, we focus on the data processing chain from raw data reconstruction to the calculation of the particle kinematics for physics analysis [1]. The reconstruction procedure consists in four steps: 1) Decoding raw data to extract the signal amplitude and time information; 2) The clusterization and cluster unfolding to reconstruct the position and energy of the incident particles; 3) Construct the track segments by connecting the CPV-EMC or collisions vertex to EMC cluster position; 4) Particle identification.

4.1 Raw data

The raw data are recorded from ALICE data acquisition system based on a data-driven approach [129]. For every bunch crossing in the LHC machine, the central trigger processor decides in less than one microsecond whether or not to collect the data resulting from a particular collision. The trigger decision will be distributed to FEEs. The FEEs are located as close as possible to the detectors to format and validate the raw data at the local level by the corresponding Local Trigger Unit (LTU) and an optical broadcast system: the Trigger, Timing and Control system (TTC). All the accepted events are delivered via a customer-designed point-to-point optical link called Detector Data Link (DDL) to a Local Data Concentrator (LDC). The LDCs validate the events and perform local event building when they receive multiple incoming DDLs. Meanwhile, it compresses the data and finally move the raw data to the event builder running on a Global Data Collector (GDC). Then the Permanent Data Storage (PDS) records the data from GDCs and also provide the access to the event data for all successive analysis stages.

The ALICE DAQ software framework DATE (ALICE Data Acquisition and Test Environment) was developed during the detectors construction and testing phase. During the real data-taking, the ROOT format is employed to minimize the data size and keep accordance with the analysis framework, which is a starting point for offline analyzers.

---

[1] The study was reported at the conference of Calor2010 in Beijing, China.

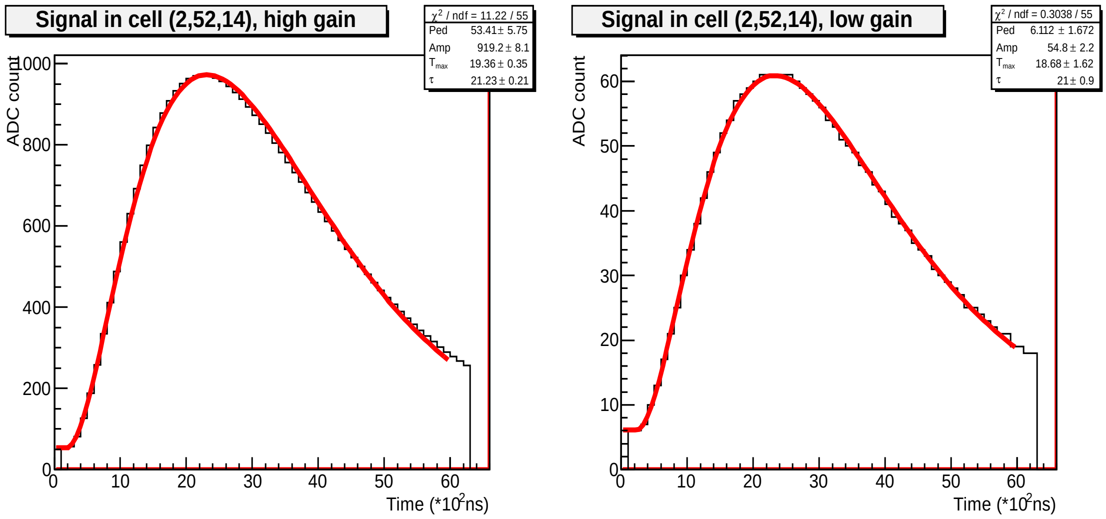

Figure 4.1: Signal extraction with PHOS cell (2, 52, 14) of two gains from the real data. The shapes are fitted by a $\Gamma - 2$ function with the fixed order n=2.

4.2 Signal extraction

4.2.1 Amplitude and timing

For the ALICE EM-calorimeters, the signal shaper after the decoding of the raw data is illustrated in Fig. 4.1 from data with run 138225, which can be fitted by the $\Gamma - 2$ function

$$f(t) = Ped + Amp \cdot t^n \cdot e^{-2t+2} \tag{4.1}$$

where $t = (t - T_{max} - \tau)/\tau$, Ped is the signal pedestal level, T_{max} is the time when the signal arrives at its maximum, τ is the peaking time of the shaper and Amp is the signal amplitude after subtracting the pedestal. In addition, other fitting functions were tested to estimate the signal extraction performance, e.g.

$$f(t) = Ped + Amp \cdot (dt^n e^{-\alpha dt} + b \cdot dt^2 e^{-\beta dt}) \tag{4.2}$$

where $dt = t - t_0$, and t_0 is the initial start time of the signal.

However, it is time consuming to precisely extract the signal by the above fitting function. An alternative coarse and fast way called $k - level$ method is used as the procedure below:

1) The signal energy (in ADC count) is a value that the maximum sample minus the pedestal for a detection channel read from Offline Condition DataBase (OCDB);

2) Calculate the k-level by a linear function $k\_level = pedestal + k * energy$. Usually, k=0.35;

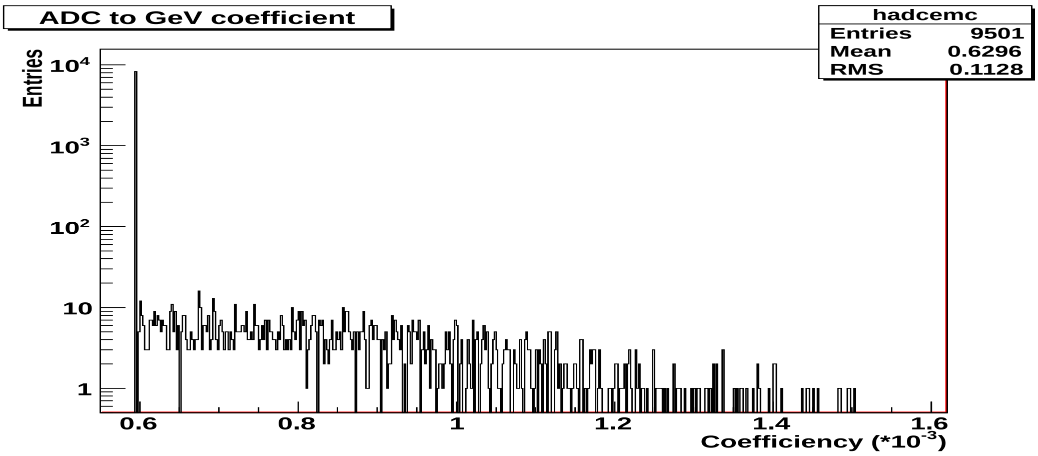

Figure 4.2: The coefficient from amplitude to energy conversion vary from cell-to-cell with PHOS. Here it shows the coefficient distribution, which is stored in OCDB during the run period 2009∼2010 with run number 130850.

3) By using the least square method to find the crossing point between the k-level and signal shape and determine the shape slope (c_1) and offset (c_0) around the crossing point;

4) Calculate the signal time by $(k\_level - c_0)/c_1 - 5$, where 5 is the mean offset between k-level and start time.

The uncertainty due to the extraction method stays at a few percent level, which can be compensated by the latter calibrations and non-linearity corrections.

4.2.2 From amplitude to energy

The conversion for the cell signal from amplitude (in ADC count) to energy (in GeV) is determined by the absolute energy calibration. The coefficient varies cell-by-cell which has been pre-defined and stored in OCDB and its distribution shown in Fig. 4.2. It is about 6 MeV per ADC count for most of detection channels.

4.3 Calibration of PHOS and EMCAL

To achieve the physics goals and take fully advantage of calorimeters, it is required to calibrate the energy measurement at a reasonable level. Technically speaking, there are absolute and relative calibrations. The absolute calibration aims to scale the energy, which would be a a dominant systematic error on cross section measurements. While the relative calibration aims to make all the detection channels have an uniform response for a given energy deposit.

In ALICE, a sophisticated calibration strategy in different stages by cosmic rays, beam test, LED and physics data-taking are used. As designed for both PHOS and

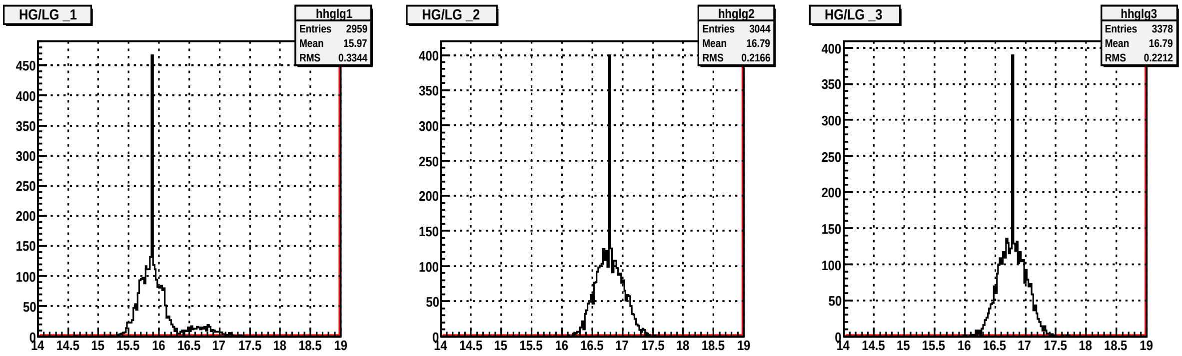

Figure 4.3: HG/LG ratio for PHOS registered in OCDB during the run period 2009∼2010 with run 130850.

EMCAL, each detection channel has two gains with a ratio of $HG/LG \sim 16$, which provides us a first calibration at the electronic level. For the calorimeters, uniforming the MIP (minimal ionizing particle) position produced by the cosmic μ, measuring the invariant mass peaks for known resonances and short lived particle (π^0, η), the energy-momentum matching for electrons measured in calorimeters and tracking detectors, are general methods used.

4.3.1 High and low gain ratio by LED

Concerning PHOS and EMCAL, to cover a large momentum range there are two APD gains for each detection channel with a ratio of $HG/LG \sim 16$ in design. Fig. 4.3 shows the HG/LG distribution with PHOS, which is derived from the LED events. The results are stored in OCDB to be used in the event reconstruction. The mean values are 15.97 for module 1 (was installed in 2006) and 16.79 for module 2 and 3 (were installed in 2008 with some changes of electronic configurations).

4.3.2 Beam test

To understand precisely the detectors, it is nevertheless necessary to calibrate the calorimeters by using the external and specified test beams. However, due to some constrains, only one PHOS module was tested at T10 beam line of CERN-PS in the summer of 2006. Several beam counters and an electron identification gas counter are used in the beam line. The first PHOS module was put on a moving stage so that the beam can be shot into any positions of the PHOS module (x, z) surface. The monochromatic electrons with 2 GeV energy are irradiated into most of channels for channel-by-channel energy calibration. Meanwhile, the APD bias was successfully adjusted to equalize the gain up to a accuracy of 4%. Besides, the beams of electron with 1∼5 GeV/c and π^- with 5 GeV/c were also generated to investigate the energy

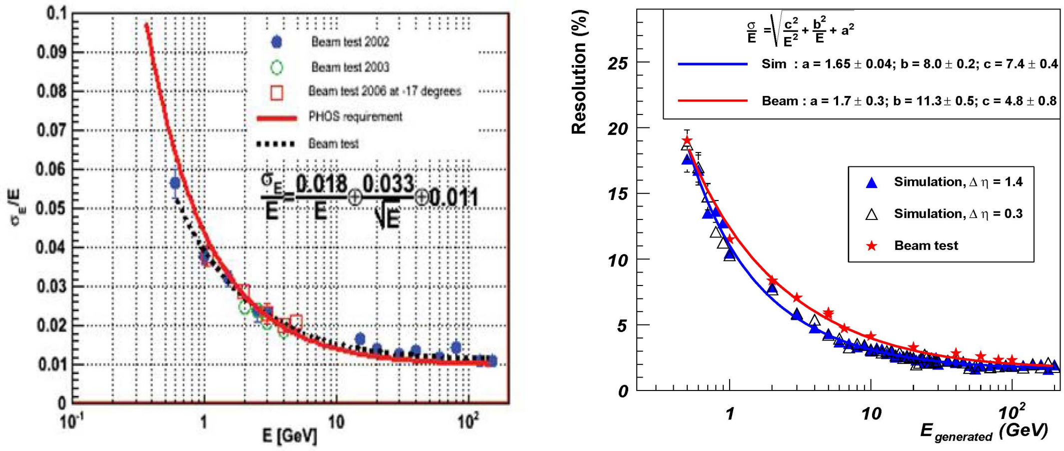

(a) PHOS (b) EMCAL

Figure 4.4: Energy resolution for PHOS (a) and EMCAL (b).

resolution and their shower shape. No beam test for the other two modules, however, the initial calibration was done based on the APD gains provided by the manufacture.

While for the EMCAL super-modules, no beam test was taken before the LHC first data-taking. One EMCAL prototype with 64 towers (8×8) was tested on July 2010 at CERN-PS T10 beam line. The beam provided electrons over a large momentum range from 1 GeV/c to hundred GeV/c, also with protons and pions. The analysis is still ongoing to provide a precise correction function for the real data analysis. The detector energy resolutions are shown in Fig. 4.4 for PHOS and EMCAL with the latest test beam results.

4.3.3 Cosmic rays μ

The composition of cosmic rays in space are mainly charged nuclei dominated by protons. When going through the atmosphere, they interact with the atmospheric nuclei and produce a vast majority of pions. Lot of those pions then decay to muons to penetrate and arrive at the ground level. The average muon energy at sea level is about 4 GeV. More detailed can be found in [95].

When the μ goes through the electro-magnetic calorimeters, it suffers a weak interaction and produce a minimal ionizing particle about 250 MeV/c. By using of this information, the basic idea by using the cosmic μ to calibrate the detector is to collect the energy distribution for all the detection channels and put the peaks to the same position. It is a free source, however, it only calibrates well at low energy. Some cosmic rays tests had been taken during 2007~2010 for PHOS and EMCAL.

4.3.4 E/p measurement by electrons

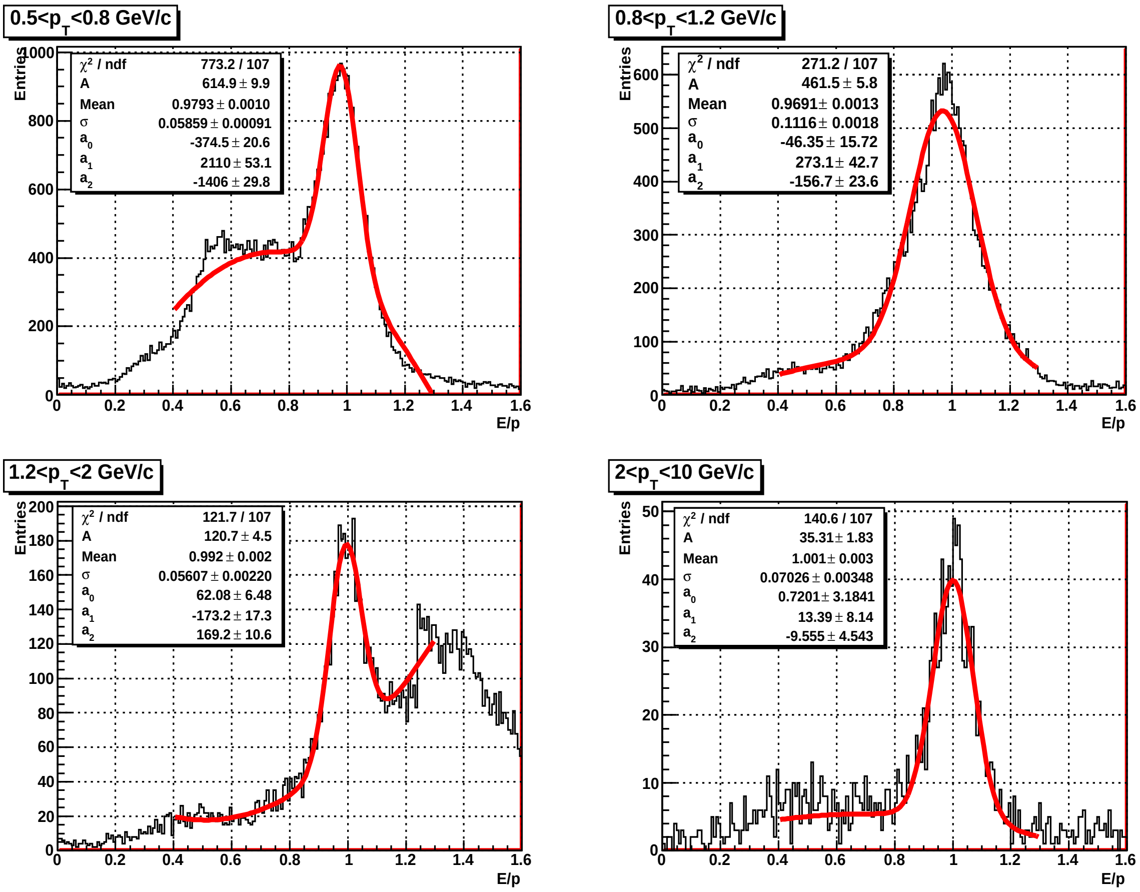

Figure 4.5: E/p with PHOS from real data at four p_T bins of the clusters [0.5, 0.8], [0.8,1.2], [1.2, 2] and [2, 10] GeV/c. The standard track cuts and $65 < dE/dx < 80$ in TPC are used for the track selections. The curves are fitted by a gaussian and second order polynomial function.

ALICE tracking detectors have an excellent momentum measurement for the charged particles at a wider momentum range. Using the electrons, we measure their momentum in the central tracking detectors and energy in EM-calorimeters. It provides an effective approach for the calibration of the EM-calorimeters. Ideally, the value of E/p should equal 1 for the electrons by ignoring its mass. Limited by the statistics from the data-taking, it is impossible to use them to calibrate the calorimeters cell-by-cell. However, it gives us an overall information on the calibration level.

The standard track cuts for the pp data analysis in 2010 is used and listed as below:

1. The number of clusters in TPC is larger than 70;

2. The χ^2 per cluster in TPC should be smaller than 4;

3. The ITS and TPC refit procedure is required;

4. At least one reconstructed point in SPD;

5. The maximum of DCA to vertex in Z direction is 2, while in XY direction is p_T dependent
$$f(p_T) = 0.0182 + \frac{0.035}{p_T^{1.01}}. \tag{4.3}$$

6. The energy loss dE/dx in TPC is required in a range [65, 80].

Fig. 4.5 shows the E/p distribution at different four p_T bins at [0.5, 0.8], [0.8,1.2], [1.2, 2] and [2, 10] with PHOS in pp collisions at 7 TeV. A clear peak can be seen round the unity. The charged hadrons may also deposit part of their energy and contribute to additional combinatorial background.

4.3.5 Calibration by using π^0 peak

Using π^0 to calibrate the EM-calorimeters is also one of the most precise strategies for its known mass ($\sim 135 MeV/c^2$) and abundant production. It requires a rather good pre-calibration to observe the π^0 peak. To reach an accuracy $\sim 1\%$ in relative calibration, we need at least 1000 π^0s in each cell and a equivalence of $2 \sim 4 * 10^9$ min-bias pp events. Apparently, it's not enough from the current statistics. NOTE that for PHOS, the π^0 peak position is used for the absolute energy calibration. It will be further illustrated in Chapter 6.

4.3.6 Bad channels map

It is inevitable that there are some bad/hot detection channels caused by the random electronics or operational defect. Based on the stringent criteria for the signal shape and the averaged behavior of the energy deposition, they are marked properly according to:

1) HG/LG ratio in LED runs for each channel with a large deviation to the designed value is marked as bad;

2) The channel that has a frequent larger/smaller mean and RMS of pedestals value in physics runs is marked as bad;

3) The raw signal is weird and can not pass the quality check;

4) Energy deposition on per cell in physics runs has a large deviation to the mean value is marked as bad;

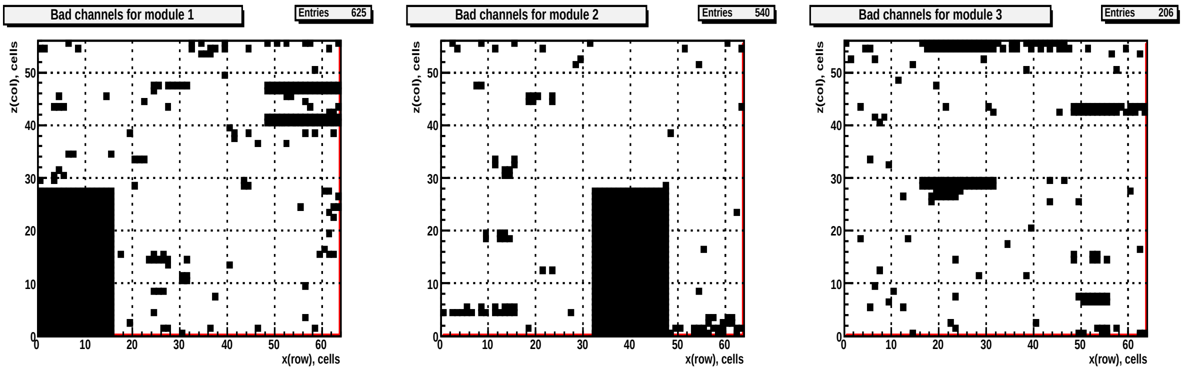

Figure 4.6: PHOS bad channels registered in OCDB with run 130850. In total, 1371 bad/hot channels in run period 2009-2010, which are excluded in the physics analysis.

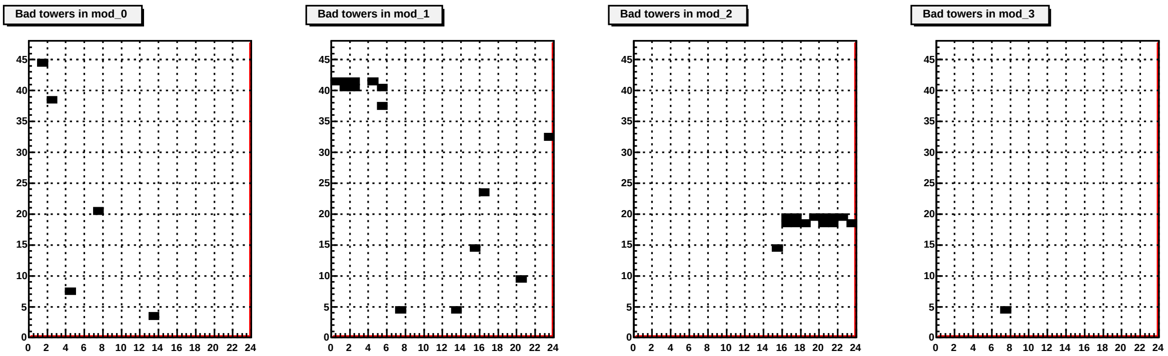

Figure 4.7: EMCAL bad towers registered in OCDB with run 130850. In total, 33 bad/hot channels in run period 2009-2010, which are excluded in the physics analysis.

5) Average value of cluster energy per cell in has a large deviation to the mean value is marked as bad;

Fig. 4.6 and 4.7 present the bad channel maps for PHOS and EMCAL respectively during the physics data-taking 2009∼2010 registered in OCDB with run number 130850. Totally, there are 1371 (12.75%) bad/hot cells including two destroyed branches for PHOS and 33 (0.7%) bad/hot towers for EMCAL. All of these information are put into OCDB to be excluded during the event reconstruction and physics analysis.

After the calibration, all the parameters such as : the HG/LG ratio, the *ADC* to *GeV* coefficient, the time shift are transfered into OCDB. It is crucial to ensure a correct event reconstruction taking into account the calibration and alignment parameters in a run-by-run bias.

4.4 Clustering

A cluster, resulted in when a crystal is fired by an incident particle, is composed by a group of adjacent cells with an energy deposition above a threshold. Due to the different technologies of PHOS and EMCAL, two different clustering algorithms are used for them. From the current situation that the EMCAL clustering and unfolding are still immature and need further investigation. Here PHOS algorithm will be discussed in short.

Required by the PHOS physics motivation, the cluster reconstruction should fulfill:

- Precise reconstruction of the incident particle position and energy deposit;
- Separation of electromagnetic (γ and electron) and hadronic showers;
- Identification and unfolding two or more overlapping showers.

4.4.1 Cluster finding

Any cell with an energy larger than a minimal energy value E_1^{th} (the noise threshold) is considered as a seed of a new cluster. The cluster is formed when there are other cells around this one whose energy is greater than E_2^{th}. If one of the cells which belongs to the cluster has a energy much higher than all the other cells a value of E_3^{th}, the cell is tagged as a local maximum. The simulation study turns out that the procedure is poor sensitive to the adjustable parameters E_2^{th} and E_3^{th}. In principle, one incidence particle will generate one local maximum in the cluster, so that two or more local maximum mean there are superposition of multiple showers. The cluster unfolding algorithm described below is needed.

4.4.2 Cluster unfolding

The unfolding algorithm deals with the clusters containing multiple local maxima with the most probability occurring in a high multiplicity environment. The basic idea is based on the knowledge of electromagnetic shower lateral distribution parameterized as

$$f(r,E) = e^{\left(-r^4 * \left(\frac{1}{2.32+0.26*r^4} + \frac{0.0316}{1+0.0652*r^{2.95}}\right)\right)}, \tag{4.4}$$

where r is the distance from the cell center to the incident point, and E is the energy deposition in one cell relative to the total energy. Assume there are N local maxima from the cluster, the pulse height A_i of the i^{th} cell is subdivided into A_i^1, A_i^2, ..., A_i^N following the formula:

$$A_i^k = A_i \cdot \frac{f(r_{ik,E_k})}{\sum_{j=1}^{N} f(r_{ij}, E_j)}. \tag{4.5}$$

More detailed on the cluster unfolding algorithms can be found in [108]. The procedure had been validated in simulation and real data. It demonstrates a good cluster unfolding capability to 25 GeV/c for PHOS. While for EMCAL, additional $N \times M$ cluster finding and unfolding algorithms are being developed.

4.4.3 Coordinates and energy reconstruction of an incident particle

The coordinates of the incident particle in the (x, z) plane are calculated using the center of gravity algorithm

$$\bar{s} = \sum_i s_i w_i / \sum_i w_i \tag{4.6}$$

with a logarithmic weight

$$w_i = max\ [0, w_0 + log(e_i/E)], \tag{4.7}$$

where the parameter w_0 is empirically determined. Due to the effective depth of the shower which increases logarithmically with energy, the additional correction is taken into account by using the function:

$$\Delta_x(mm) = -[a \cdot ln(E(GeV)) + b] \cdot sin\alpha, \tag{4.8}$$

where α is the angle between the normal to the detector and the incident particle. These parameters depend only on the radiation length of the detector material and are independent on the granularity.

The cluster energy is the sum of energy of cells which belong to the cluster. For each pp collision, the primary vertex can be reconstructed by correlating hits in

SPD. The resolution depends on the charged track multiplicity and is 0.1∼0.3 *mm* in the longitudinal and 0.2∼0.5 *mm* in the transverse direction. Knowing the cluster position, energy and direction from collision vertex, the particle four-momentum is reconstructed.

Fig. 4.8 shows an overview display of a PbPb event at 2.76 *TeV* for PHOS (x, z) plane for a better illustration of the data processing chain. Each column presents the modules 2, 3 and 4 of PHOS. The rows from above to bottom show the HG digits, LG digits, cell energy after the raw event reconstruction and the cluster energy.

4.4.4 Shower shape parameters

The shower shape analysis is an effective method to discriminate photons from the other charged hadrons. There are four main shower shape parameters: dispersion, two main axes and the sphericity as explained below.

Shower dispersion

The dispersion reflects the difference of the shower radial energy profile. It is calculated as:

$$D_s^2 = \frac{\sum w_i s_i^2}{\sum w_i} - \left(\frac{\sum w_i s_i}{w_i}\right)^2, \tag{4.9}$$

where s stands for the cell (x, z) coordinate, the w_i uses the same parameters as in Eq. 4.6. Then the final dispersion of the cluster is $D = \sqrt{D_x^2 + D_z^2}$.

Two main axes and sphericity of the shower

On the surface of PHOS the two main axes (λ_0, λ_1) are calculated by constructing a 2×2 sphericity tensor and solving its eigenvalues:

$$S_{xx} = \sum_i E_i x_i^2, \tag{4.10}$$

$$S_{xz} = S_{zx} = \sum_i E_i x_i z_i, \tag{4.11}$$

$$S_{zz} = \sum_i E_i z_i^2, \tag{4.12}$$

where x_i, z_i are the coordinates of cell ith of the cluster. Then the cluster sphericity is defined as:

$$S = \frac{|\lambda_1 - \lambda_2|}{\lambda_1 + \lambda_2}. \tag{4.13}$$

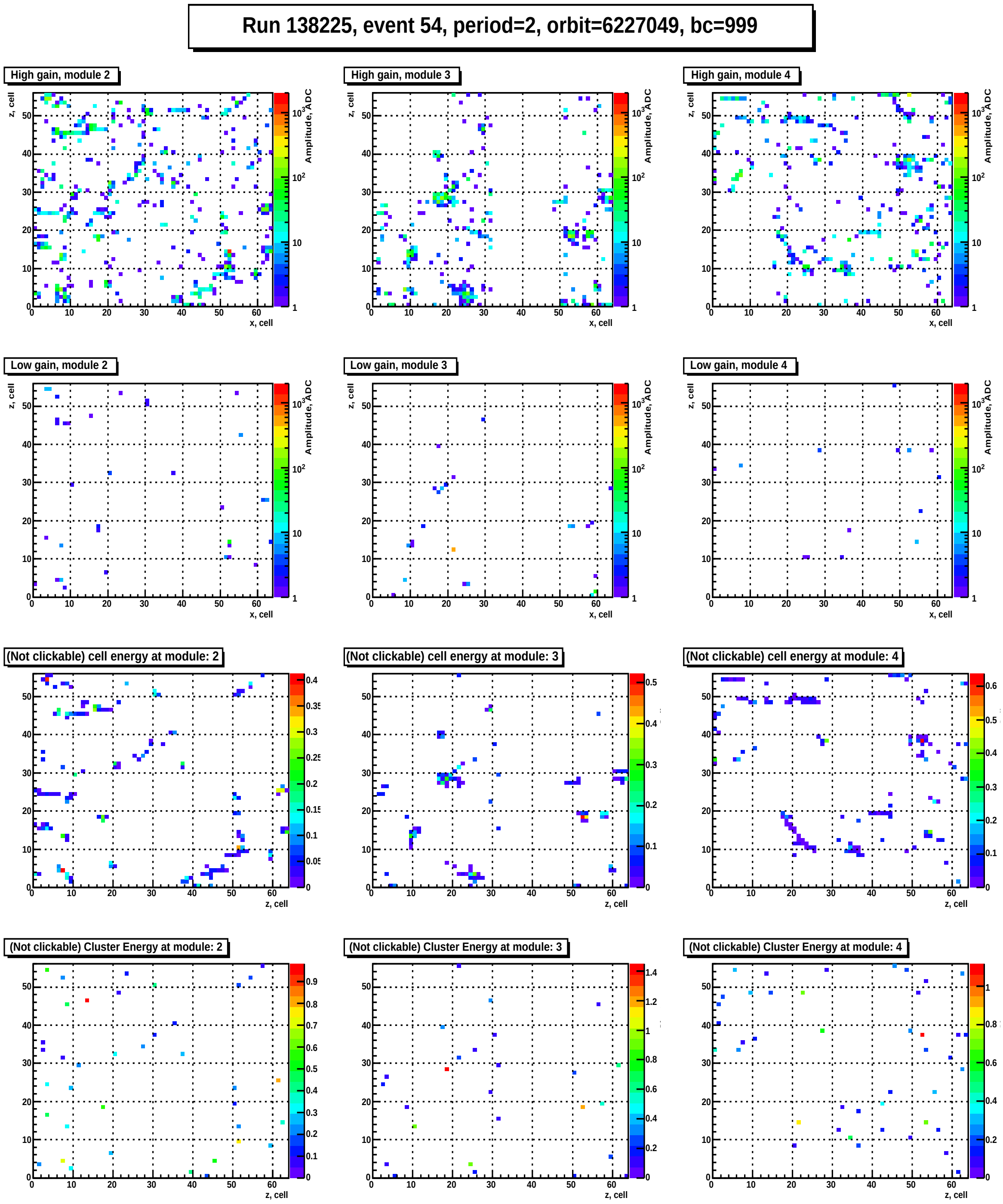

Figure 4.8: An illustration of the procedure from raw data to ESD in ALICE PHOS for a PbPb event. Each right shows the module 2, 3 and 4 of PHOS. The columns from above to bottom show the HG, LG, cell energy after the raw event reconstruction and the cluster energy.

4.5 Track segment reconstruction

For photons, there are no nominal ”tracks” in the central tracking system. The track segment here means the track position matching between TPC to EMC or CPV (not installed yet) to EMC, in order to exclude the charged particle contamination to the photon measurement. The basic idea is to propagate the tracks from TPC to PHOS surface and use the distance between the PHOS cluster and the propagated point as a complementary method for the charged particles identification. The matching performance between the TPC and PHOS with a realistic detector configuration has been studied with simulations. The track matching efficiency reaches 80% for low charged particle density dN/dη=400 and 70% for dN/dη=4000 with a weak dependence on the particle transverse momentum. The detailed simulation study on the track matching from TPC to PHOS can be found in [139].

4.6 Photon identification

Particle identification for the EM-calorimeters is based on:

1) Time of flight information to reject the slow and heavy hadrons;

2) Shower Shape Analysis (SSA) to distinguish the electromagnetic and hadronic showers;

3) The TPC-EMC position matching to discriminate the charged hadrons.

Combing the above information on a statistical basis, the PID probability and purity was defined and studied in simulation, which can be found in [140].

As a complement, the Bayesian method has been developed. It assigns a PID weight (or probability) to every reconstructed particle on an event-by-event basis. PID weight is calculated as:

$$W(i) = \frac{P(tof|i) \cdot P(d^{xz}_{TE}|i) \cdot P(dis|i) \cdot P(rec|i)}{\sum_s [P(tof|s) \cdot P(d^{xz}_{TE}|s) \cdot P(dis|s) \cdot P(rec|s)]}, \tag{4.14}$$

where P is the density probability distribution for a given particle i and $s = \gamma, e^{\pm}, h^0, h^{\pm}$ and π^0. The PID probability of the different detectors can also be combined onto a global PID probability with ALICE central tracking detectors. The simulations indicate that, at low and intermediate p_T, PHOS PID efficiency is close to 100% for photons and electrons in a low-multiplicity environment, and about 80% to 90% in heavy-ion collisions. For the high-transverse-momentum π^0 ($p_T > 30\ GeV/c$), the two decay photon clusters start to merge and can be misidentified as a single cluster. The Bayesian method is able to provide a good separation and obtains a π^0 PID efficiency up to 80% with a misidentification probability below 10% [141]. This is particularly interesting to maximize the high-p_T π^0 yield and minimize the

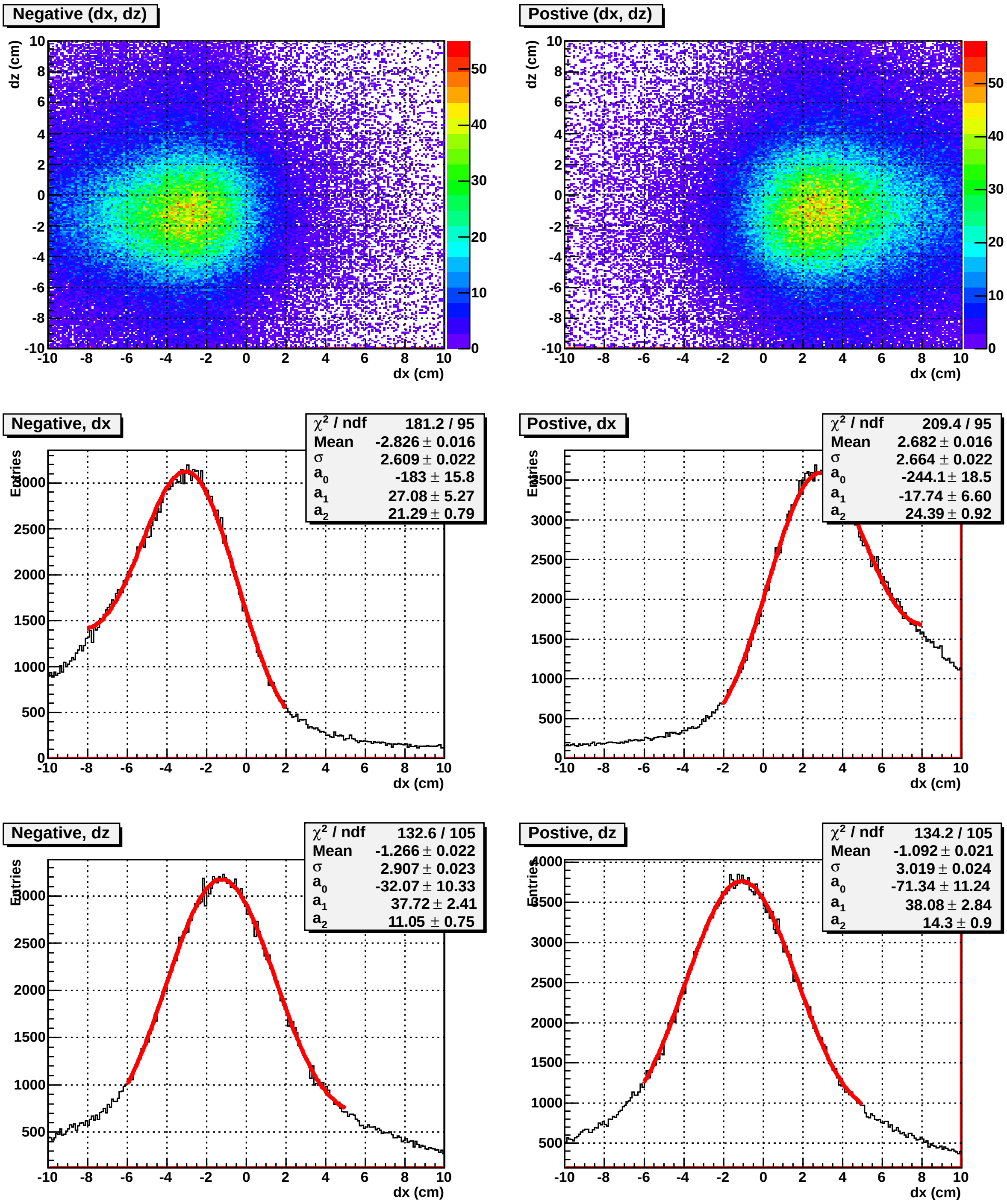

Figure 4.9: The track matching performance with ALICE PHOS in pp at 7 TeV data. There is no PID for the charged particles but from all the charged hadron contributions.

systematical uncertainties for direct photon measurements. This method still needs to be further studied with the real data.

At the moment, timing information is not provided available yet which needs to be further tuned and calibrated. Thus only the track matching and the shower shape analysis are studied in the analysis.

4.6.1 Track-position matching from TPC to EM-calorimeters

The standard track cuts are used for the track selection. And the cluster p_T value is larger than 300 MeV/c. Fig. 4.9 shows the track matching performance with ALICE PHOS in pp collisions at 7 TeV data. No charged particles PID by central tracking system is used, but from all the charged hadron contribution. For the positive and negative particles, a position shift $\sim 3cm$ in x direction due to the ALICE magnetic field, and ~ 1 cm shift in z direction are observed.

4.6.2 Shower shape in real data

In the real data analysis, we first select the photon whose combined with another cluster in one event has an invariant mass in the nominal π^0 mass window. However, there are still lots of combinatorial background from uncorrelated cluster pairs (some of them are caused by the charged hadrons). As shown in Fig. 4.10, at higher $p_T >$ 2 GeV/c, it presents a similar behavior as in simulation with the single photon event. At lower $p_T < 2$ GeV/c, the charged hadrons contamination may disturb the idea photon shower topology.

Here I just present some performance plots on the photon identification. However, particle identification is not used in order to keep a high statistics for the neutral mesons measurement. It is then necessary for the photon analysis, where we need to know exactly whether the cluster is a photon or not.

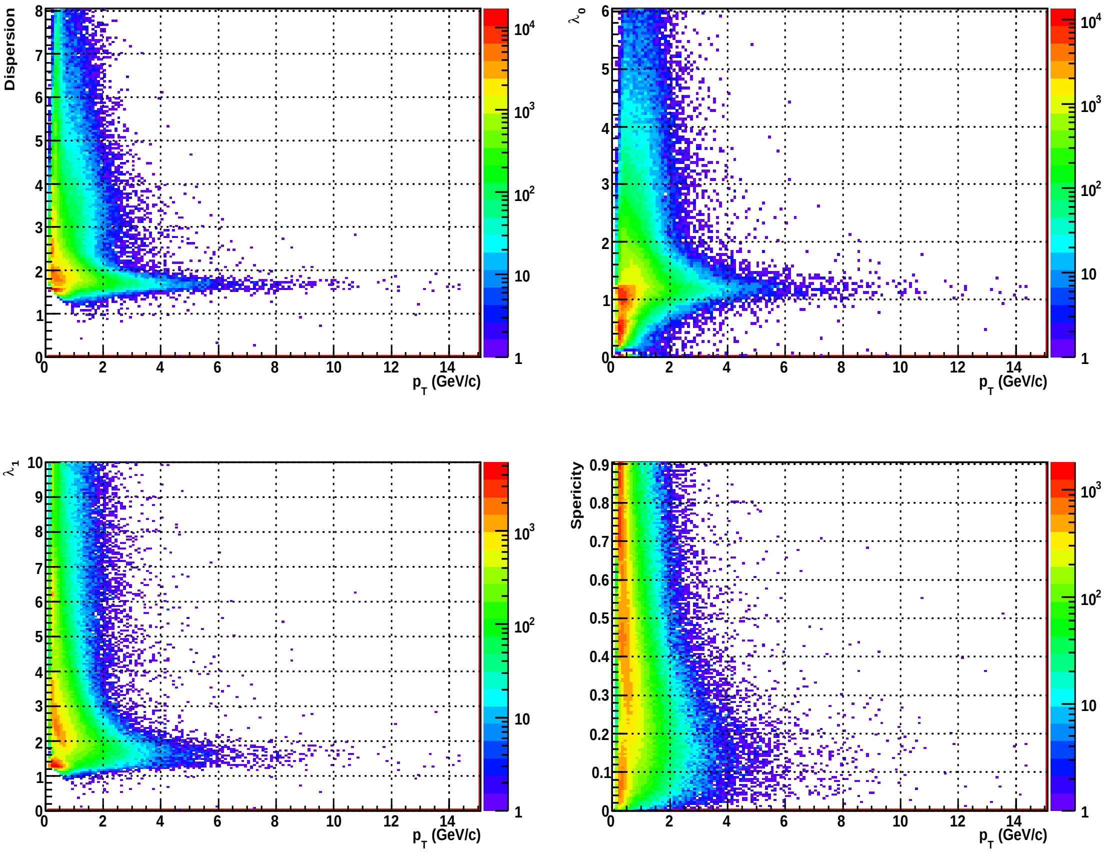

Figure 4.10: The shower shape parameter performances obtained from data with pp collisions at 7 TeV with PHOS. No particle identification is used. Instead, the photon combined another photon within an event has an invariant mass in the π^0 mass window selected.

Chapter 5

Raw yield of neutral mesons

This chapter presents the analysis of proton-proton collisions data at 7 TeV. About 390 million events used after the standard physics selection and data quality check. Then we optimize the cluster and cluster-pair selection. The raw yield of neutral mesons are extracted by using invariant mass analysis.

5.1 Event selection and QA

The trigger detectors V0 and SPD are used to select the min-bias events. It accepts events which have at least one hit in SPD, or in either one of the V0 beam counters. To subtract the min-bias events background, such as from beam-gas or pileup events, the offline analysis follows the official physics selection (AliPhysicsSelection in AliRoot) [144] by ALICE analyzers. Besides, for calorimeters, we also require the collision vertex in Z coordinate should less than 10 cm, and at least one primary track reconstructed in central tracking detectors by using the standard ITS+TPC track cuts.

At the event level of calorimeters, the cluster with a energy > 300 MeV/c and digit multiplicity > 2 for PHOS and > 1 for EMCAL is selected as a photon candidate for neutral mesons reconstruction. Besides, a group of criteria based on the average characterization in a event is defined for the data quality assessment:

1) The average value of the number of cluster and cluster energy;

2) The slope of the cluster p_T distribution;

3) The invariant mass peak position and quantity of the reconstructed π^0 with the photon pair at $p_T > 1$ GeV/c;

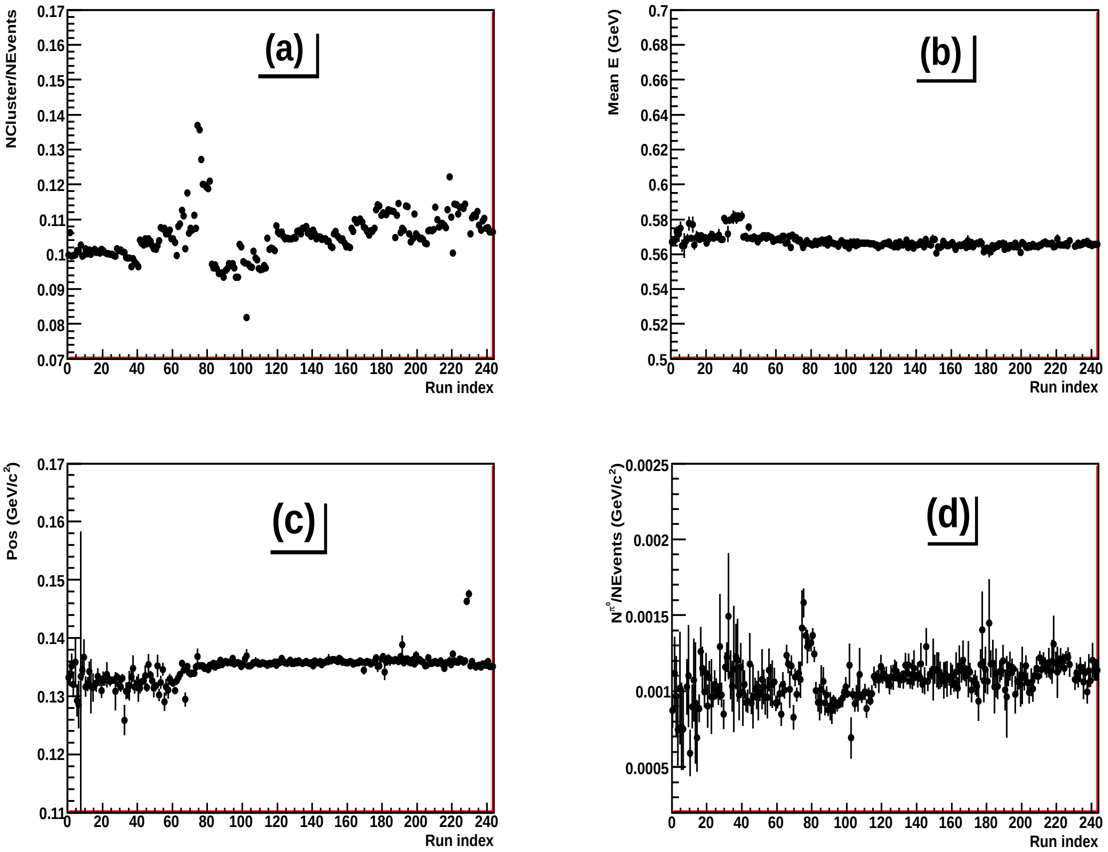

Figure 5.1: PHOS QA plots. (a) The averaged number of cluster per event. (b) The mean energy deposition per event. (c) The invariant mass peak position around the π^0. (d) The number of reconstructed π^0 per event.

Fig. 5.1 shows the PHOS QA plots for the runs at a level of ESD analysis. The run indexes correspond to the runs listed in Table: 5.1. From the QA results, the averaged number of clusters per event is about 0.11. The mean energy deposition per run is about 0.56 GeV. The 2γ invariant mass position for π^0 sits at 135 MeV/c^2. While the averaged number of π^0 is about 0.001 (for the photons pairs with $p_T > 1\ GeV/c$). In principle, all the good runs should have similar global properties after being normalized to the triggered events. Any runs with a QA value larger than a 3 standard deviation from the mean value is considered as a bad run. We can observe that a large variation with the run index of 65 to 75, 231 and 232. After checking these run conditions and detailed, it was found that there are some additional hot channels not properly marked. In this analysis, these runs are marked as bad. The detailed analysis with QA can be found in [145].

5.2 Data sample

After the physics selection and the event quality check, 244 runs in total[1] were converted from ESD to AOD for the physics analysis. These runs are from different periods and passes of reconstruction:

- Pass2 reconstruction of LHC10b (115393 – 117222) + LHC10c (119041 – 120829) + LHC10d (125628 – 126437);
- Pass 1 reconstruction of LHC10e (127719 – 130848).

13 runs in the table marked as black-bold font are bad runs for PHOS. The runs are listed in the below table:

Table 5.1: The runs used in the analysis from proton-proton collisions at 7 TeV. 13 runs marked as black-bold font are bad runs for PHOS. In total, 244 runs with 391 million for EMCAL and 231 runs with 366 million min-bias events are used.

Index	Run	NEvents	Index	Run	NEvents	Index	Run	NEvents
1	115393	761741	83	125628	3194043	165	128678	372913
2	115401	841735	84	125630	2098283	166	128777	1296627
3	115414	322574	85	125842	1591583	167	128819	420695
4	115521	110874	86	125843	417245	168	128820	934897
5	116102	148850	87	125844	176595	169	128823	380536
6	116401	62556	88	125847	673243	170	128824	1723295
7	116402	113643	89	125848	732600	171	128833	1248644
8	116403	111666	90	125849	1952700	172	128835	129247
9	116561	26875	91	125855	2753948	173	128836	1463302
10	116562	436557	92	126004	620222	174	128843	983985
11	116571	206616	93	126008	875922	175	128850	3216293
12	116572	111943	94	126073	2711954	176	128853	964583
13	116574	595401	95	126078	5740054	177	128855	1134885
14	116643	85792	96	126081	1872025	178	128913	527760
15	116645	157882	97	126082	3354606	179	129514	662229
16	116684	99237	98	126088	4411723	180	129515	127761
17	117048	1355541	99	126090	4355008	181	129516	253595
18	117052	656783	100	126097	1512212	182	129519	354273
19	117053	918265	101	126168	2199460	183	129520	1009226
20	117054	1110053	102	126283	1453599	184	129521	94040
21	117059	731254	103	126284	7769073	185	129523	917082
22	117063	758542	104	126285	282348	186	129524	272422

---

[1] Actually, there are a bit more runs than this amount. However, due to the grid analysis, this number is the best I was able to achieve.

23	117065	1095632	105	126350	242463	187	129525	208755
24	117077	192882	106	126351	3957537	188	129527	291525
25	117099	2345848	107	126352	2068073	189	129528	725189
26	117109	1341298	108	126359	1259561	190	129536	1441280
27	117112	2663785	109	126403	481883	191	129540	1697905
28	117116	2328497	110	126405	284021	192	129587	670928
29	117118	98488	111	126406	3646289	193	129599	349911
30	117220	1440481	112	126407	5073890	194	129639	110180
31	117222	963041	113	126408	2157439	195	129641	1232754
32	119041	1447168	114	126409	1622429	196	129652	722184
33	119047	1502334	115	126422	4313024	197	129653	839990
34	119055	62385	116	126424	6506629	198	129654	6248905
35	119057	307540	117	126437	1712934	199	129659	389322
36	119061	477510	118	127719	1645408	200	129666	838425
37	119067	93953	119	127724	2305120	201	129667	1873676
38	119077	248662	120	127729	3967548	202	129723	254856
39	119079	185150	121	127730	875799	203	129725	242985
40	119084	339583	122	127814	980602	204	129729	1057866
41	119085	451229	123	127815	2826023	205	129735	1458636
42	119086	184878	124	127817	3127543	206	129736	1532338
43	119159	1479498	125	127822	1207582	207	129738	1011731
44	119161	3024199	126	127931	3401383	208	129742	719975
45	119163	1725186	127	127932	1568352	209	129960	843118
46	119841	348120	128	127933	1076440	210	129961	4187787
47	119842	2166194	129	127935	956627	211	129962	1288075
48	119844	289860	130	127936	1370012	212	129966	2977508
49	119845	1939259	131	127937	1488332	213	129983	3850599
50	119856	1251511	132	127941	1644046	214	130149	2135861
51	119859	340137	133	127942	2463724	215	130151	1762578
52	119862	4153011	134	128175	4717878	216	130157	2374116
53	119904	259470	135	128180	1801974	217	130158	2280859
54	119907	1095717	136	128182	1141180	218	130172	880365
55	119909	854071	137	128185	1086700	219	130178	2383399
56	119913	452431	138	128186	1375233	220	130179	313888
57	119917	922989	139	128189	2721971	221	130342	289270
58	119935	683235	140	128191	832283	222	130343	1285356
59	119952	686525	141	128192	454904	223	130479	208072
60	119959	1555164	142	128257	7234035	224	130480	2016891
61	119961	4779597	143	128260	1097589	225	130481	1399165
62	119965	5912794	144	128452	4523049	226	130517	5326641
63	119969	3868256	145	128483	502703	227	130519	3477048
64	119971	1932359	146	128486	1986031	228	130520	4023656
65	**120069**	**1479662**	147	128494	784249	229	130524	2215645

66	**120072**	**2977857**	148	128495	409702	230	130526	1168235
67	**120073**	**1862333**	149	128498	1684131	**231**	**130601**	**1637896**
68	**120076**	**2303418**	150	128503	3752276	**232**	**130608**	**548231**
69	**120079**	**1047918**	151	128504	3478120	233	130628	1586663
70	**120244**	**1892037**	152	128505	144091	234	130696	1542997
71	**120503**	**1262601**	153	128506	838244	235	130704	2330445
72	**120504**	**3127427**	154	128507	556083	236	130793	1698808
73	**120505**	**4334432**	155	128582	510528	237	130795	9287709
74	**120617**	**1820193**	156	128590	885240	238	130798	367390
75	**120671**	**711050**	157	128592	1921012	239	130799	1391058
76	120820	120936	158	128594	364293	240	130834	1029955
77	120821	1111144	159	128596	974113	241	130840	540193
78	120822	3117727	160	128605	479565	242	130844	4126221
79	120823	816964	161	128609	3894799	243	130847	595246
80	120824	3900741	162	128611	590174	244	130848	1596815
81	120825	2660570	163	128615	998465			
82	120829	3692774	164	128621	1769553			

5.3 Cluster selection

To study the detector performance, as well as to understand their influence on the photon spectra, the following cuts are considered for the physics analysis.

- Energy of cluster. The hadron deposits its energy through the ionization loss process corresponding to a minimal energy 230 MeV in calorimeters. Also there are fractional cluster energies from electronic noise. Here we set the cuts $> 0.1,\ 0.3,\ 0.5,\ 0.7\ and\ 1\ GeV/c$ to estimate the influence on π^0 spectra. In the final analysis, the energy of cluster which is larger than 300 MeV/c are selected to suppress the hadronic background.

- Cell multiplicity of the cluster. It is firstly used to suppress the background by minimum ionizing particles and hadron. In addition, the high energy charged hadrons deposit small part of their energy in calorimeters but with a larger spread. Finally, there are occasional clusters with a small number of cell multiplicity but with a large energy, which may be caused by the punch-through effect or un-physics source.

  The cluster p_T distribution for different cell multiplicity value are shown in Fig. 5.2(a) for PHOS and in Fig. 5.2(b) for EMCAL. The higher cell multiplicity cut, the stronger suppression at lower p_T, $< 0.8\ GeV/c$ for PHOS and $< 3\ GeV/c$ for EMCAL. While for the high p_T clusters, there is no obvious dependence on the cell multiplicity.

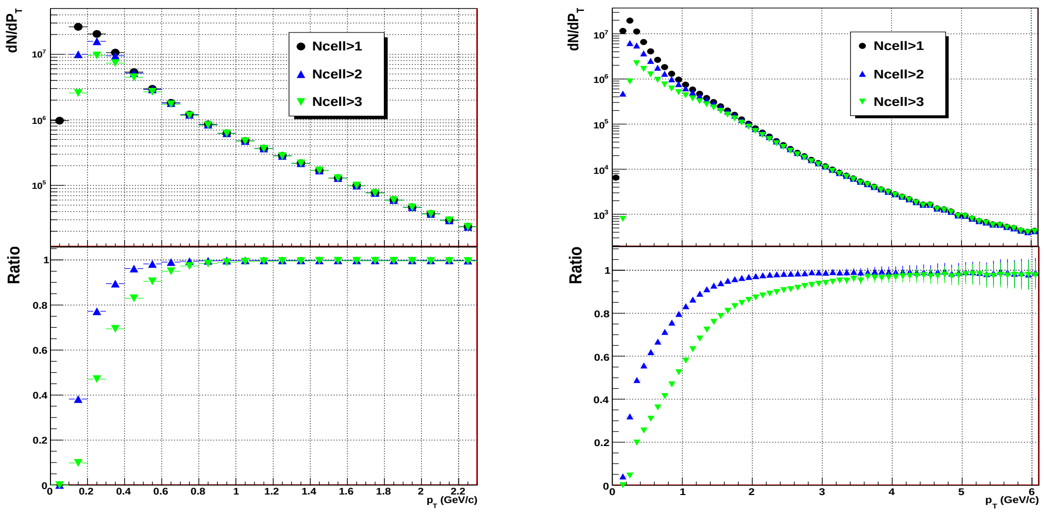

(a) PHOS

(b) EMCAL

Figure 5.2: p_T distributions of clusters for three number of cell cuts in PHOS (a) and EMCAL (b).

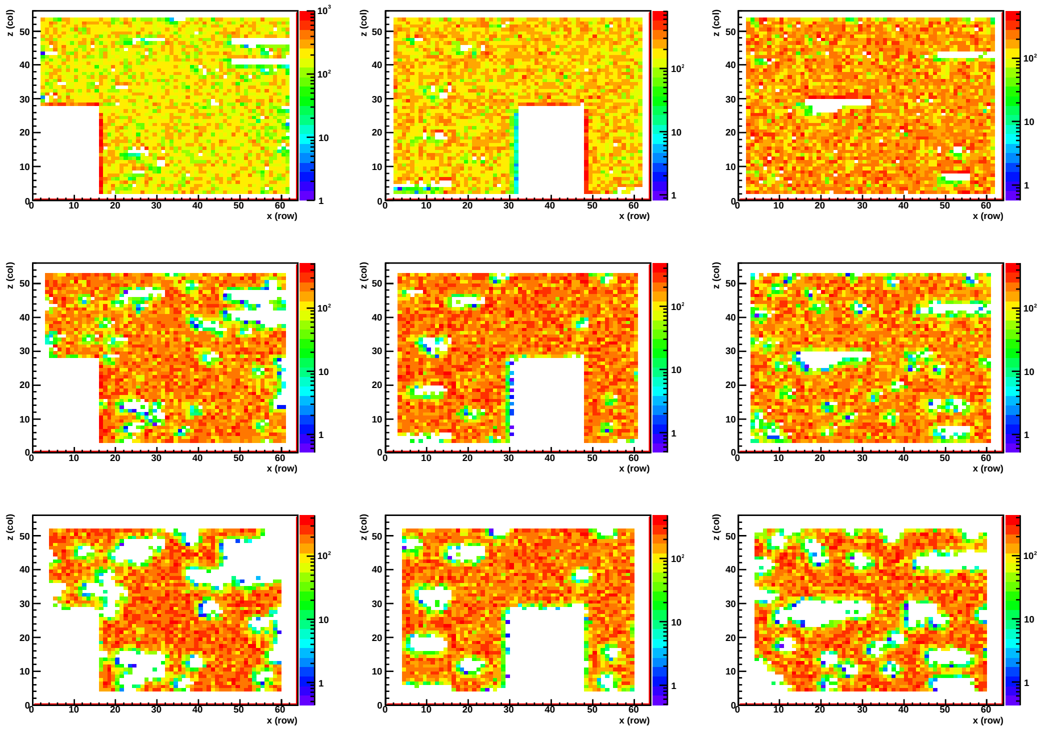

Figure 5.3: The cluster distribution in PHOS (x, z) plane after the rejection of the cluster with distance to bad channels cuts. 1, 2 and 3 cell-size correspond to 2.2, 4.4 and 6.6 *cm* distances respectively. The cells in edge are assumed as bad channels.

- Distance to bad channels. The energy of incident particle (γ) will be partly lost or changed in case there are some bad channels among the fired channels. By using the distance to bad channel cuts will remove this contribution to keep the integral information of the photon cluster. Fig. 5.3 and Fig. 5.4 show the cluster distribution in the detector transverse plane, respectively for PHOS and EMCAL after the rejection of the cluster whose distance to the closest bad channels is smaller than 1, 2, 3 cell-size (corresponding 2.2, 4.4 and 6.6 *cm* for PHOS and 6, 12 and 18 *cm* for EMCAL). The cluster p_T distributions by using the distance to bad channels cuts are shown in Fig. 5.5(a) for PHOS and Fig. 5.5(b) for EMCAL. About 20%∼30% clusters will be lost by using 2 and 3 cell-size cuts.

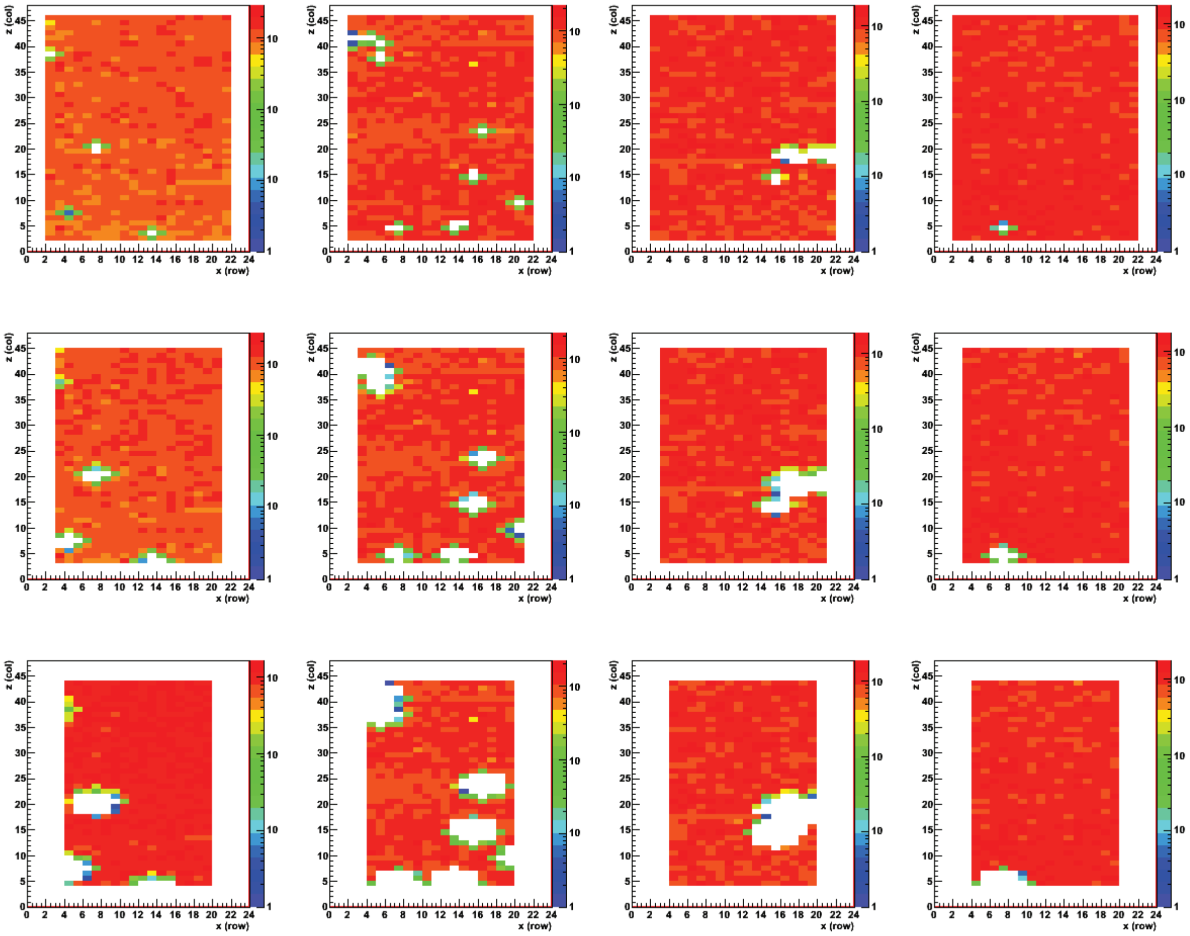

Figure 5.4: Cluster distributions in EMCAL (x, z) plane after the rejection of the cluster with distance to bad channels cuts. The 1, 2 and 3 cell-size correspond to 6, 12 and 18 *cm* distance, respectively. The towers in edge are assumed as bad channels.

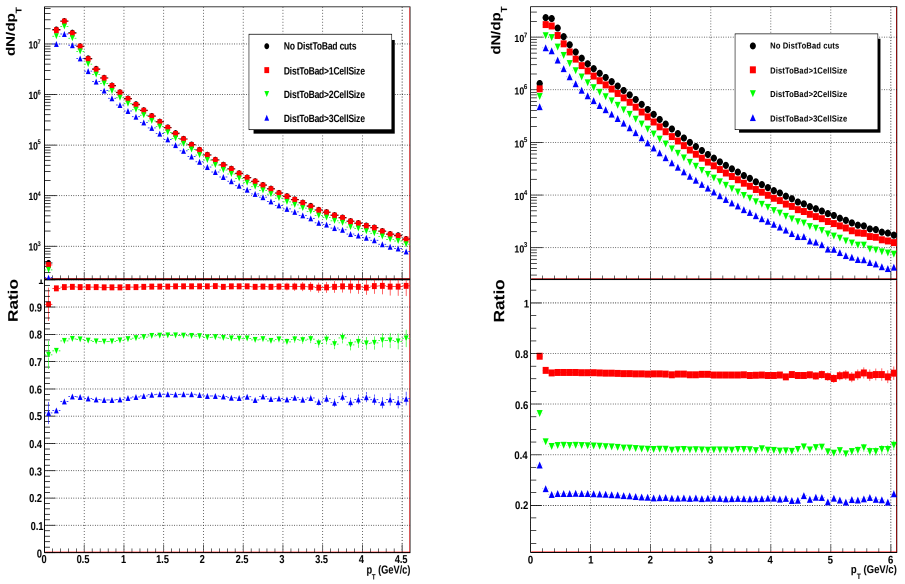

(a) PHOS (b) EMCAL

Figure 5.5: p_T distribution of clusters under different distances to bad channel cuts for PHOS (a) and EMCAL (b). The cell-sizes corresponding to 2.2, 4.4 and 6.6 cm distance to bad channels for PHOS and 6, 12 and 18 cm for EMCAL.

- Particle identification. The particle identification is critical for the photon selection and the photon physics analysis where we should unambiguously know the particle ID. However, for the neutral meson measurements, there is no effect on the extraction of the resonance peak, and thus we will not use it here.

5.4 π^0 raw yield extraction

We first construct the 2 dimensional histogram ($m_{2\gamma}$, p_T), and then extract the number of π^0 in each p_T bin. Due to some correlated background originating from the photon conversion, or some other physics processes such as the jet fragmentation, flow effect and HBT correlations, there are some combinatorial background around the π^0 peak at low p_T. By using the photon identification, the correlated background around π^0 peak will be reduced. However, the statistics decrease by more than a factor 4. A compromise way is to extract the signal by different fitting functions or methods and take the contribution into account as the systematic uncertainties.

Mathematical fits of the real invariant mass distribution

We first use the mathematical fit to extract the raw yield by using the real invariant mass distribution. The procedure to extract the raw yield has been described in chapter 3. Fig. 5.6 to Fig. 5.9 show the invariant mass distribution at 24 p_T bins from

0.6 GeV/c to 25 GeV/c. The distributions are fitted by at Gaussian plus a second order polynomial function. At $p_T < 2$ GeV/c, the background can not be fitted well by the second order polynomial function, and should be considered separately to use higher order polynomial function.

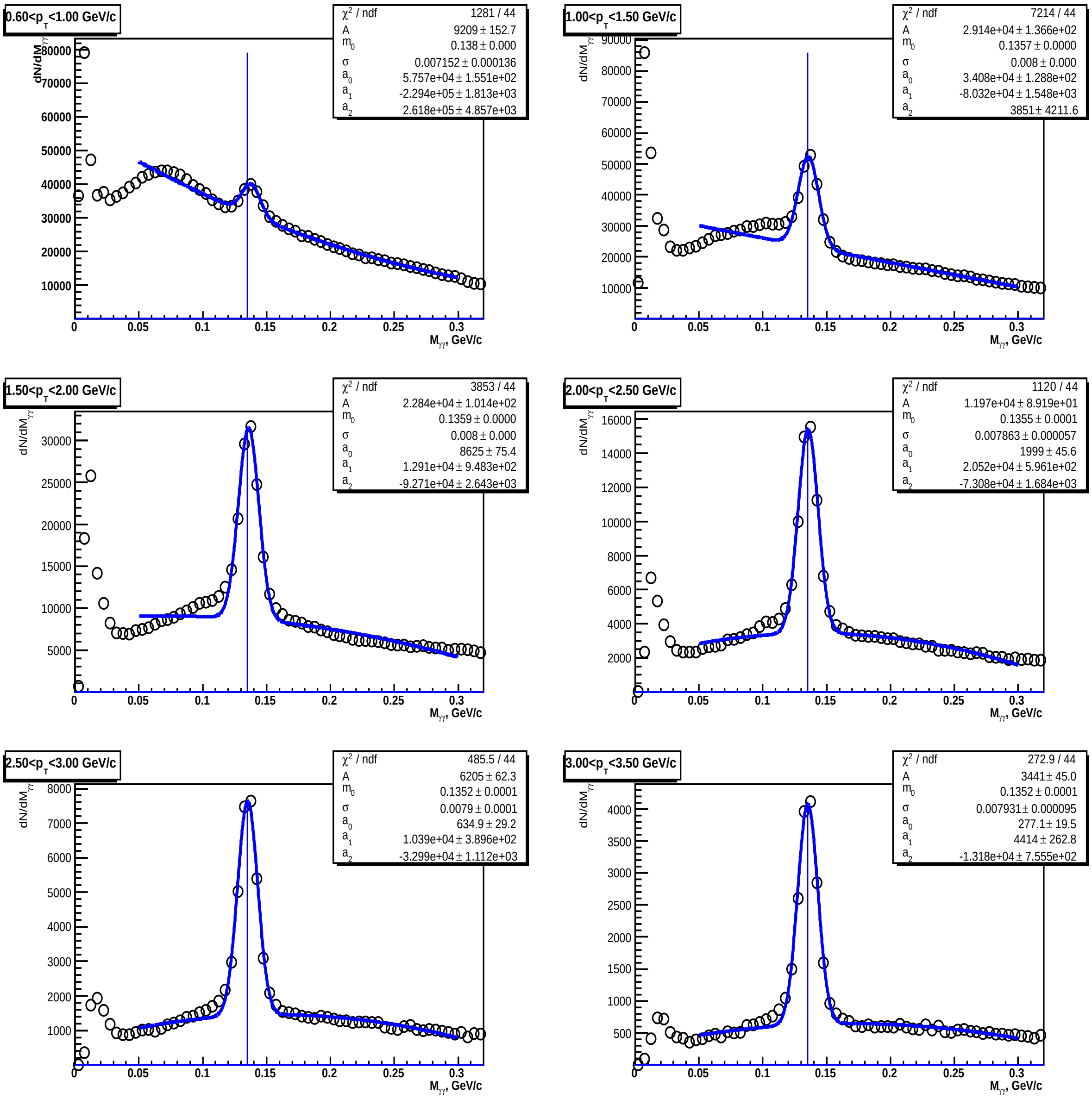

Figure 5.6: PHOS, in pp collisions at 7 TeV: Invariant mass spectra at $0.6 < p_T < 3.5$ GeV/c. The histograms are fitted by Gaussian and polynomial functions.

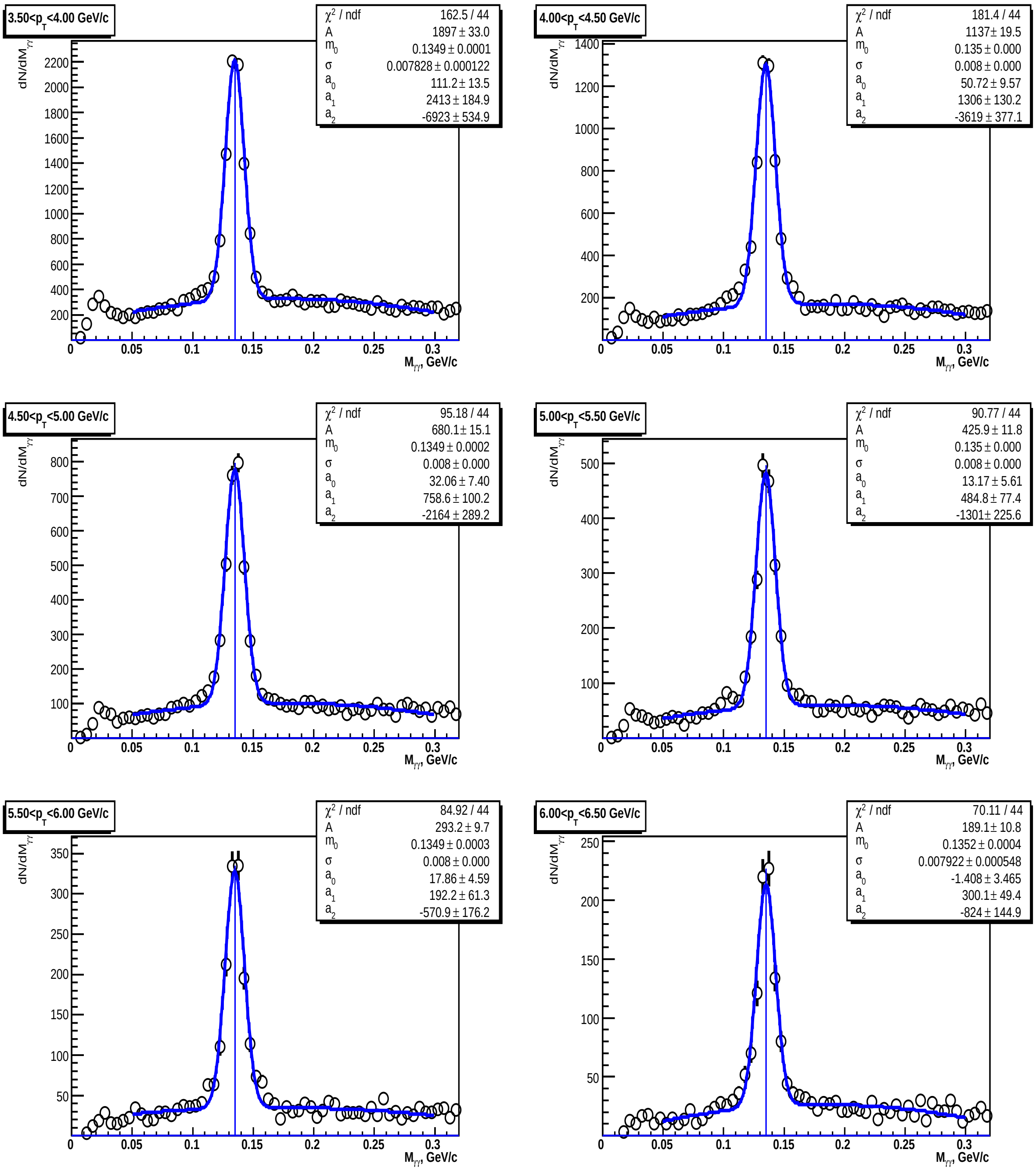

Figure 5.7: PHOS, in pp collisions at 7 TeV: Invariant mass spectra at $3.5 < p_T < 6.5$ GeV/c. The histograms are fitted by Gaussian and polynomial functions.

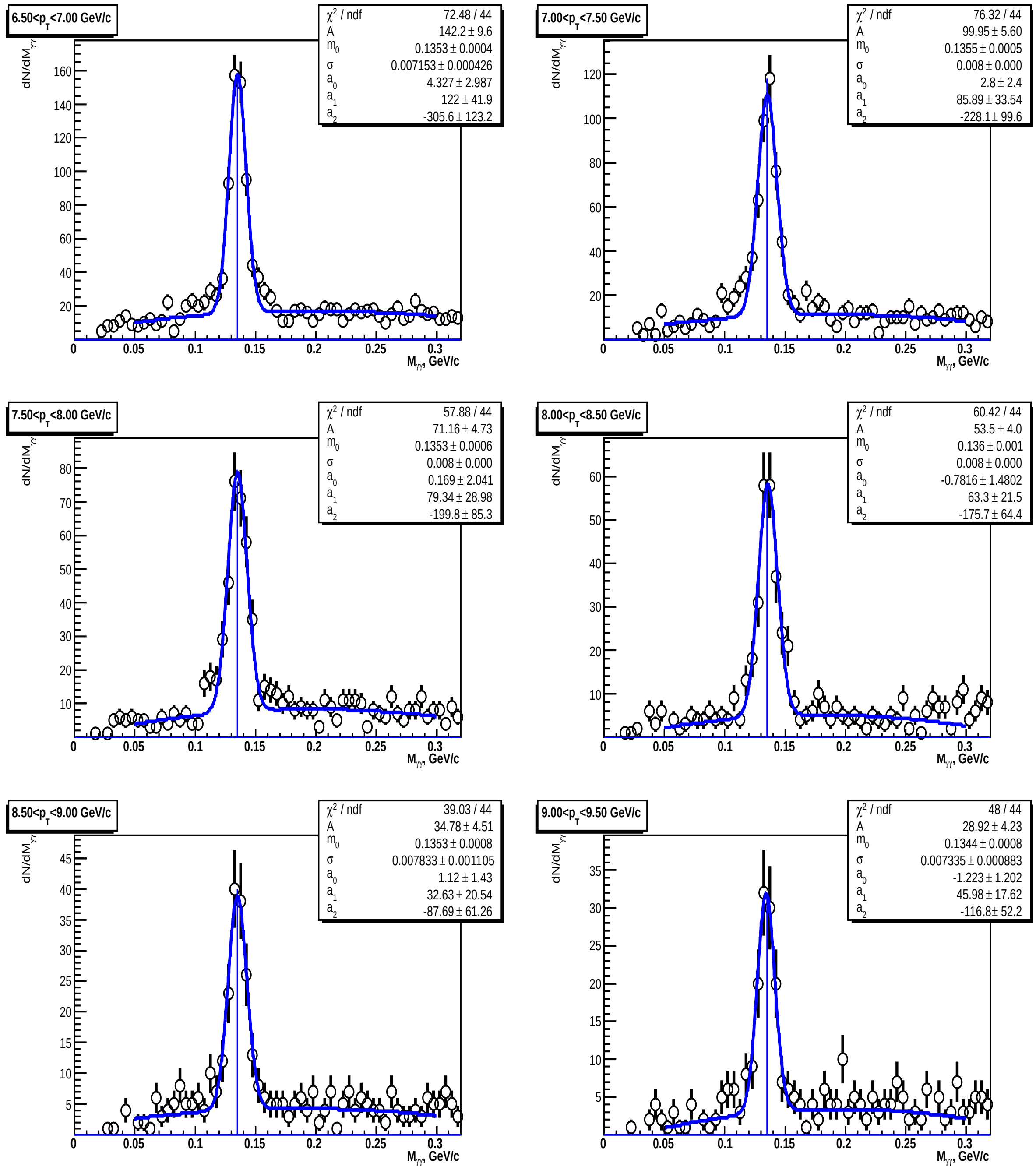

Figure 5.8: PHOS, in pp collisions at 7 TeV: Invariant mass spectra at $6.5 < p_T < 9.5$ GeV/c. The histograms are fitted by Gaussian and polynomial functions.

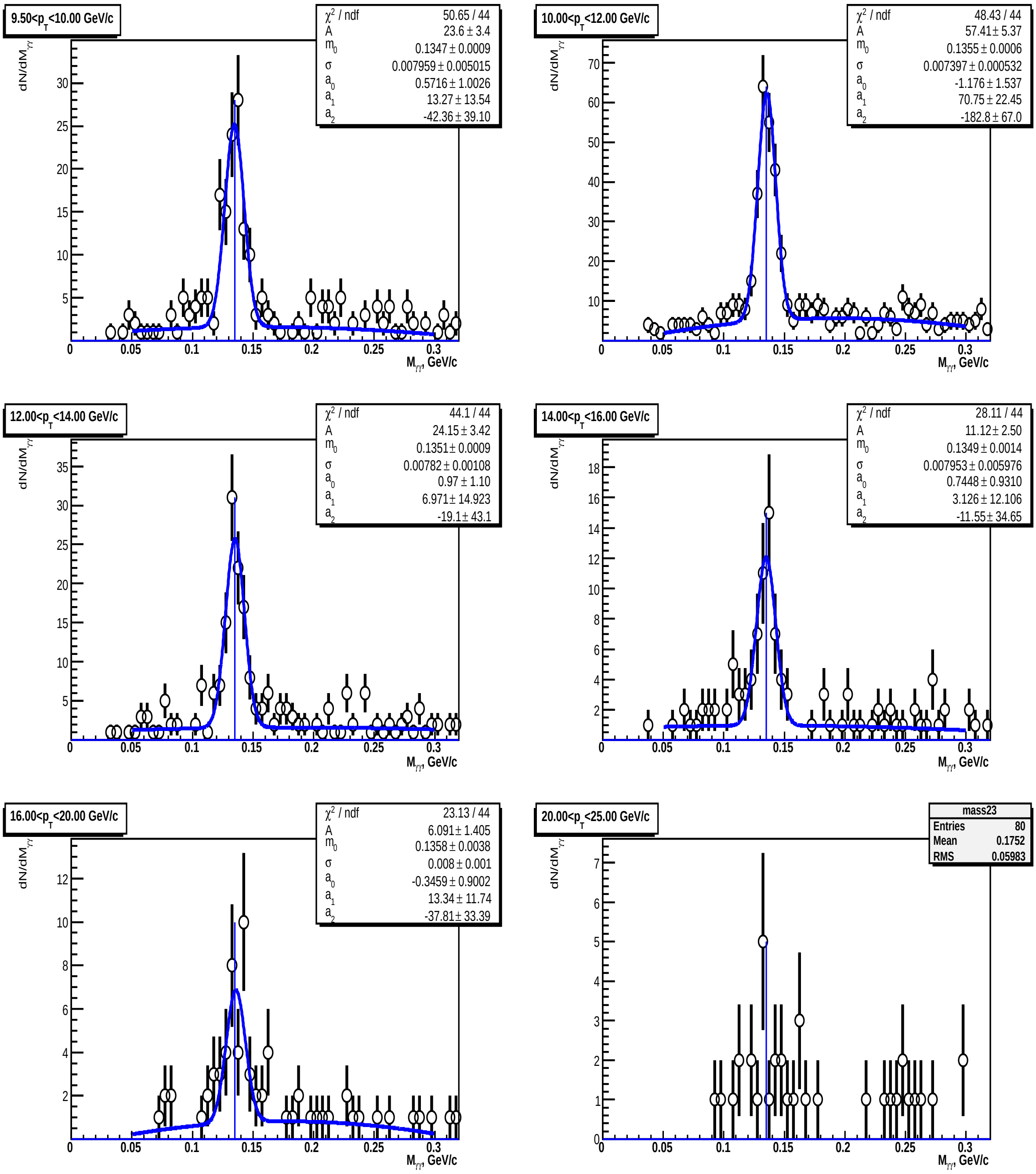

Figure 5.9: PHOS, in pp collisions at 7 TeV: Invariant mass spectra at $9.5 < p_T < 25.0\ GeV/c$. The histograms are fitted by Gaussian and polynomial functions.

π^0 raw yield influenced by the cut selection

Here the influences of using the different cuts for the photon and photon pairs selection on the π^0 raw yield are studied.

Fig. 5.10 shows the p_T dependence on the π^0 extraction. The clusters with p_T larger than 0.1, 0.3, 0.5, 0.7 and 1 GeV/c are selected for the reconstruction of invariant mass distribution. There are no obvious influence to the π^0 peak position and resolution. The peak positions stay around 135 ± 1 MeV/c^2 and the resolution is 7.6 ± 0.8 MeV/c^2. At larger p_T, the signal-to-background is slightly improved and the raw yield at lower p_T is decreased.

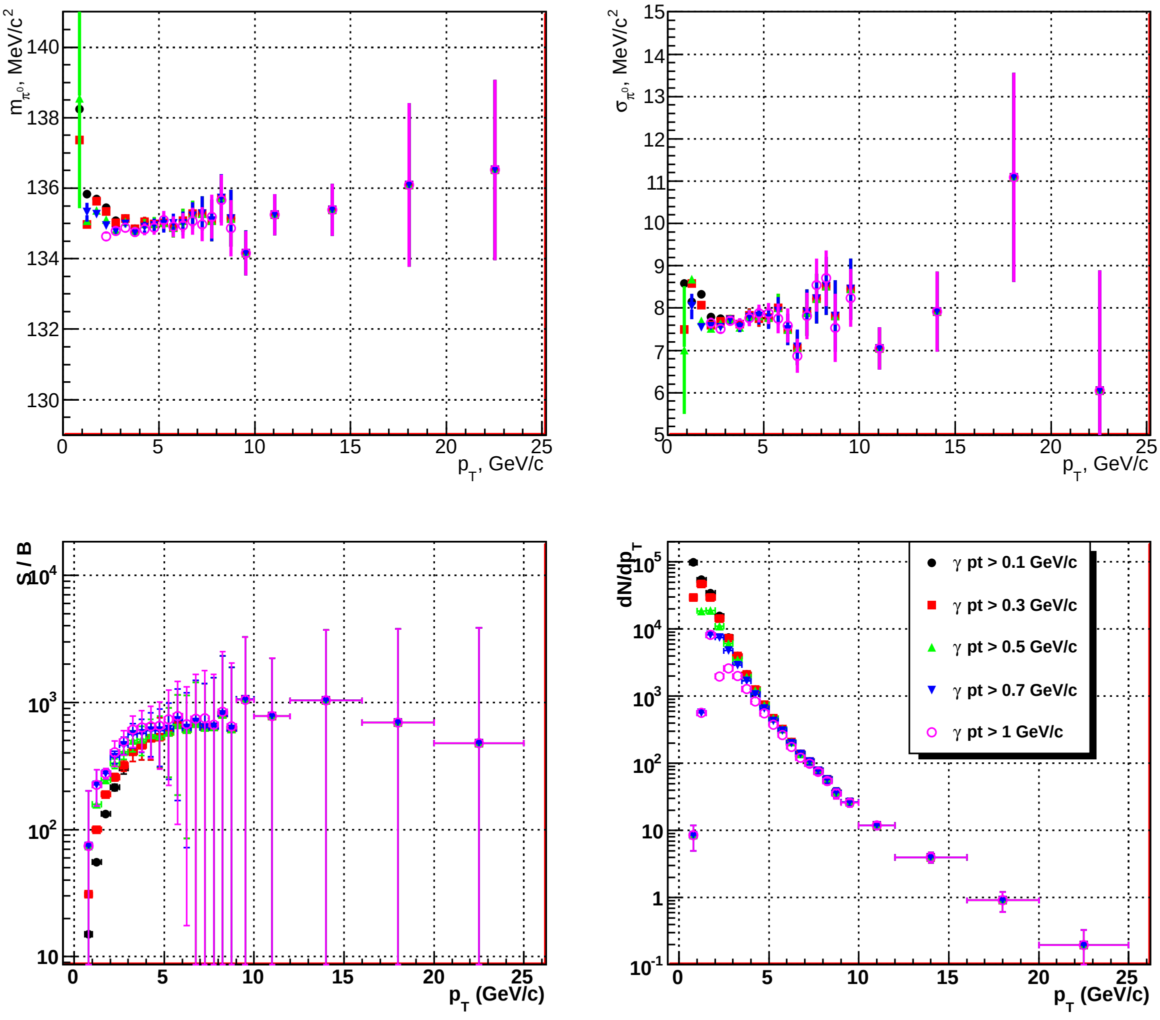

Figure 5.10: Performance of π^0 peak position, resolution, signal-to-background and raw yield with different p_T cuts of cluster measured in PHOS for pp collisions at 7 TeV.

Fig. 5.11 shows the π_0 performance depending on the cell multiplicity of the cluster. The photons with at least 1, 2 and 3 cell multiplicities are selected to extract the invariant mass. With tight cuts, the clusters at lower p_T are rejected and also the number of reconstructed π^0. However, there are no obvious improvement to the π^0 peak position and resolution. The signal-to-background is slightly improved. In the later analysis, we choose a moderate cut $N_{cell} > 2$ for PHOS analysis.

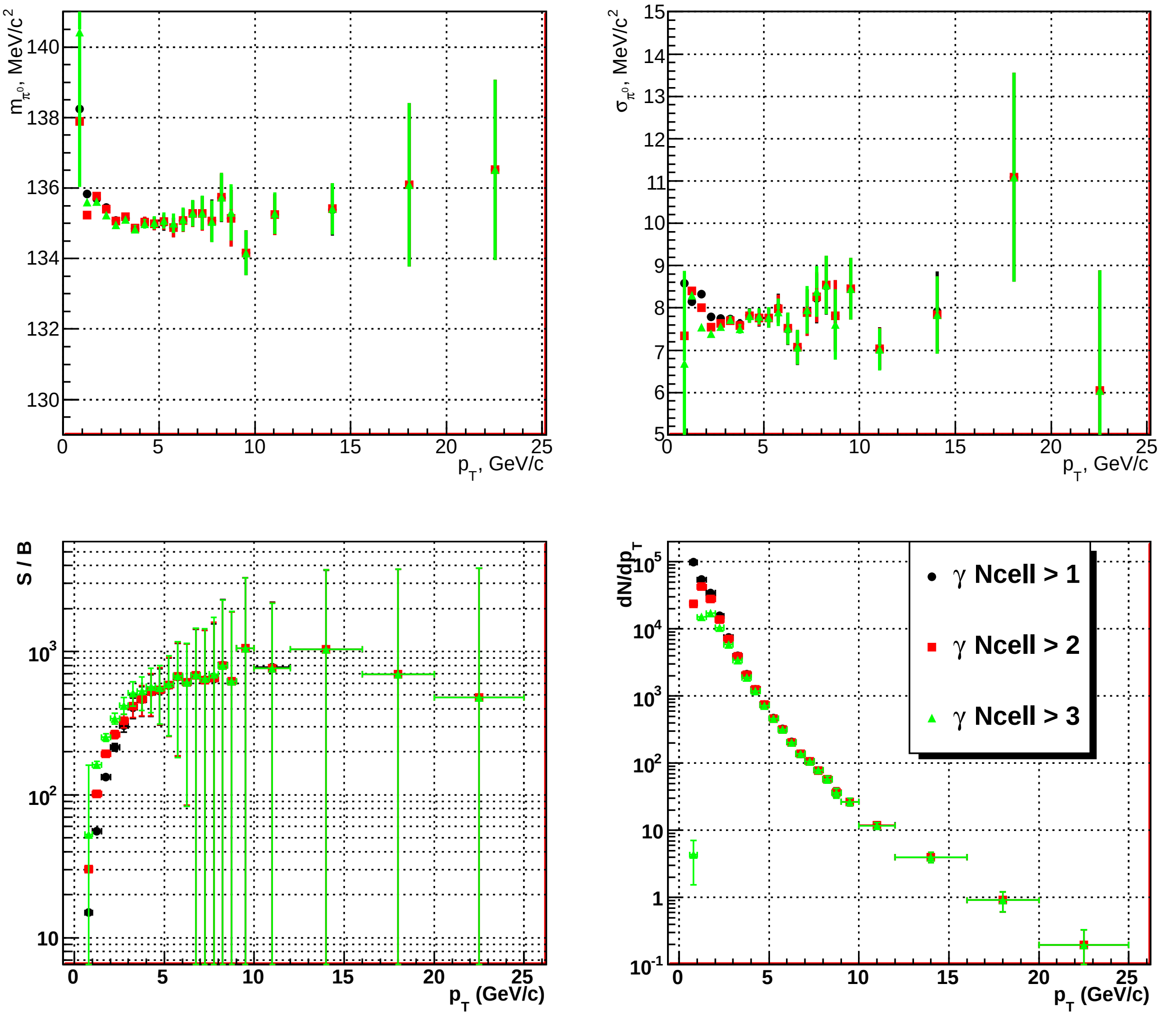

Figure 5.11: Performance of π^0 peak position, resolution, signal-to-background and raw yield with different number of cell cuts of cluster measured in PHOS for pp collisions at 7 TeV.

The spectra are shown in Fig. 5.12 with different clusters energy asymmetry cuts < 0.5, 0.6, 0.7, 0.8 and 1. There is no improvement to the π^0 mass resolution. With the strict cuts, it improves the signal-to-background with a factor 2 to 4, while the raw yield are suppressed at higher p_T.

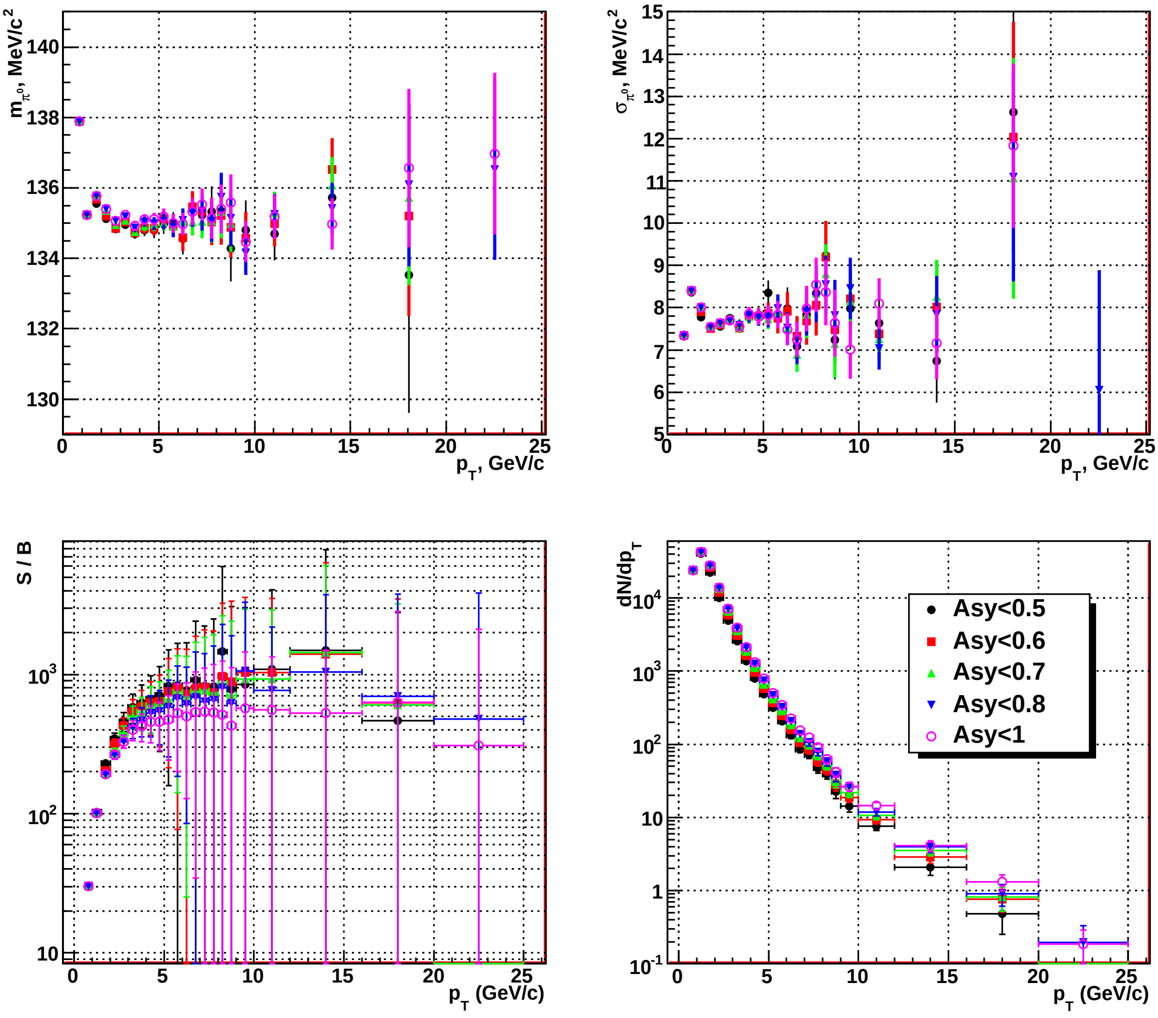

Figure 5.12: Performance of π^0 peak position, resolution, signal-to-background and raw yield with different energy asymmetry cuts of cluster pairs measured in PHOS with pp collisions 7 TeV.

Fig. 5.13 presents the π^0 performance by using the distance to bad channel cuts. Using the 2 or 3 cell-size cut do not change the π^0 mass position, but the mass resolution is slightly improved from 8 MeV/c^2 to 7 MeV/c^2. The signal-to-background increase by a factor 1∼2 factor by using a tight cut. However, it suppresses the raw yield by about a 2 factor in the whole p_T range with the 2 or 3 cell-size cut.

To keep a high statistics and a reasonable level of signal to background, for PHOS, the loose cuts of $p_T > 0.3$ GeV/c, number of cells per cluster larger than 2, distance to bad channel larger than 1 cell-size and the clusters pair energy asymmetry smaller than 0.8 are used for the following analysis.

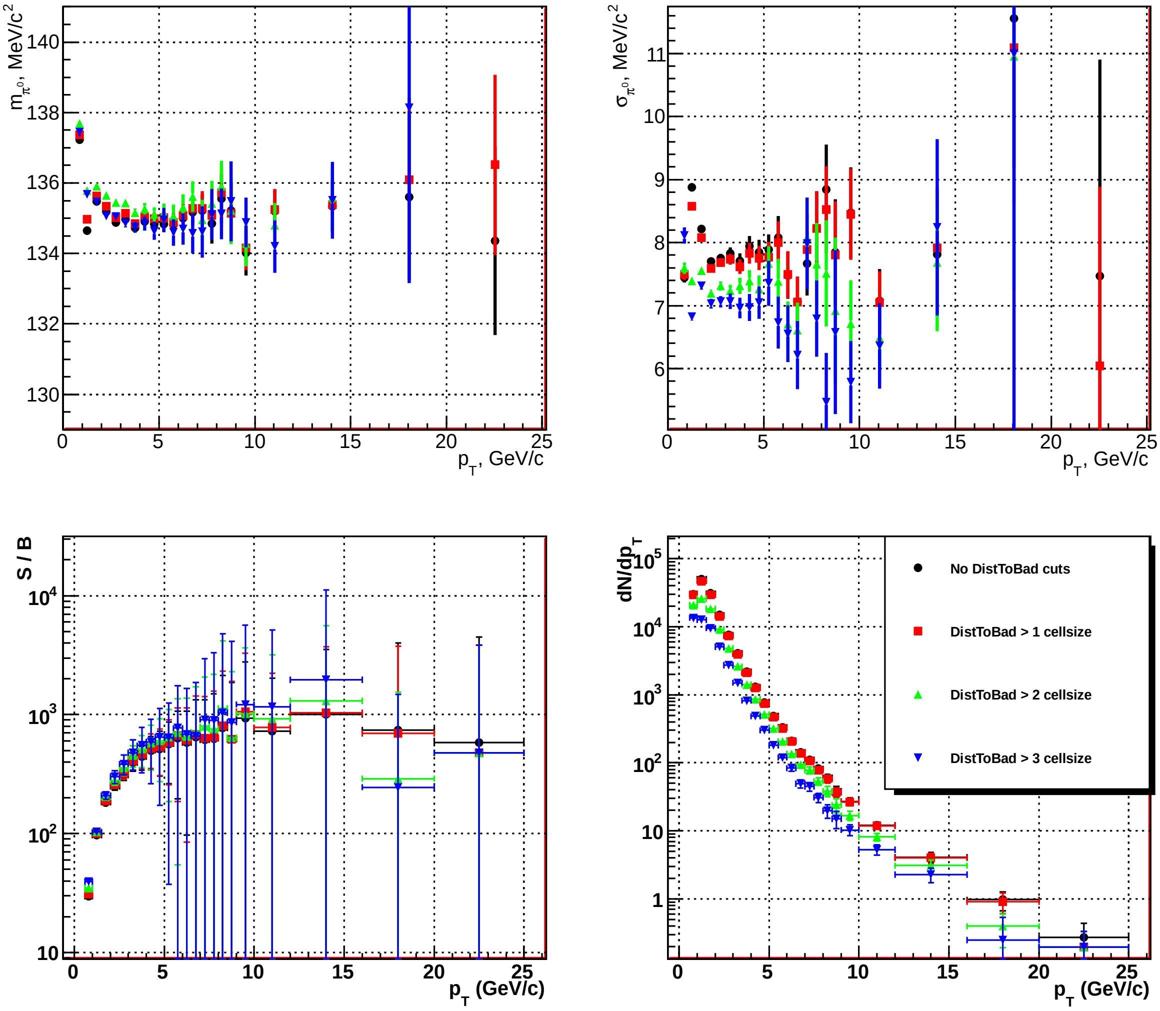

Figure 5.13: Performance of π^0 peak position, resolution, signal-to-background and raw yield with different distance to bad channel cuts of cluster measured in PHOS for pp collisions at 7 TeV.

Event mixing method to subtract the background

The procedure by using the mixing event technique to subtract the background has been introduced in the previous chapter. In pp collisions, there is no strong combinatorial background at high p_T ($> 6\ GeV/c$) in real events and what we are concerned with is the lower p_T contribution to the π^0 peak. In this analysis, the buffer size of mixed events is set to 50, which is larger than in PbPb collisions, in order to construct enough statistics at larger p_T to fulfill the analysis requirement. Fig. 5.14 shows the example of ratio real/mix measured in pp collisions at 7 TeV. The distribution are fitted with a Gaussian with a second order polynomial function. The ratio is not constant outside the nominal π^0 mass window because of the presence of the uncorrelated background.

The real distributions and normalized backgrounds are shown in Fig. 5.15 and 5.16 respectively. At higher p_T, there is no background obtained by mixing event procedure, the mathematic fitting method is used. The signals after the background subtraction are shown from Fig. 5.17 to Fig. 5.20. At low p_T, the correlated background still exists which is a deflection of the mixing event technique.

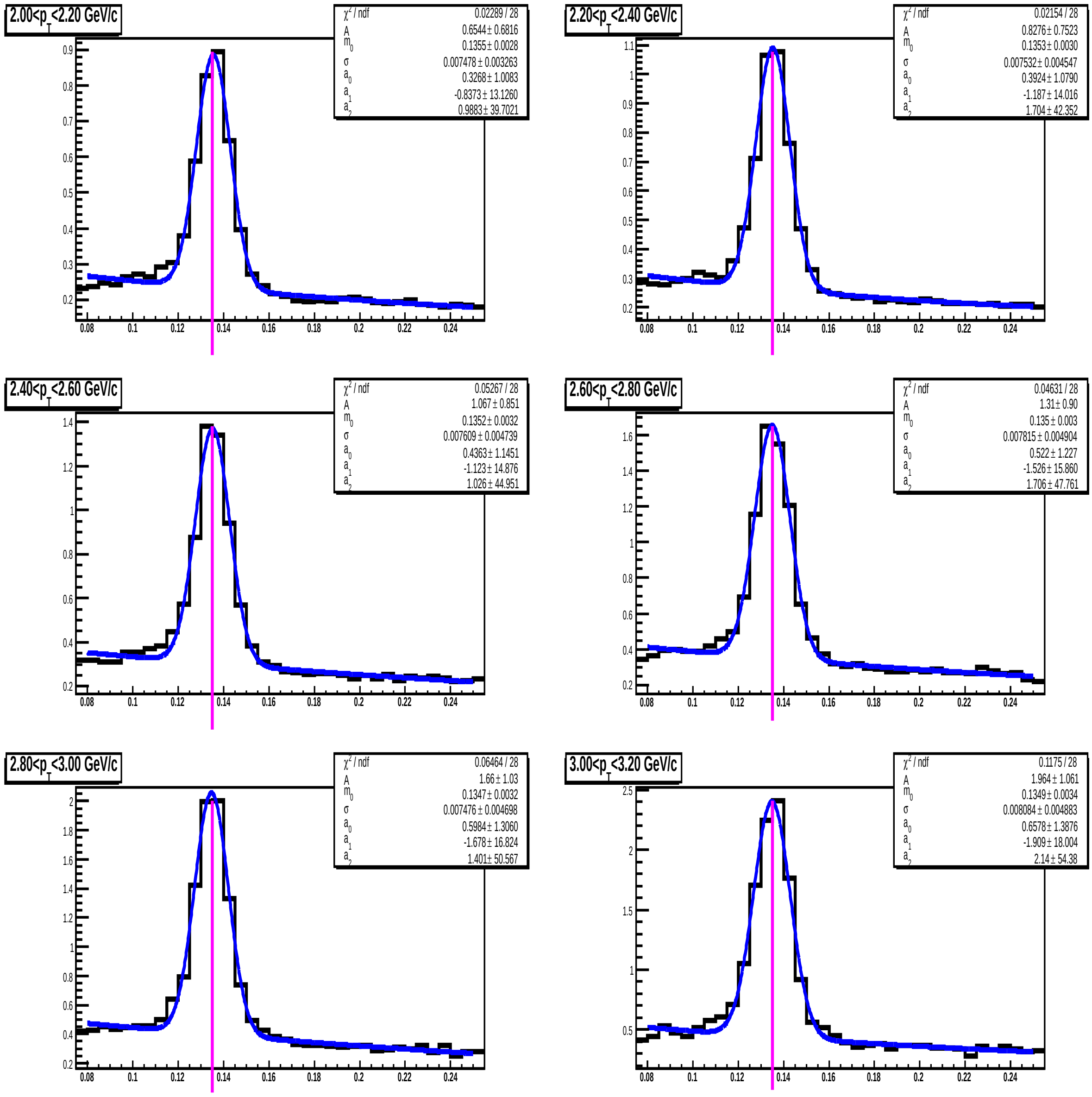

Figure 5.14: Ratio of real/mix at $2.0 < p_T < 3.2$ GeV/c measured in PHOS for pp collisions at 7 TeV. The distributions are fitted with a Gaussian plus a second order polynomial function.

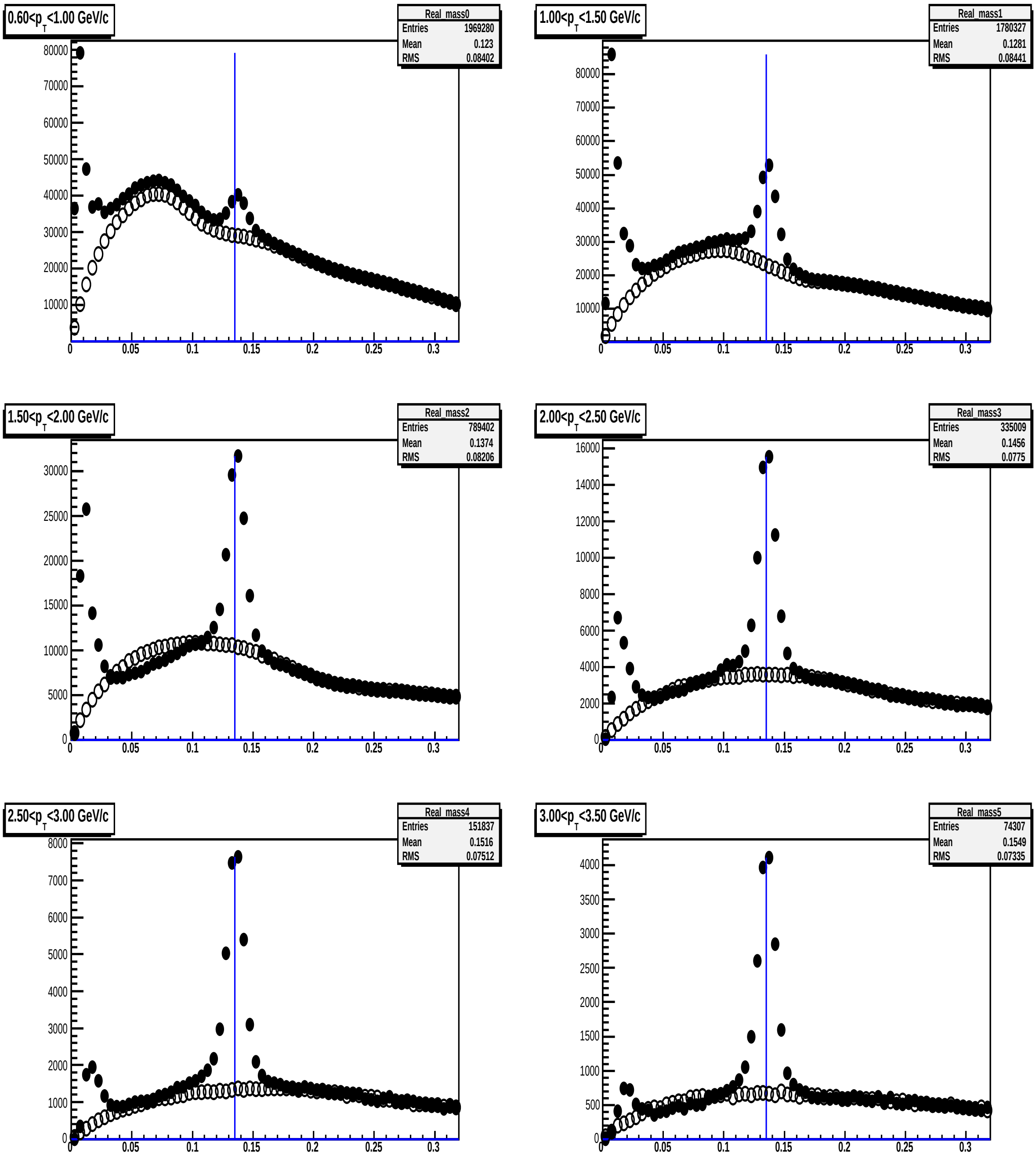

Figure 5.15: PHOS, in pp collisions at 7 TeV: The real distribution (dot) and the normalized background (open circle) at $0.6 < p_T < 3.5\ GeV/c$.

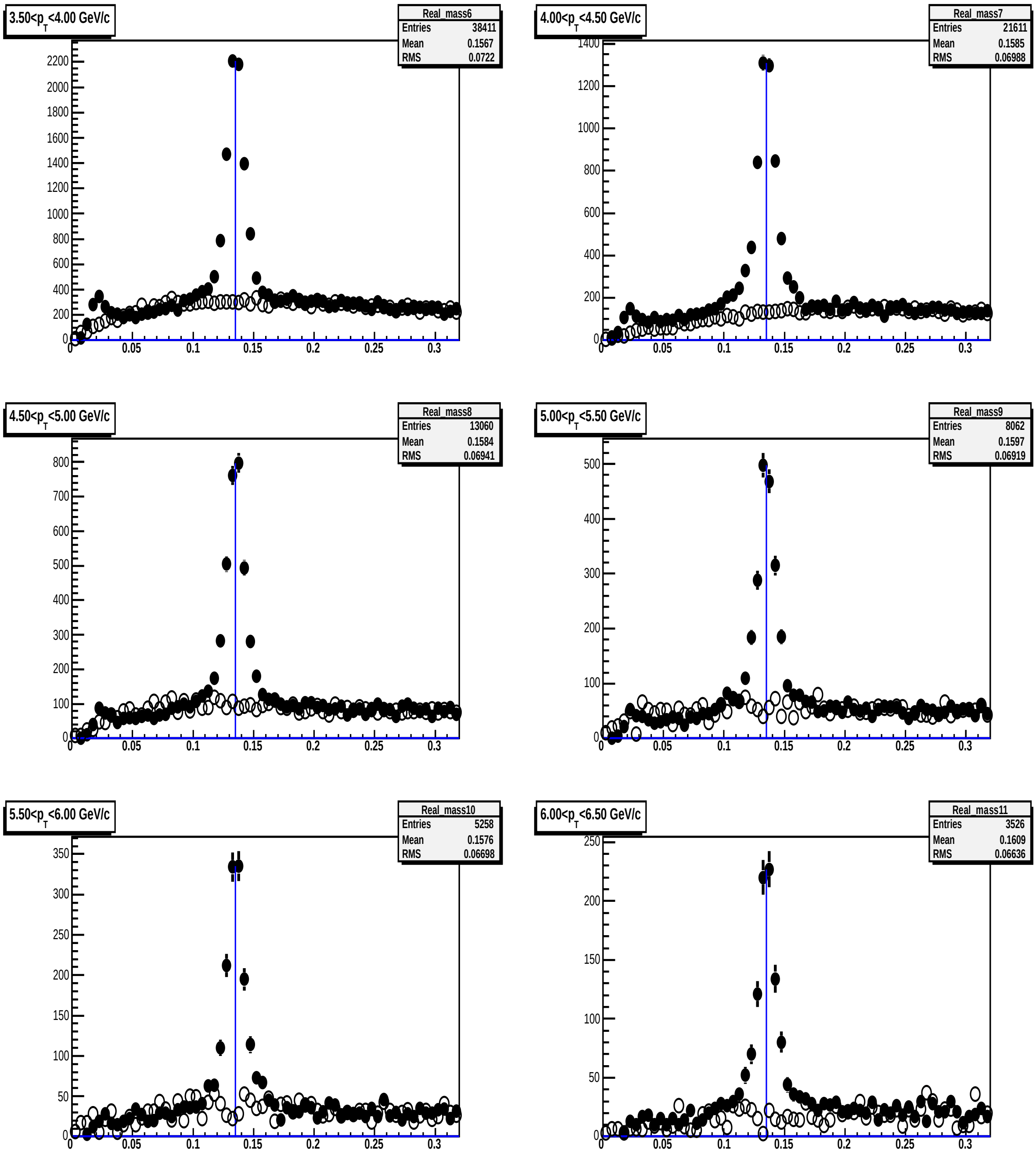

Figure 5.16: PHOS, in pp collisions at 7 TeV: The real distribution (dot) and the normalized background (open circle) at $3.5 < p_T < 6.5$ GeV/c.

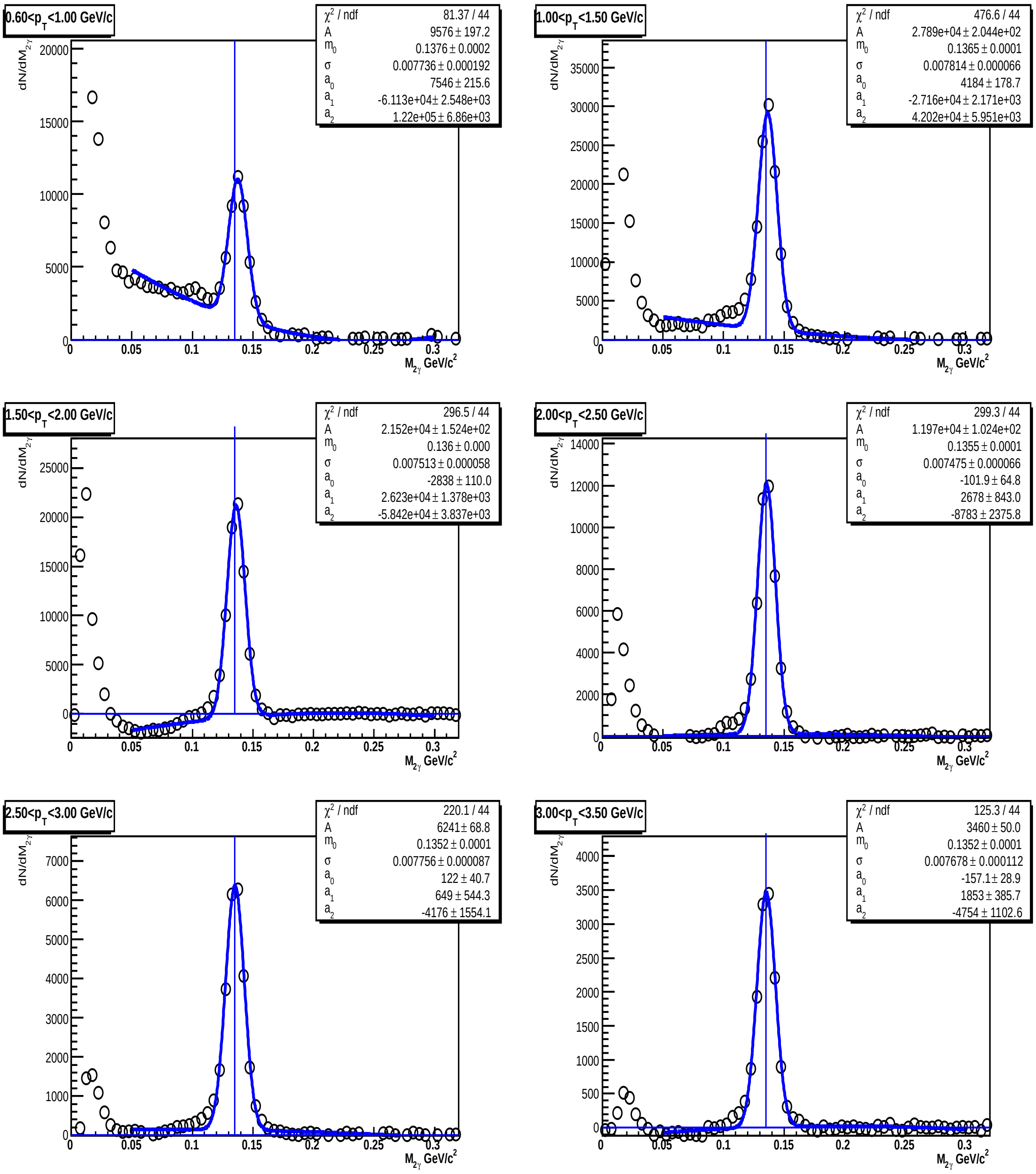

Figure 5.17: PHOS, in pp collisions at 7 TeV: The signal at $0.6 < p_T < 3.5$ GeV/c after the background subtraction fitted with a Gaussian and polynomial function.

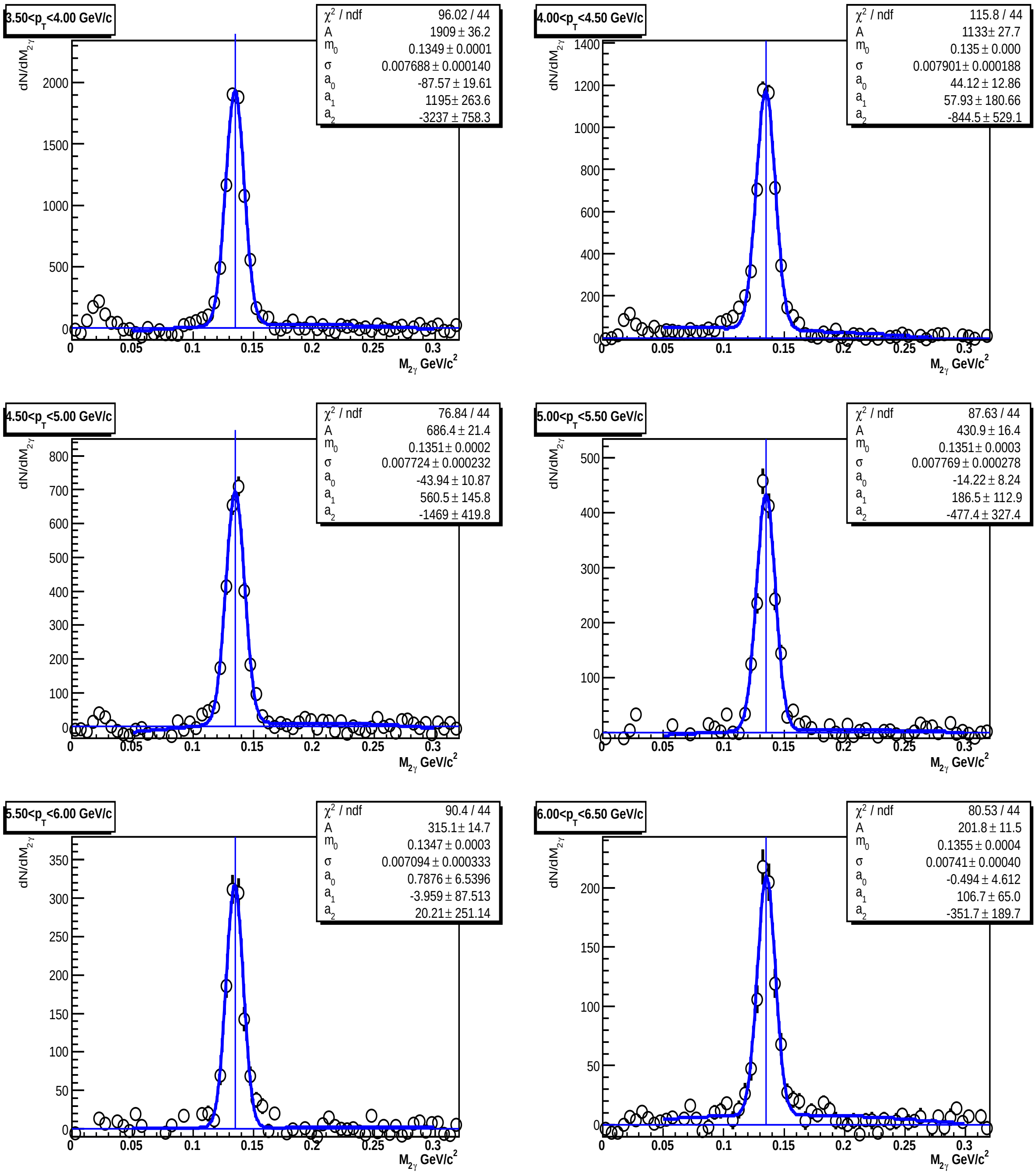

Figure 5.18: PHOS, in pp collisions at 7 TeV: The signal at $3.5 < p_T < 6.5\ GeV/c$ after the background subtraction fitted with Gaussian and polynomial function.

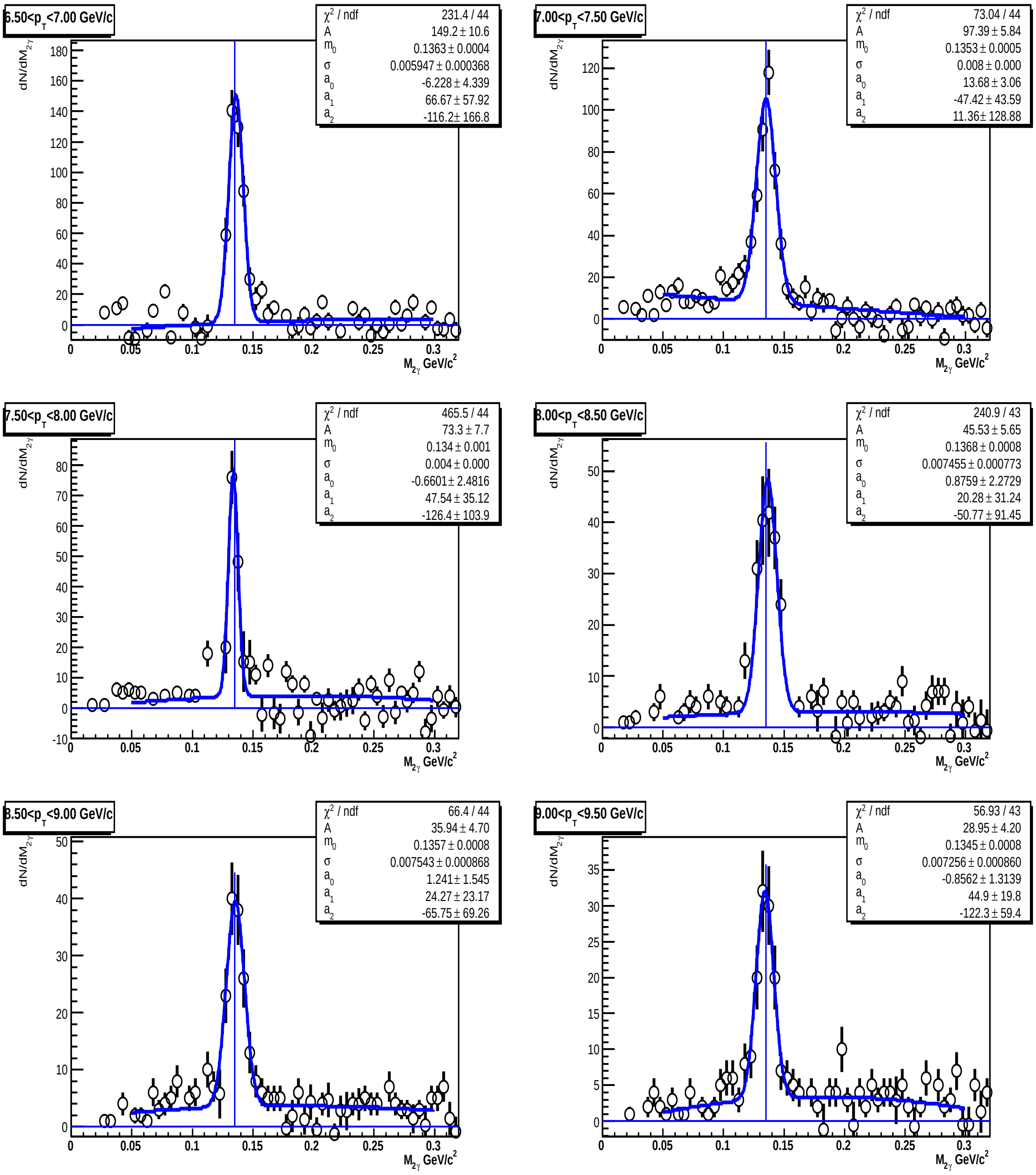

Figure 5.19: PHOS, in pp collisions at 7 TeV: The signal at $9.5 < p_T < 9.5$ GeV/c after the background subtraction fitted with a Gaussian and function.

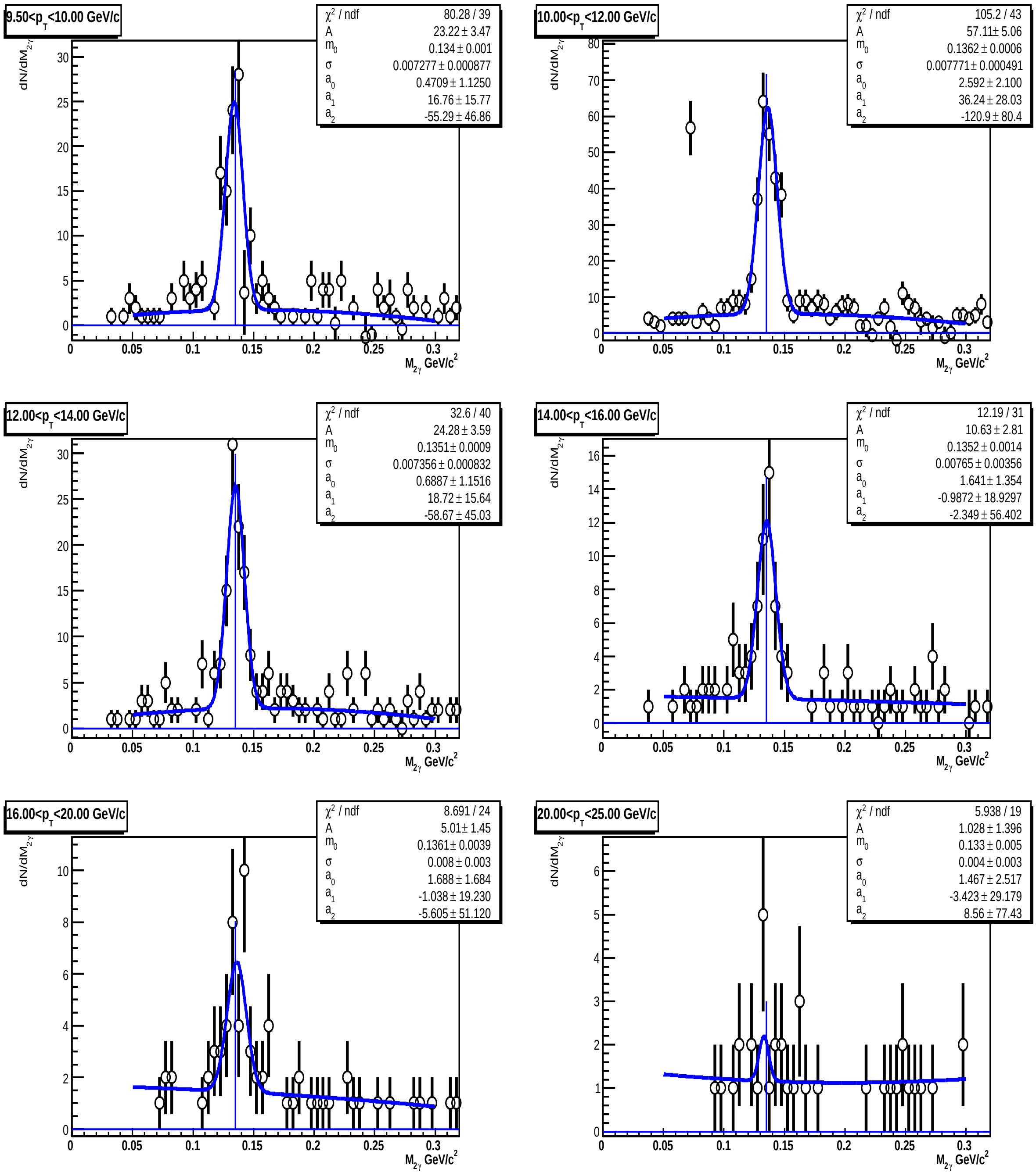

Figure 5.20: PHOS, in pp collisions at 7 TeV: The signal at $9.5 < p_T < 25.0\ GeV/c$ after the background subtraction fitted with a Gaussian and polynomial function.

5.5 $\eta \to 2\gamma$ reconstruction

The same procedure as the one used for π^0 reconstruction is applied for the η reconstruction. Due to lower yields, here the two photon invariant mass distribution at $4.0 < p_T < 6.0$ GeV/c and $6.0 < p_T < 8.0$ GeV/c around the nominal η mass are shown in Fig. 5.21 and Fig. 5.22. The red lines are related to the signals obtained after the fit procedure using with a Gaussian and a second order polynomial function. Clear signal can be seen. Limited by the statistics, we will not go further on this analysis.

5.6 $\omega(782) \to \pi^0\gamma \to 3\gamma$ reconstruction

The detection of $\omega(782) \to \pi^0\gamma \to 3\gamma$ was validated in 2009 in pp collisions at 10 TeV by simulations using pythia Monte Carlo production (LHC09a4) [104]. Up to now, from the data taking period 2009-2010, this detection channel still can not be extracted as expected in Chapter 2 when an integral luminosity is set to 4.7 nb^{-1} as in the first year data taking in pp collisions at 7 TeV. However, clear peaks round $\omega(782)$ nominal mass have been observed as shown in Fig. 5.23 for PHOS at $p_T > 4.0$ GeV/c and in Fig. 5.24 and 5.25 for EMCAL at $4.0 < p_T < 6.0$ GeV/c and $6.0 < p_T < 8.0$ GeV/c respectively. We didn't obtain $\omega(782)$ spectrum because the intrinsic limited acceptance and bad channels for PHOS and some problems on detector calibration, non-linearity corrections and cluster finding and unfolding algorithms for EMCAL. Here for EMCAL, due to it larger granularity and limitation of cluster unfolding capability, we assume high $p_T > 5$ GeV/c clusters are merged by the two decay photons from π^0. So it is looped with the second cluster to reconstruct $\omega(782)$. In principle, this method is weakly dependent on the unfolding capability. However, to get the final physics result, more simulation analyses are further needed in parallel with the cumulation of real data from the following years.

5.7 Summary

This chapter has been presenting the analysis of pp collisions at 7 TeV with PHOS detector. 231 runs with 366 million events have analyzed. The raw spectra are shown in Fig. 5.26 for π^0 by using the cuts

1) $p_T < 0.3$ GeV/c;

2) $N_{cells} > 2$ for PHOS and $N_{cells} > 1$ for EMCAL;

3) Distance to bad channel cut is larger than 1 cell/tower size;

4) The asymmetry of two cluster energies is less than 0.8.

The same cuts will be used for the calculation of acceptance and reconstruction efficiency to correct the raw spectra in next chapter.

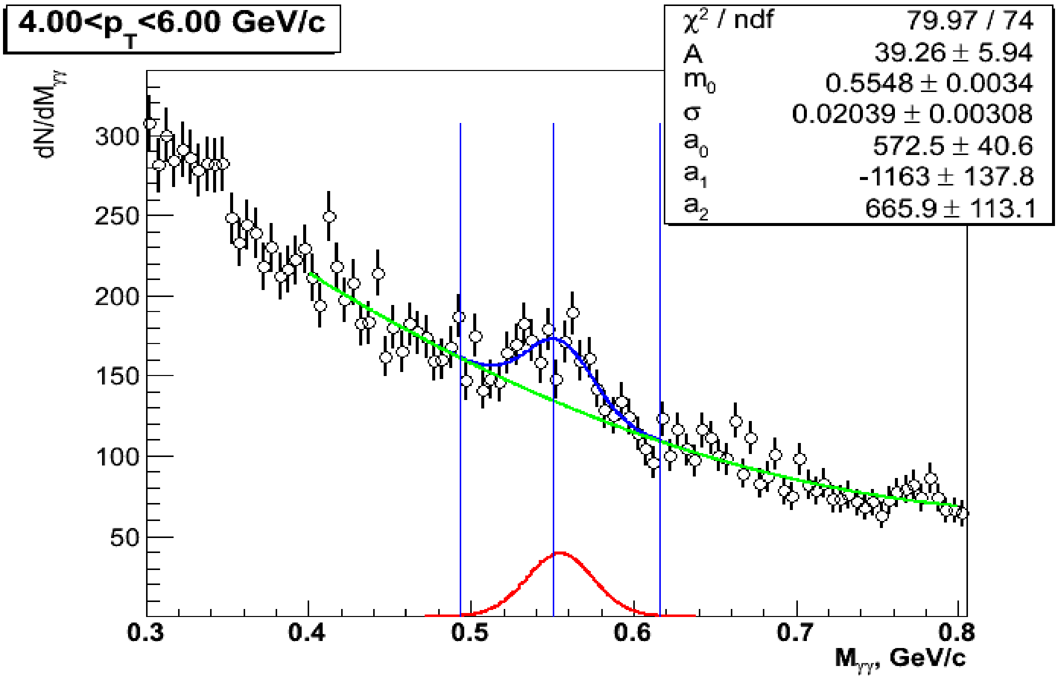

Figure 5.21: PHOS, in pp collisions at 7 TeV: The 2γ invariant mass distribution round the η mass at $4.0 < p_T < 6.0$ GeV/c fitted with a gaussian and second order polynomial function.

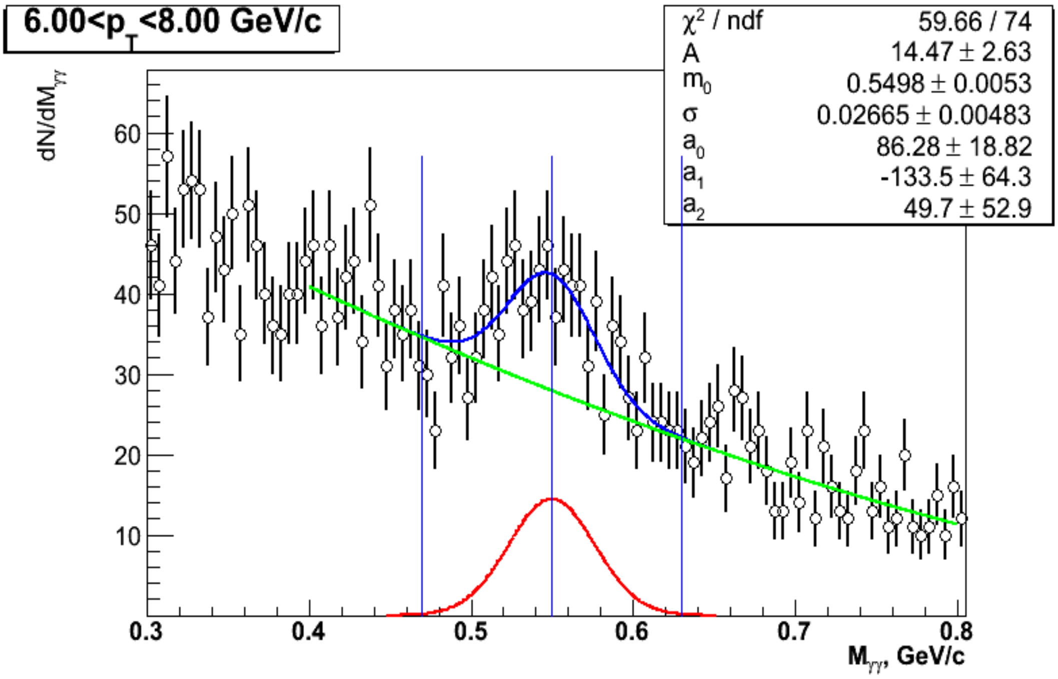

Figure 5.22: PHOS, in pp collisions at 7 TeV: The 2γ invariant mass distribution round the η mass at $6.0 < p_T < 8.0$ GeV/c fitted with a gaussian and second order polynomial function.

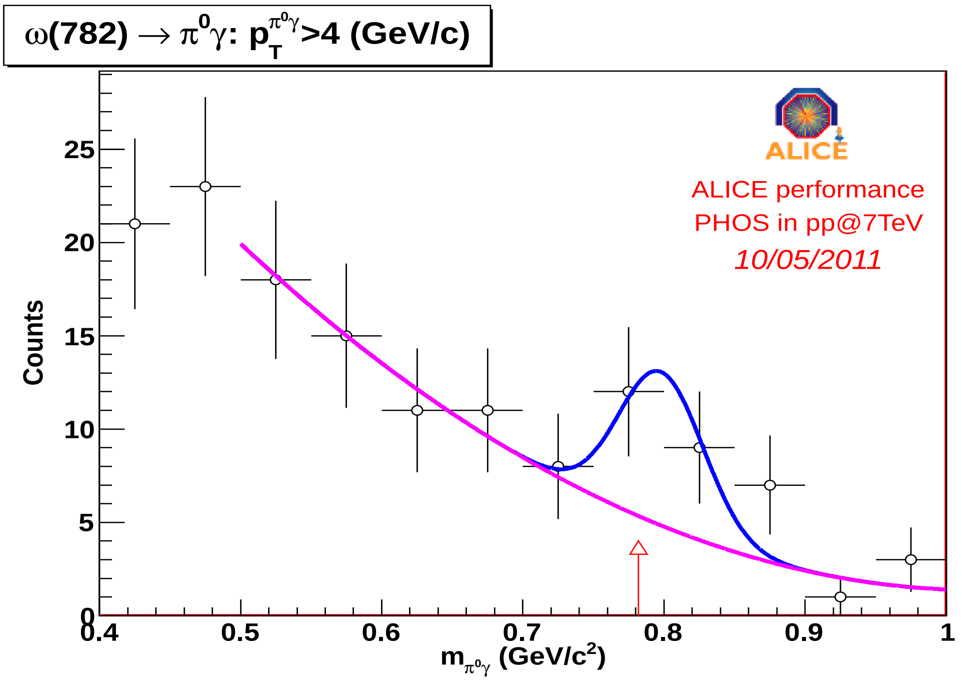

Figure 5.23: PHOS, in pp collisions at 7 TeV: The $\pi^0\gamma$ invariant mass distribution round the $\omega(782)$ mass at $p_T > 4.0$ GeV/c fitted with a gaussian and second order polynomial function.

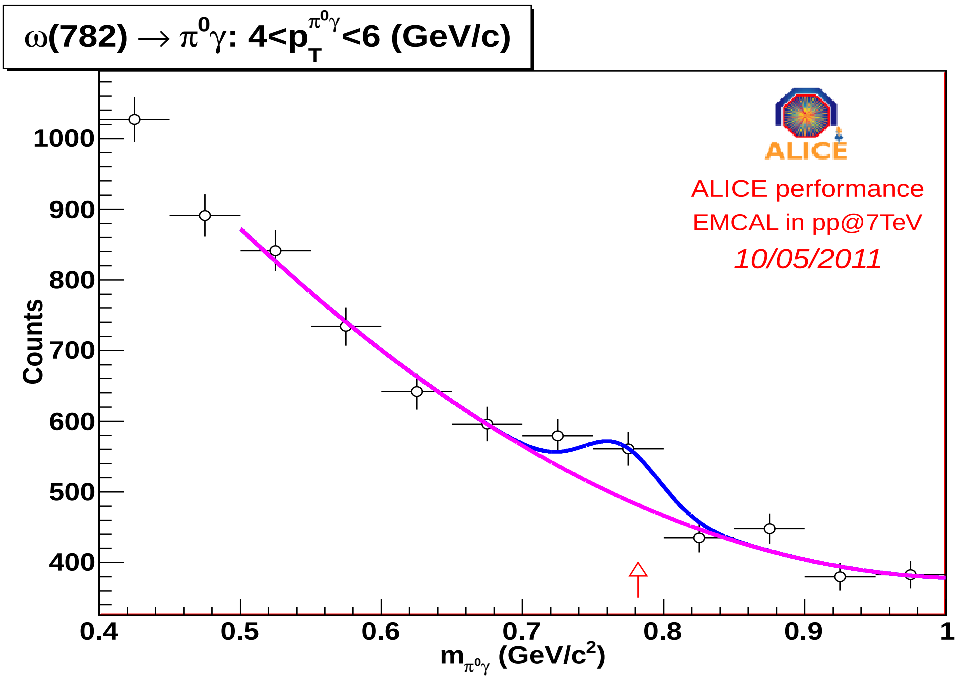

Figure 5.24: EMCAL, in pp collisions at 7 TeV: The $\pi^0\gamma$ invariant mass distribution round the $\omega(782)$ mass at $4.0 < p_T < 6.0$ GeV/c fitted with a gaussian and second order polynomial function.

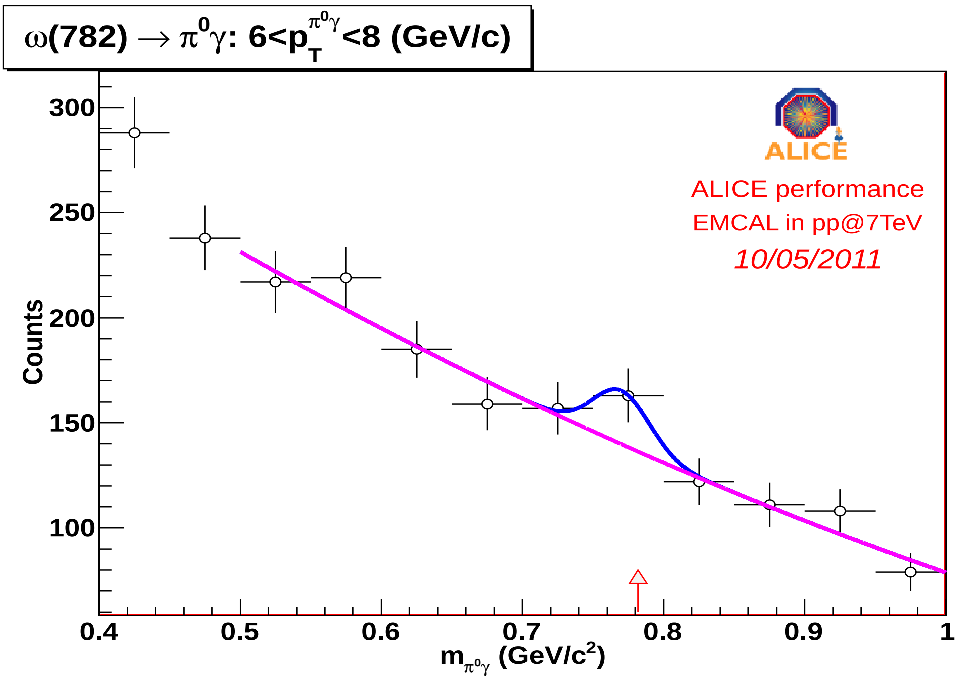

Figure 5.25: EMCAL, in pp collisions at 7 TeV: The $\pi^0\gamma$ invariant mass distribution round the $\omega(782)$ mass at $6.0 < p_T < 8.0$ GeV/c fitted with a gaussian and second order polynomial function.

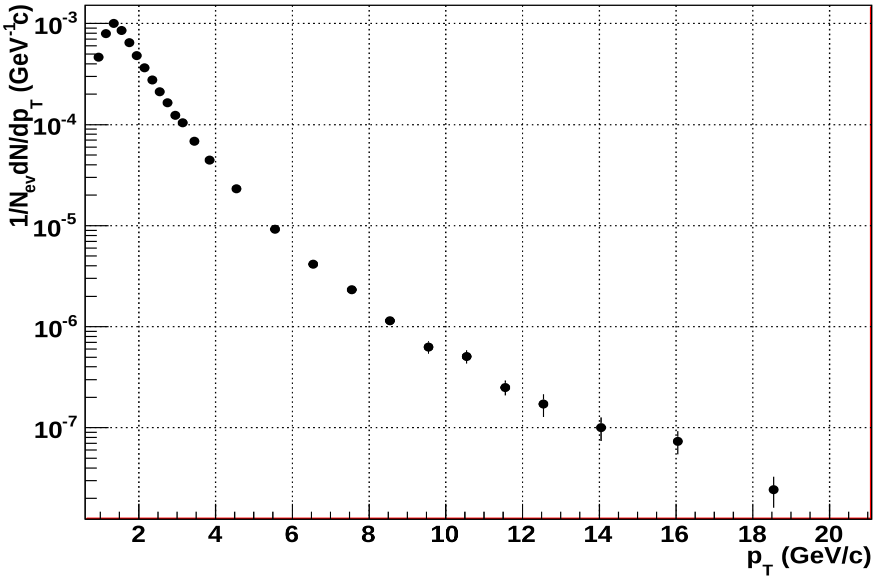

Figure 5.26: π^0 raw yield by the invariant mass of 2γ in PHOS with pp collisions at 7 TeV. The spectrum is normalized to the total number of events.

Chapter 6

Corrections and uncertainties

The first physics goal with PHOS and EMCAL aim at measuring the invariant cross section of light neutral mesons in pp collisions as a reference for heavy-ion collisions, expressed by the formula quoted below:

$$\frac{1}{N_{ev}}\frac{d^2N}{2\pi p_T dp_T dy} = \frac{1}{N_{ev}}\frac{\Delta N}{2\pi p_T \Delta p_T \Delta y} \cdot \frac{1}{\epsilon_{Acc\times Rec}} \cdot \frac{1}{Br}, \tag{6.1}$$

where the ϵ is the correction factor from geometrical acceptance and reconstruction efficiency, and the Br is the decay branching ratio of detection channel. In this chapter, the correction factor is calculated and the systematic uncertainties due to the absolute scale of the energy, non-linearity response, raw yield extraction methods by different fitting functions, bad channel maps and π^0 loss by conversion or off-vertex are estimated.

6.1 Acceptance and reconstruction efficiency

Here we take into account the acceptance and reconstruction efficiency together defined by the formula

$$\varepsilon = \frac{\frac{dN^{\pi^0}_{Rec}}{dp_T}}{\frac{dN^{\pi^0}_{Gen}}{dp_T}(|\Delta\eta| = 1; \Delta\phi = 2\pi)}. \tag{6.2}$$

In this case, there is not necessary to calculate the photon conversion efficiency and other corrections, which has been included in the above formula to minimize the uncertainties caused by the simulation.

The efficiency is calculated by Monte Carlo simulation with a single π^0 event with an uniform distribution over a large transverse momentum range $0.1 < p_T < 25\ GeV/c$, azimuthal angle coverage of 2π and a unity rapidity. The generated events go through ALICE full detectors as the environment used in 2009∼2010 data taking. During the event reconstruction, the same condition data was used as in real-data reconstruction. The real bad channel map was used in reconstruction of PHOS data.

Besides, the invariant mass spectrum was constructed with the same cluster criteria describe in Chapter 5. The calculated efficiency is shown in Fig. 6.1, which is fitted with a function [1]:

$$f(x) = (a + bx)[1 - e^{\frac{-x+c}{d}}] \tag{6.3}$$

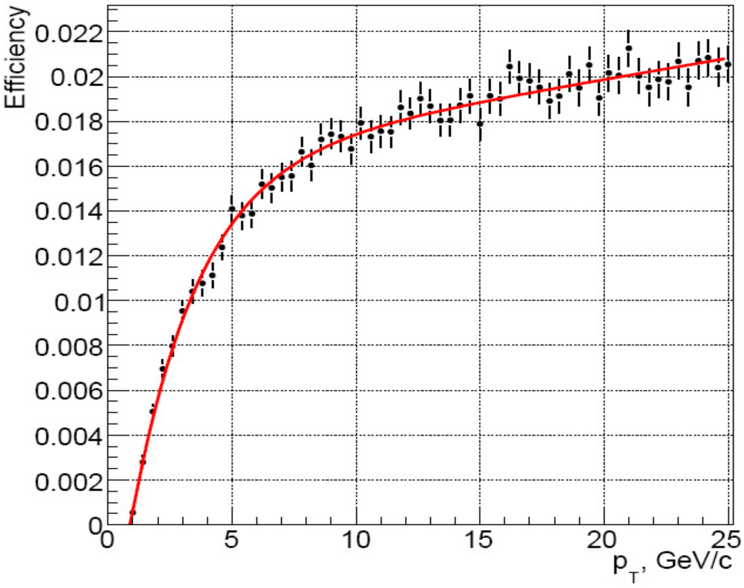

Figure 6.1: PHOS: Geometrical acceptance and reconstruction efficiency for π^0 as a function of p_T.

and the fitting parameters are listed in:

	a	b	c	d
PHOS	$(1.61\pm0.06)\cdot10^{-2}$	$(1.9\pm0.3)\cdot10^{-4}$	0.09 ± 0.02	2.64 ± 0.17

6.2 Systematical uncertainties

The systematical uncertainties are classified and estimated due to

a) absolute energy scale calibration;

b) non-linearity of the detector response;

c) influence of bad channels mapping;

d) raw yield extraction by different fitting methods;

e) π^0 conversion loss and recovery by the detector materials;

f) contribution from off-vertex π^0.

---

[1] See more details in ALICE internal note.

6.2.1 Absolute energy scale

As we discussed in Chapter 3, for PHOS, there was no absolute energy calibration for the whole three modules instead of pre-calibration based on the APD gain data sheet. When we took the first data with pp collisions at 900 GeV, we did not observe the π^0 peaks due to the incorrect absolute energy scale. Then the calibration was done by using the π^0 peak till we put the π^0 peak in the correct position (not absolutely in its PDG mass). However, there are some discrepancy between the Monte Carlo simulation and real data with a little shift of the peak position, which is mainly due to the energy resolution. Then the improved calibration had been done to adjust the π^0 peak position consistent at $p_T = 3\ GeV/c$ in Monte Carlo and data.

When using the π^0 to calibrate the detector, it incorporates the errors from energy resolution in Monte Carlo simulation and the detector alignment. The latter means the distance from the PHOS surface to the beam interaction point. The value was measured through the photogrammetry with a high precision. The cross-check study was performed by track matching study and found the value of the uncertainty due to this misalignment is about $\sim (1.0 \pm 0.5) \cdot 10^{-3}$, which should be the dominant uncertainty for the absolute scale of the cluster energy.

6.2.2 Detector non-linearity response

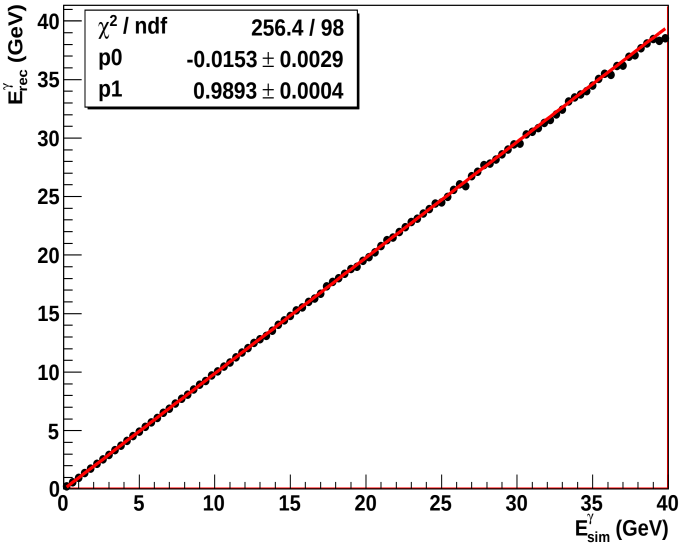

Figure 6.2: PHOS: simulation study of the photon non-linearity with the single photon per event over the p_T range from 0 to 40 GeV/c.

Fig. 6.2 shows the PHOS non-linearity response with the single photon per event over a range of $0 < p_T < 40\ GeV/c$ from simulation. The slope is 0.9893 ± 0.0004.

However, the π^0 position depends on the p_T presented in Chapter 5, which is mainly due to the non-linearity of the detector, especially at lower p_T. The best way to take this effect into account is to assign a compensation factor f(E) and Gaussian smeared energy to each reconstructed cluster

$$E_{corr} = E \cdot f(E), \tag{6.4}$$

so that the uncertainty due to the detector non-linearity can be estimated.

The non-linearity correction function can be determined by several ways for the cross-check and error estimation, such as from the Monte Carlo simulation with the OCDB as in real data, from the invariant mass of photon and conversions, from the symmetrical decay of $\pi^0 \to 2\gamma$, and from beam test.

For PHOS, the parameterization of non-linearity correction function $f(E) = 1 + a \times exp^{-E/b}$ with two sets of parameters (0.1, 0.4) and (0.2, 0.5), and a Gaussian smeared energy $\sigma = 0.065\ GeV$ were studied both in real data and simulation. At lower transverse momentum range the uncertainties are estimated by comparing the raw π^0 yield in Monte Carlo and data and found the systematic errors are 27% at $p_T = 0.8\ GeV/c$, 17% at $p_T = 1\ GeV/c$, 3% at $p_T = 1.2\ GeV/c$, 2% at $p_T = 1.4\ GeV/c$ and $< 2\%$ at $1.4 < p_T < 12\ GeV/c$. At higher $p_T > 12\ GeV/c$, the error is estimated by fitting the π^0 peak position and found the value is $< 1\%$.

6.2.3 Bad channels

The bad channel map is called during the event reconstruction. However, not all the bad channels are properly marked, which will influence the raw π^0 yield spectrum. Here the relevant uncertainty due to bad channels map is estimated.

The variation of the distance from the cluster coordinates to the closest bad channel center was performed to study the dependence. Here four distance cuts are used in this analysis: without distance cut, larger than 1, 2 or 3 cell-sizes. It is studied by comparing in Monte Carlo and real data by using the cuts. In simulation, the reconstruction efficiency is defined as

$$\varepsilon_{rec.}(d_i) = \frac{\frac{dN^{\pi^0}_{sim-rec}}{dp_T}}{\frac{dN^{\pi^0}_{sim-in-phos-acc}}{dp_T}}. \tag{6.5}$$

Then it is used in the formula below to calculate the produced spectrum with the corrected reconstruction efficiency

$$\frac{dN^{\pi^0}_{prod}}{dp_T}(d_i) = \frac{1}{\varepsilon_{rec.}(d_i)} \frac{dN^{\pi^0}_{data-rec.}}{dp_T}(d_i). \tag{6.6}$$

And the relative uncertainty can be expressed as below:

$$\sigma = \frac{\frac{dN^{\pi^0}_{prod}}{dp_T}(d_i)}{\frac{dN^{\pi^0}_{prod}}{dp_T}(d_j)} - 1 = \frac{\frac{1}{\frac{dN^{\pi^0}_{sim-rec}}{dp_T}(d_i)}\frac{dN^{\pi^0}_{data-rec}}{dp_T}(d_i)}{\frac{1}{\frac{dN^{\pi^0}_{sim-rec}}{dp_T}(d_j)}\frac{dN^{\pi^0}_{data-rec}}{dp_T}(d_j)} - 1 \tag{6.7}$$

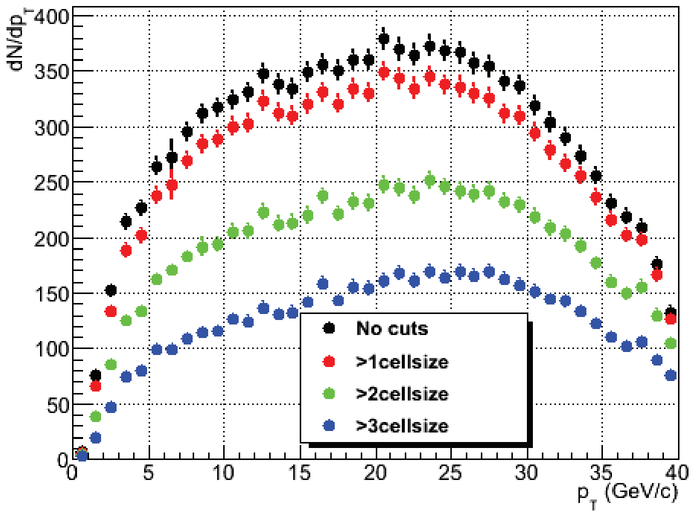

(a) Simulation

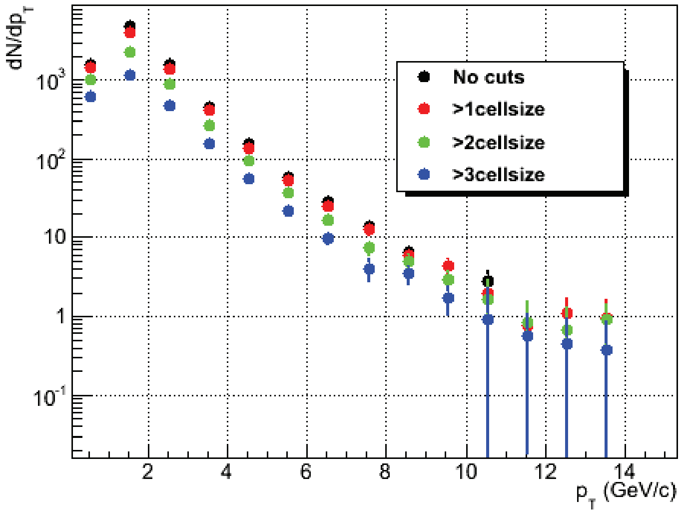

(b) pp@7TeV

Figure 6.3: PHOS: The π^0 raw yield distribution with the four distance to bad channel cuts in simulation (a) and real data (b). The analysis is performed under the same analysis conditions.

From the above formula, to get the relative uncertainty we need to calculate the π^0 raw yield spectrum both in simulation and real data by using the same analysis conditions. Fig. 6.3 shows the π^0 raw yield distribution both in Monte Carlo and real data after the rejection of the cluster with a closest distance smaller than 1, 2 and 3 cell-sizes. From these two distributions, the relative uncertainty is estimated as shown in Fig. 6.4, which demonstrates that the uncertainties in the π^0 production spectrum will not exceed 0.02 in the range $2 < p_T < 7$ GeV/c and $< 15\%$ at $p_T < 2$ GeV/c and $p_T > 7$ GeV/c.

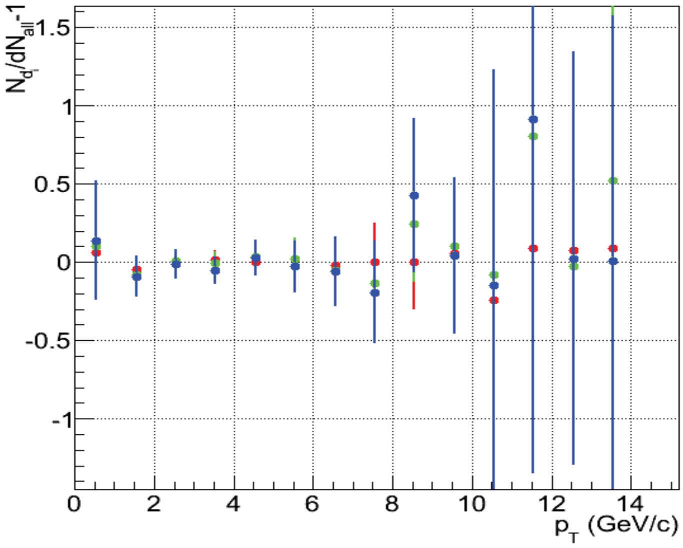

Figure 6.4: Relative uncertainties of the π^0 raw spectra due to the bad channel map.

6.2.4 Raw yield extraction by different fitting methods

As introduced in Chapter 3, the π^0 raw yield extraction are performed by mathematical fitting and mixing event technique. The choice of different fitting functions and the counting methods will introduce the systematic errors to the raw yield spectra. Several aspects are taken into account to estimate the uncertainties:

- With/Without mixing events;
- Fitting methods to extract the raw spectra with different combination of Gaussian (Crystal ball) and n^{th} order polynomial function;
- Consideration of various ranges of invariant mass spectra for fit;
- Counting method by integrate the histogram or fitting function;
- The different integration mass windows ($\overline{m} \pm n\sigma$).

Fig. 6.5(a) presents the raw π^0 spectra from real data for pp collision at 7 TeV by using different fitting functions with/without mixing events. Fig. 6.5(b) presents the relative variation between the raw yield spectra. Due to the overestimated/unknown the combinatorial background, by using the mathematical fitting method with a Gaussian and polynomial function has a large variation $\sim 8\%$. To extract the final spectrum we use the mixing event technique to subtract the background. Here we estimated that the uncertainties due to the signal extraction amount 3% in the whole p_T range.

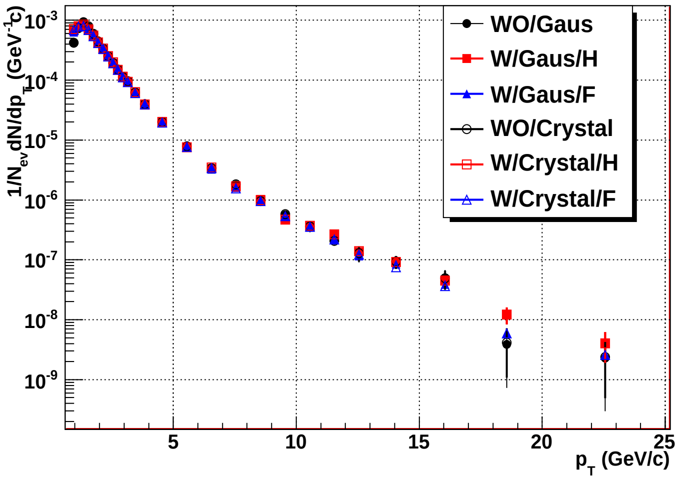

(a) Raw yield

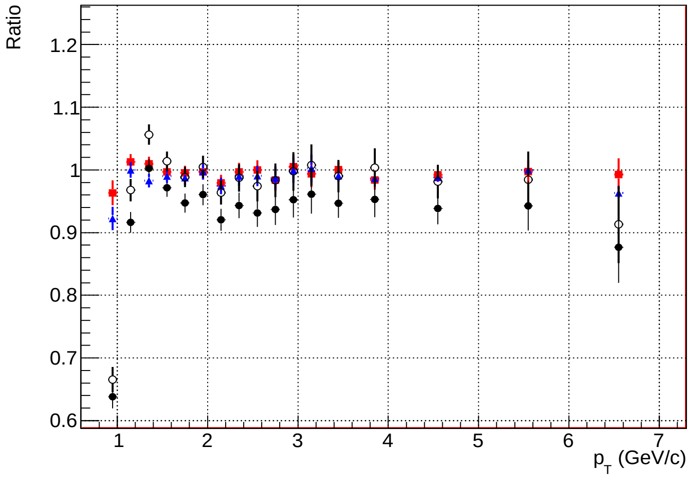

(b) Relative uncertainties

Figure 6.5: The π^0 raw yield spectra by 2γ invariant mass analysis with/without mixing event technique and fitted by Gaussian+polN and CrystalBall+PolN functions.

6.2.5 π^0 conversion loss and recovery

The photon conversion ($\gamma \to e^- e^+$) may take place anywhere between the electro-magnetic calorimeters and the collision vertex, due to the material budget of the detector or support structure, and air atoms. So that the number of π^0 will be reduced as shown in Fig. 6.6. This effect is called conversion loss which is dominant in TPC.

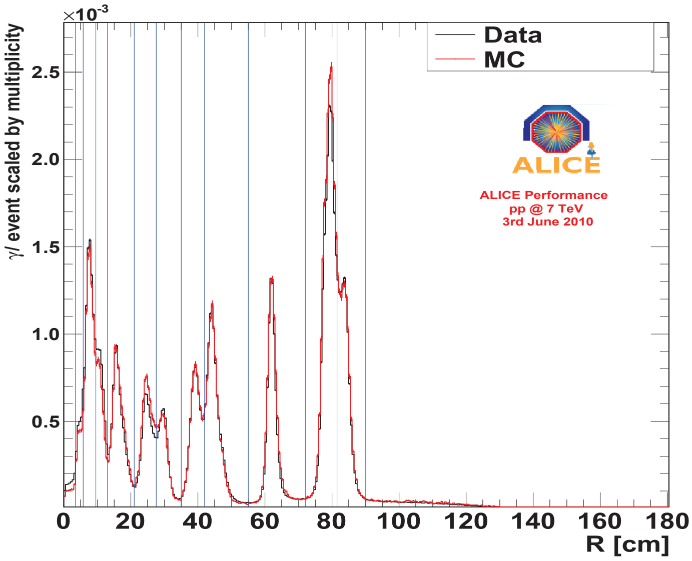

Figure 6.6: Radial distance distribution of the gamma conversion points compared between pp collisions at 7 TeV data and Monte Carlo simulation.

Depending on the transverse momentum of electrons (or positrons), some of them may hit on the surface of electro-magnetic calorimeters. With the help of position matching in the surface of electro-magnetic calorimeters between the track propagation and the cluster, some of them could be rejected. However, for the neutral mesons analysis, we do not use the particle identification information. So that some additional number of π^0 are still be reconstructed by a photon cluster and a electron (positron) cluster. The contribution from this part is so called "recovery".

Actually, the correction by the photon conversion and recovery has been included in the efficiency as Eq. 6.2. Here we estimate the uncertainties by comparing simulation and real data under different detector configurations.

Simulation study

The simulation study by single π^0 per event with an uniform distribution was studied under two configurations:

1) L3 magnet is off, and only the PHOS detector is switched on;

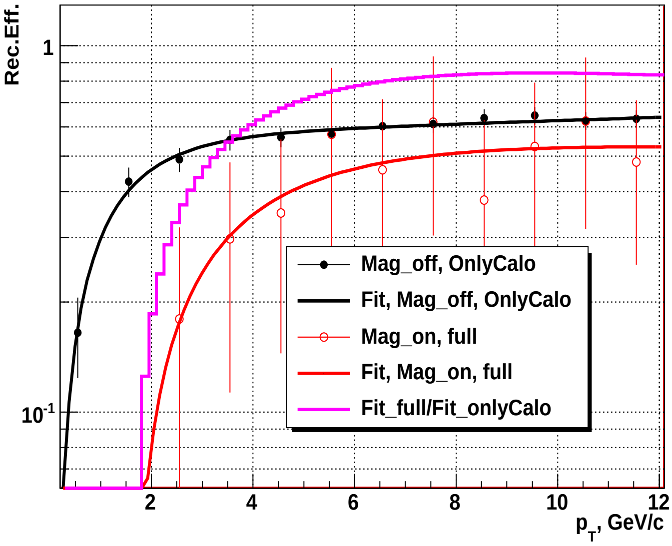

Figure 6.7: PHOS: Ratio of the reconstructed π^0 to the input π^0 as a function of p_T, simulated with single π^0 per event with two configurations. Black: L3 magnet off, only PHOS on. Red circle: full simulation with L3 magnet. Pink: ratio of the full simulation to the one where only PHOS is on.

2) L3 magnet is on. All other detectors are switched on with the same configuration as in the data taking period 2009∼2010.

As shown in Fig. 6.7, at the intermediate $p_T > 4\ GeV/c$ the reconstruction efficiency is close to saturation, $\sim 50\%$ with the full simulation and $\sim 60\%$ with only calorimeter and without the L3 magnet. So that ratio of measured π^0 with full simulation with magnetic filed to the measured π^0 without magnetic field is 82.2%±0.46% at high p_T, which demonstrates that conversion probability amount 17.8% for at least one conversion from the decay photons.

Real data with pp collisions at 7 TeV

The real data with pp collisions at 7 TeV are also analyzed with ALICE magnet field status on and off. Some of the runs in the physics partition LHC10c are selected:

1) With L3 magnet on. 1 run, ∼6 million events: 119965;

2) With magnetic field off. 11 runs, ∼5 million events: 119041, 119047, 119055, 119057, 119061, 119067, 119077, 119079, 119084, 119085, 119086.

The π^0 raw yield normalized to the number of events are shown in Fig. 6.8 from the above two groups of runs, while the ratio between them is shown in Fig. 6.9. Due to the fact that the data sample is small, here we measure the π^0 spectrum with a p_T range from 0 to 6 GeV/c. After fitting the ratio of the L3 magnet is on and off, the value amount 0.832±0.098(statistic error).

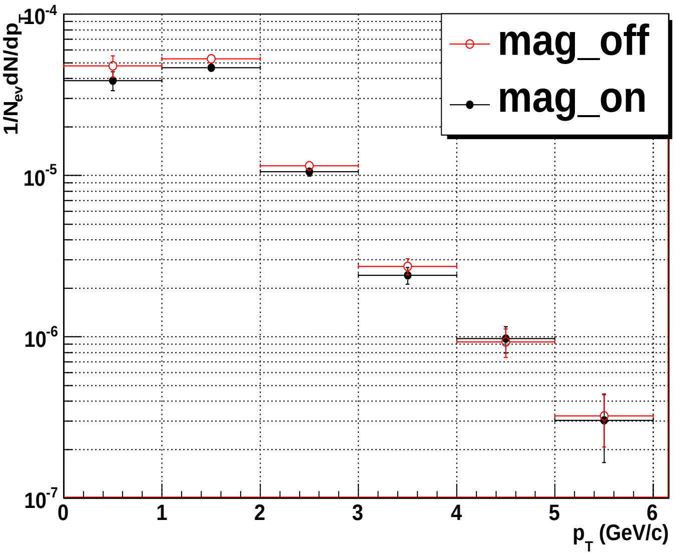

Figure 6.8: The π^0 raw yield normalized to the number of events in pp collisions at 7 TeV with the ALICE magnetic field on (black point) and off (red circle).

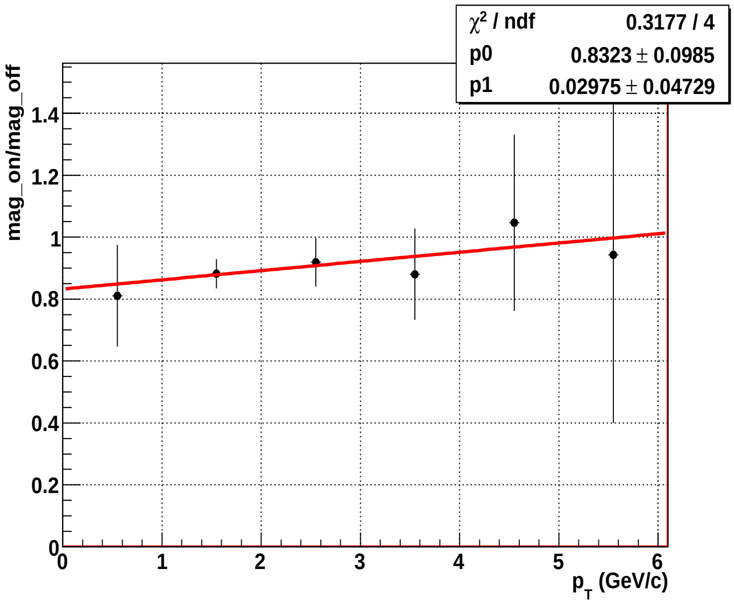

Figure 6.9: Ratio of the π^0 yield with magnetic field to the yield without magnetic. The red line is fitted by a first order polynomial function.

The results of the systematic uncertainties due to the material budget within TPC as +5.18%-4.69%, imply to propagate 0.5% systematic error to the π^0 correction factor. In addition, the conversions between TPC and calorimeter are estimated from simulation as 12.0%±6.6%. Since most of the converted photons near PHOS can be recovered, the π^0 loss probability between TPC and PHOS is reduced to 4.4%±2.6%.

In total, the systematic errors is 3.1% (as a sum of 0.5% from TPC and 2.6% from outside TPC) due to photon conversion and recovery.

6.2.6 Contributions from off-vertex π^0

In our measurement, the photons/clusters are supposed to be produced from the primary vertex so that π^0s are also produced from the interaction point. However, two main processes:

1) Hadronic decay, such as $\eta \to 3\pi^0$ and $K^0_{S,L} \to 3\pi^0$;

2) Charged exchange reaction, $\pi^\pm + X \to \pi^0 + X^\pm$.

The source of these generate π^0s which do not originate from the collision vertex and can not be excluded during the analysis, which will introduce additional systematic uncertainties for the π^0 measurement.

Fig. 6.10 shows the ratio of π^0 from non-vertex contribution to all the π^0 in PHOS acceptance, which is simulated by the PYTHIA generator without going through the ALICE detectors. About ∼5% is expected from the non-vertex hadronic decay. In the measurement, we can not measure the decay vertex thus impossible to correct this contribution. The detailed study on the charged exchange reaction with the detector material had been studied in [146], and found this contribution is almost ignorable with 0.04%±0.02%.

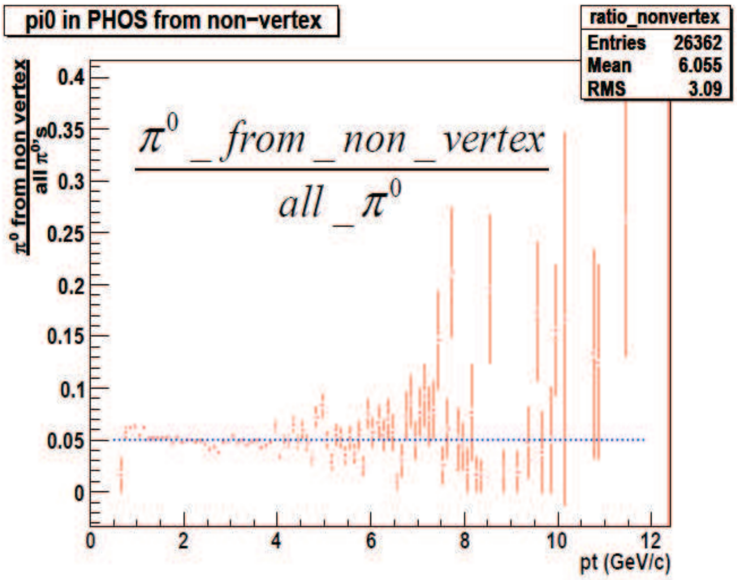

Figure 6.10: The ratio of π^0 from non-vertex contribution to all the generated with PYTHIA simulation.

Chapter 7

Results and outlook

In this last chapter, the final physics results of π^0 production yield and invariant differential cross section are presented. Comparing the production cross section, as well as the scaling behaviors with the existing world data points, we get the conclusions and outlook on the first measurement with ALICE electromagnetic calorimeters.

7.1 Fitting of π^0 spectrum

Particle spectrum fit distribution

It is well known from the existing the experimental data that at lower p_T (typically with a $p_T < 2\ GeV/c$) of the spectrum where the region is quite difficult to be fully understood due to the bulk properties. In this region, the spectrum can reveal the thermal emission with short-range correlations and obey to the Boltzmann-Gibbs statistics:

$$E\frac{d^3\sigma}{dp^3} = C_b e^{E/T} \tag{7.1}$$

where C_b is a normalization factor, E is the energy of the particle and T can be interpreted as the system temperature.

At higher $p_T > 2\ GeV/c$, particles are produced from the hard processes which can be well described by pQCD. Typically, it can be fitted by a power law function

$$E\frac{d^3\sigma}{dp^3} = Ap_T^{-\upsilon}, \tag{7.2}$$

where A is a normalization factor and υ is the power to describe the exponential shape.

However, there is no clear boundary between the soft and hard region to explain the mechanisms. Recently, the Tsallis parameterization [147] has been successfully used to fit the particle spectra. It derives from the Boltzmann-Gibbs entropy as

$$G_q(E) = C_q\Big(1 - (1-q)\frac{E}{T}\Big)^{1/(1-q)}, \tag{7.3}$$

where q is a nonextensivity parameter. To satisfy the normalization, q is limited in a range $(1, 1\frac{1}{3})$ and the coefficient C_q is expressed [148]

$$C_q = \frac{(2q-3)(q-2)}{T(T+m_0)-(q-1)(q-2)m_0^2} \frac{1}{(1-(1-q)\frac{m_0}{T})^{1/(1-q)}} \tag{7.4}$$

By replacing q with $n = -\frac{1}{1-q}$, the fitting function is given by:

$$E\frac{d^3\sigma}{dp^3} = \frac{1}{2\pi}\frac{d\sigma}{dy}\frac{(n-1)(n-2)}{(nT+m_0(n-1))(nT+m_0)}(\frac{nT+m_T}{nT+m_0})^{-n}, \tag{7.5}$$

where $m_T = \sqrt{m_0^2+p_T^2}$, $d\sigma/dy$ denotes the integrated cross section of the particle production at the midrapidity. Under the limit of $m_0 \to 0$, Eq. 7.5 becomes

$$E\frac{d^3\sigma}{dp^3} = \frac{1}{2\pi}\frac{d\sigma}{dy}\frac{(n-1)(n-2)}{(nT)^2}(1+\frac{m_T}{nT})^{-n}, \tag{7.6}$$

And this form has the similar expression than the QCD inspired formula suggested by Hagedorn. Besides, by connection of Eq. (7.2) and Eq.(7.5) one can get

$$n = \frac{\upsilon m_T^2}{p_T^2 - \upsilon T m_T} \tag{7.7}$$

Thus the best advantage of the Tsallis function is that it builds a single function to describe the full spectrum with an underlying physics interpretation. The two parameters T and n involved reflect the kinetic freeze-out temperature and the amount of temperature fluctuations (indirectly by q) respectively.

The production yield in pp at 7 *TeV* measured with PHOS in ALICE

The raw spectrum of π^0 after the correction of the geometrical acceptance, reconstruction efficiency and the branching ratio is shown in Fig. 7.1 with the statistic (blue box) and systematic (red box) uncertainties. The spectrum is fitted by Eq. 7.5 in a range of $0.8 < p_T < 25$ *GeV/c* and the fitting parameters are listed in Table 7.1. However, the results are expected to be further improved for a better fitting. And its also compared with the fitting results of mesons measured at RHIC in pp at 200 *GeV* [26, 149, 150]. At lower $p_T < 3$ *GeV/c*, the systematic uncertainties are dominant, while at higher $p_T > 15$ *GeV/c* the statistic uncertainties are dominant. The ratio between the data and the fitting is shown in the bottom plots. At intermediated p_T, the ratio is around 1, while it has a deviation of 20% at $p_T < 3$ *GeV/c* and $p_T > 10$ *GeV/c*.

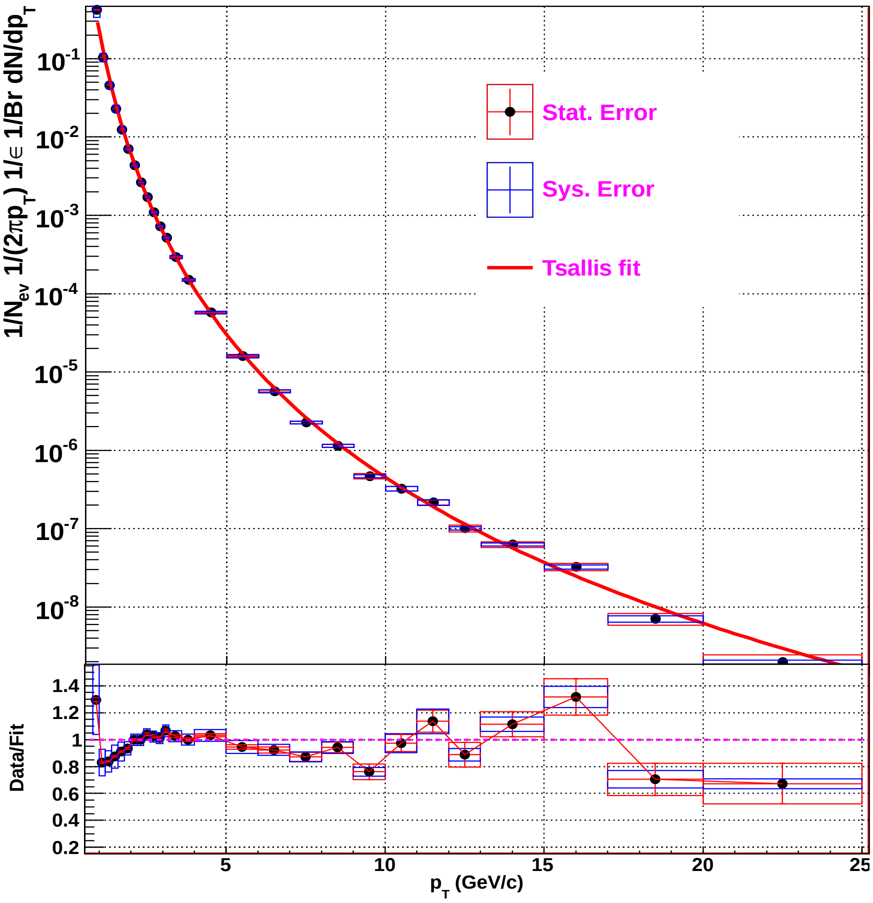

Figure 7.1: The π^0 production yield in pp collisions at 7 TeV measured with PHOS. The distribution is fitted by a Tsallis function.

The normalized production spectrum is converted to the invariant differential cross section $E\frac{d^3\sigma}{d\mathbf{p}^3}$ under the assumption of the pp cross section for the selected event samples by

$$E\frac{d^3\sigma}{d\mathbf{p}^3} = \sigma_{pp}^{inel} \cdot \frac{1}{N_{ev}} \frac{\Delta N}{2\pi p_T \Delta p_T \Delta y} \cdot \frac{1}{\epsilon_{Acc\times Rec}} \cdot \frac{1}{Br} \tag{7.8}$$

From the ALICE measurement, the cross section in pp collisions at 7 TeV is 67 ± 10 mb. The π^0 invariant cross section is shown in Fig. 7.2, compared by the NLO pQCD predictions.

Table 7.1: Fitting parameter of the π^0 production yield (Fig.7.2) in pp at 7 TeV. It also compared with the fitting results of mesons measured at RHIC in pp at 200 GeV. $d\sigma/dy$ are in μb for J/ψ and ψ, and in mb for all the other mesons.

type	$d\sigma/dy(mb,\mu b)$	$T(MeV)$	n=-1/(1-q)
π^0	135.869±123.185	49.32±22.57	6.325±0.233
π	42.8±3.1	112.6±2.1	9.57±0.1
K	4.23±0.09	125.4±0.9	9.81±0.13
η	3.86±0.30	124±2	9.84±0.14
ω	4.26±0.23	115.5±2.1	10.0±0.22
η	0.63±0.27	123±17	10.12±0.28
ϕ	0.427±0.019	123.4±3.0	10.16±0.31
J/ψ	0.76±0.014	148±8	11.5±1.1
ψ	0.132±0.029	147±127	11.9±1.3
p	1.775±0.044	58.5±1.8	9.2±0.28

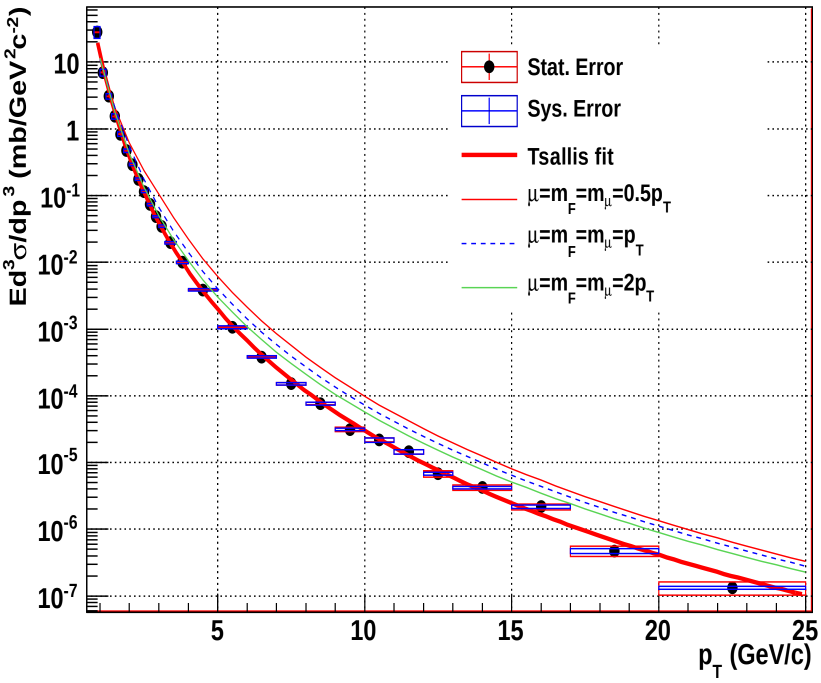

Figure 7.2: The π^0 invariant cross section measured in pp collisions at 7 TeV with PHOS.

7.2 Scaling behavior of m_T and x_T

m_T scaling

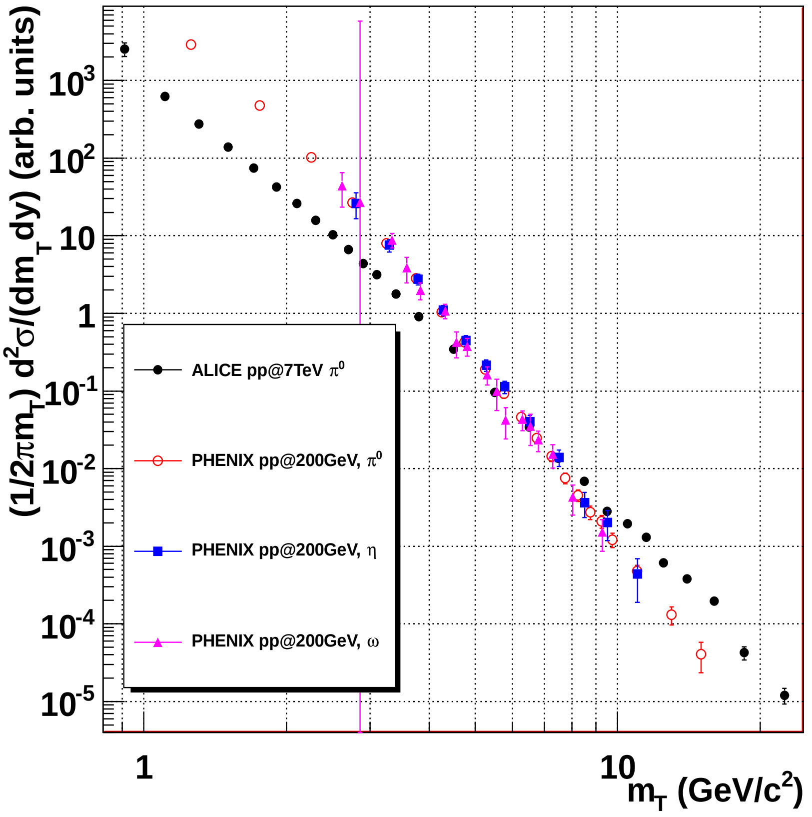

Figure 7.3: π^0 m_T distribution measured in ALICE with pp at 7 TeV(circle real point), and π^0, η and ω mesons measured in PHENIX with pp at 200 GeV. All the distributions are normalized to an arbitrary unit.

At ISR energies, for the different identified particle spectra, an universal parameterization has been found as an expression [151]:

$$E\frac{d^3\sigma}{dp^3} = A\frac{e^{-m_T/T}}{m_T^{\lambda}}. \tag{7.9}$$

Because of the exponential spectra shapes, it can describe the experimental data very well. From the observation of the temperature parameter, they are the same for different particles. Thus, so called m_T scaling refers the m_T distribution for different particles regardless of their mass have a similar slope.

Fig. 7.3 is the m_T distribution for neutral mesons π^0 measured in ALICE with pp collisions at 7 TeV, π^0, η and ω measured in PHENIX with pp collisions at 200

GeV. All the distribution are normalized to an arbitrary unit. From the PHENIX results for different particles, a similar shape is observed. In ALICE, more physics data points will be implemented soon after.

x_T scaling

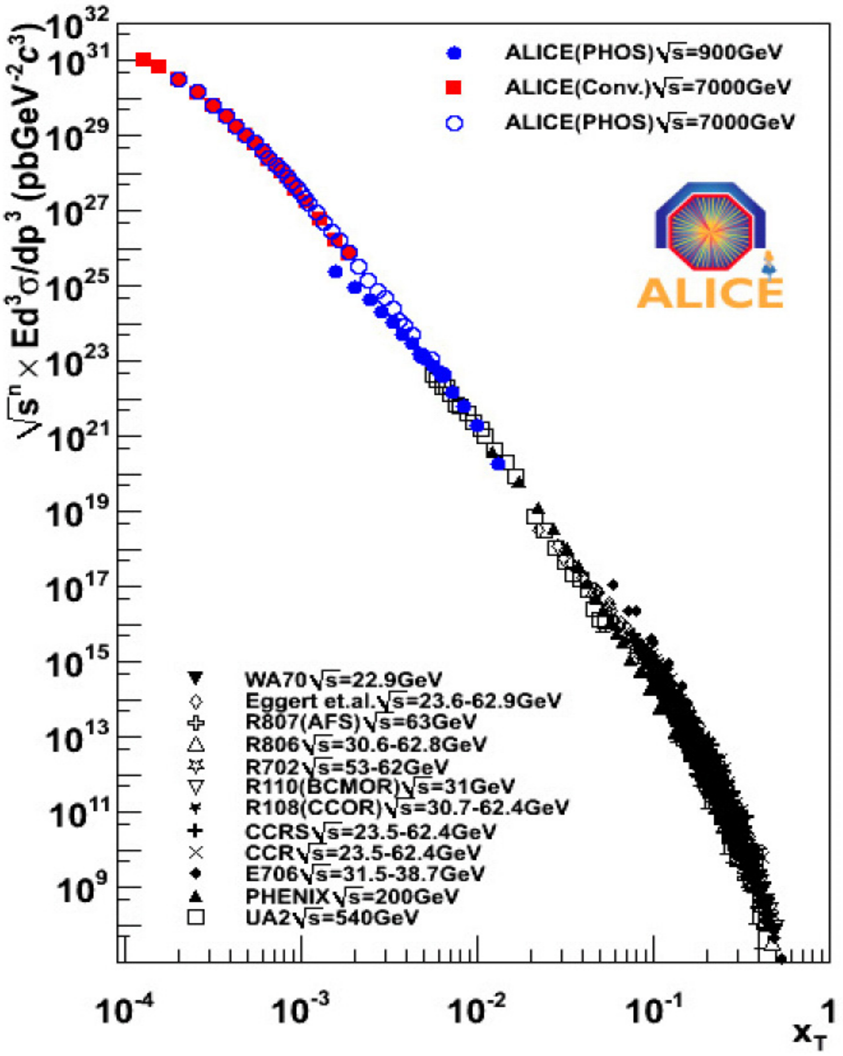

Figure 7.4: π^0 x_T distribution measured with ALICE in pp collisions at 7 *TeV*, compared with world-wide data (black). The parameter n is fixed with a value of 5.23±0.03

The x_T ($x_T = 2p_T/\sqrt{s}$) scaling has a form [152]

$$E\frac{d^3\sigma}{dp^3} = \frac{1}{\sqrt{s}^{n(x_T,\sqrt{s})}} G(x_T), \tag{7.10}$$

where $G(x)$ is scaling factor and $1/\sqrt{s}^n$ is dimensional factor and n gives the form of force-law between constituents. It describes the transverse momentum spectra dependence on the center-of-mass energy $\sqrt{s}$. At lower p_T, it is a soft physics region thus depends very little on $\sqrt{s}$. At higher p_T there is a power law tail which strongly depends on $\sqrt{s}$.

Fig. 7.4 shows the π^0 x_T distribution measured with ALICE in pp collisions at 7 TeV, compared with world-wide data (black). The parameter n is fixed with a value of 5.23±0.03. The results from ALICE can be well extended to very small x_T value region of 10^{-4} with a global similar shape.

7.3 Outlook

In this thesis, the strategy of the neutral mesons measurement have been studied. Followed by the first data-taking with ALICE at the LHC, we first understood our electromagnetic calorimeters and made them work. Based on the statistics collected in pp collisions at 7 TeV, π^0 can be measured with a p_T range from 0.6 GeV/c to 25 GeV/c. The η peaks from the invariant mass spectra have been clearly observed and the spectrum is expected to be extracted up to 15 GeV/c. The production yield is obtained for π^0 compared with theoretical NLO calculation. The result presents a $\sim$ 20% difference with NLO calculation. The π^0 spectrum scaling behavior of m_T and x_T are studied. Compared the x_T distribution from ALICE with the world existing data points, a similar shape is observed. This measurement is a baseline for the ongoing PbPb analysis to conclude the medium properties.

ALICE now has started the new production since March, 2011 and will continue the data-taking with pp and PbPb collisions till the end of 2012. More physics data will be collected with several $\sim 10^9$ min-bias events under the designed luminosity. Then ALICE PHOS and EMCAL will take the chance to get a fine calibration. As expected, the neutral mesons of π^0, η and ω are expected to be measured up to 45 GeV/c.

The initial study of detector performance and π^0 measurement are crucial for understanding the detectors and any other physics measurements, such as direct photon excess, γ-jet and π^0-jet measurement, flow measurement by photon probes etc. Combing all of these physics measurements, the understanding to the hot-dense matter created at LHC energies will be realized.

Finally, I would like to end the thesis by the below quota.

We experimentalists are not like theorists: the originality of an idea is not for being printed in a paper, but for being shown in the implementation of an original experiment.

Patrick M. S BLACKETT, London, 1962

Appendix

A. Acronyms

- **ACORDE**: ALICE COsmic Ra DEtector
- **Ads/CFT**: Anti-de-Sitter space/Conformal Field Theory
- **ALICE**: A Large Ion Collider Experiment
- **ALTRO**: ALICE TPC ReadOut
- **AOD**: Analysis Object Data
- **APD**: Avalanche Photon Diode
- **CPV**: Charged Particle Veto
- **CSP**: Charged Sensitive Preamplifier
- **CTP**: Central Trigger Processor
- **DAQ**: Data Acquisition
- **DATE**: ALICE Data Acquisition and Test Environment
- **DCA**: Distance Closest Approach
- **DCS**: Detector Control System
- **DDL**: Detector Data Link
- **ECS**: Experiment Control System
- **EM**: ElectroMagnetic
- **EMCAL**: ElectroMagnetic CALorimeter
- **ESD**: Event Summary Data
- **FEE**: Frond-End Electronics
- **GDC**: Global Data Concentrator

- **HMPID**: High Multiplicity Particle Identification Detector
- **ITS**: Inner Tracking System
- **LED**: Light-Emitting Diode
- **LHC**: Large Hadron Collider
- **LDC**: Local Data Concentrator
- **LQCD**: Lattice Quantum ChromoDynamics
- **LTU**: Local Trigger Unit
- **MIP**: Minimal Ionizing Particle
- **MRPC**: Multi-gap Resistive Plate Chamber
- **NLO**: Next Leading Order
- **QA**: Quality Assurance
- **QCD**: Quantum ChromoDynamics
- **QED**: Quantum ElectroDynamics
- **OCDB**: Offline Condition DataBase
- **PHOS**: PHoton Spectrameter
- **pQCD**: Perturbative QCD
- **PDS**: Permanent Data Storage
- **PMD**: Photon Multiplicity Detector
- **QFT**: Quantum Field Theory
- **QGP**: Quark Gluon Plasma
- **RCU**: Readout Control Unit
- **SDD**: Silicon Drift Detector
- **SPD**: Silicon Pixel Detector
- **SSD**: Silicon Strip detector
- **TOF**: Time Of Flight
- **TPC**: Time Projection Chamber

- **TRD**: Transition Radiation Detector
- **TRU**: Trigger Readout Unit
- **TTC**: Trigger, Timing and Concentrator system
- **ZDC**: Zero Degree Calorimeter

B. Final combined π^0 yield vs. p_T with PHOS

Table 7.2: The invariant cross section vs p_T with pp collisions at 7 TeV with PHOS.

p_T	Yield (mb/GeV^2c^{-2})	stat. error	%	sys. error.	%
0.9	28.1486	0.325213	1.16	5.59312	19.87
1.1	6.95378	0.0576756	0.83	0.826805	11.89
1.3	3.07302	0.021068	0.69	0.289171	9.41
1.5	1.53827	0.0101428	0.66	0.151827	9.87
1.7	0.831302	0.00576466	0.69	0.0635115	7.64
1.9	0.469664	0.00355749	0.76	0.0245634	5.23
2.1	0.291046	0.00225311	0.77	0.0123986	4.26
2.3	0.175935	0.00151725	0.86	0.00744205	4.23
2.5	0.115004	0.001051	0.91	0.00463465	4.03
2.7	0.0734154	0.00078019	1.06	0.00299535	4.08
2.9	0.0483778	0.000567492	1.17	0.00199317	4.12
3.1	0.0347874	0.000437849	1.26	0.00143324	4.12
3.4	0.019674	0.000203105	1.03	0.000798762	4.06
3.8	0.0100425	0.000131649	1.31	0.000410737	4.09
4.5	0.00384113	4.17065e-05	1.09	0.000161712	4.21
5.5	0.00106768	1.91619e-05	1.79	5.41312e-05	5.07
6.5	0.00038181	9.3855e-06	2.46	1.67614e-05	4.39
7.5	0.000151568	5.74909e-06	3.79	6.50228e-06	4.29
8.5	7.64368e-05	3.20205e-06	4.19	3.50845e-06	4.59
9.5	3.13336e-05	2.39474e-06	7.65	1.34108e-06	4.28
10.5	2.1707e-05	1.43321e-06	6.60	1.56291e-06	7.20
11.5	1.44755e-05	1.04951e-06	7.25	1.16673e-06	8.06
12.5	6.76235e-06	6.97634e-07	10.32	3.50966e-07	5.19
14	4.21369e-06	3.55767e-07	8.44	2.01414e-07	4.78
16	2.17922e-06	2.24271e-07	10.29	1.30099e-07	5.97
18.5	4.72792e-07	8.02698e-08	16.98	4.3686e-08	9.24
22.5	1.33307e-07	2.99575e-08	22.47	7.3452e-09	5.51

C. Invariant mass distribution with EMCAL

The 2γ invariant mass distribution for EMCAL in pp collisions at 7 TeV is presented. The mix event procedure is used to subtract the background.

Real/Mix

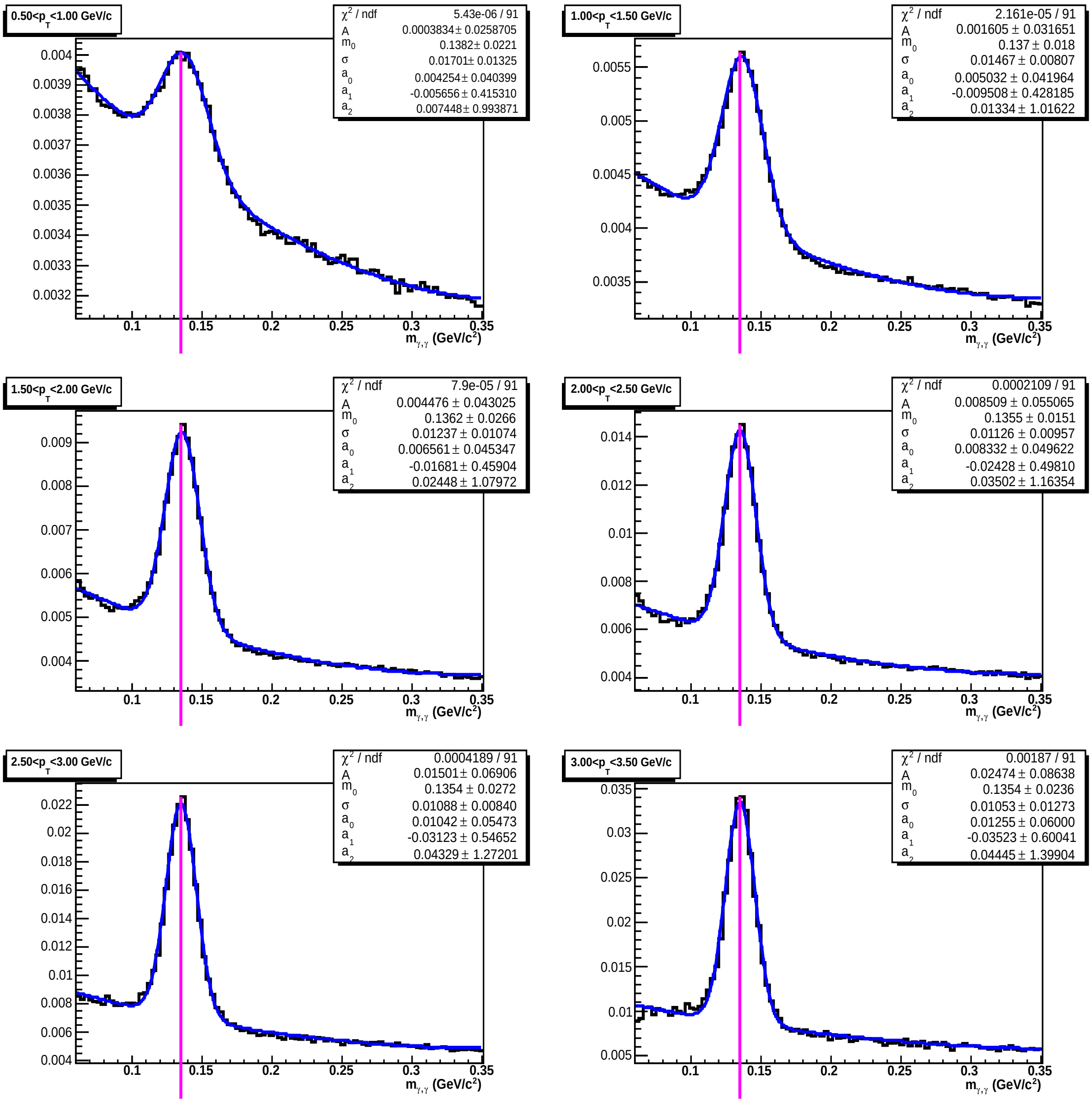

Figure 7.5: EMCAL, in pp collisions at 7 TeV: Real/Mix at $0.5 < p_T < 3.5$ GeV/c fitted by a Gaussian and polynomial function.

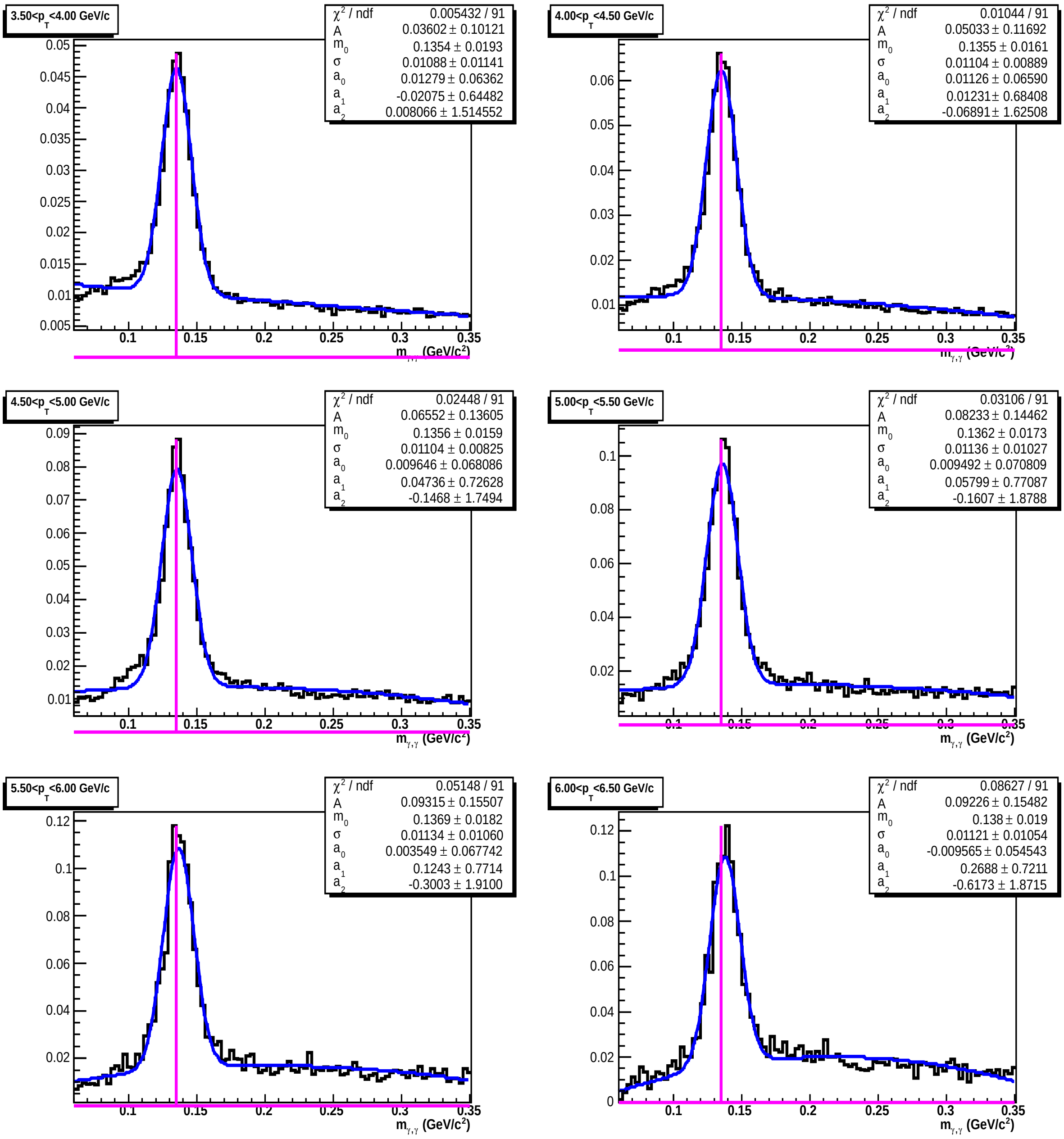

Figure 7.6: EMCAL, in pp collisions at 7 TeV: Real/Mix at $3.5 < p_T < 6.5$ GeV/c fitted by a Gaussian and polynomial function.

Real and normalized combinatorial background

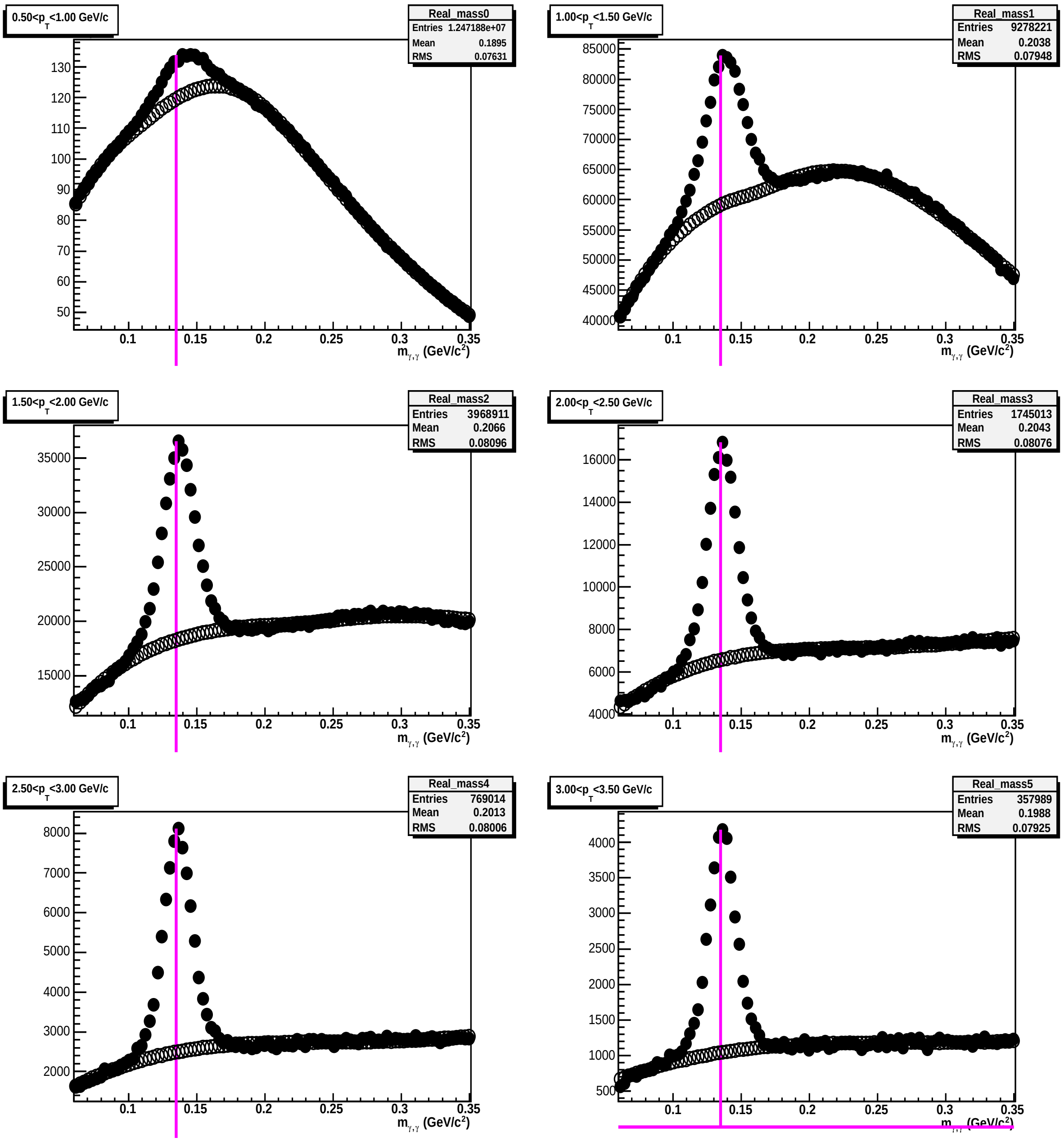

Figure 7.7: EMCAL, in pp collisions at 7 TeV: Real and normalized background distributions at $0.5 < p_T < 3.5\ GeV/c$ fitted by a Gaussian and polynomial function.

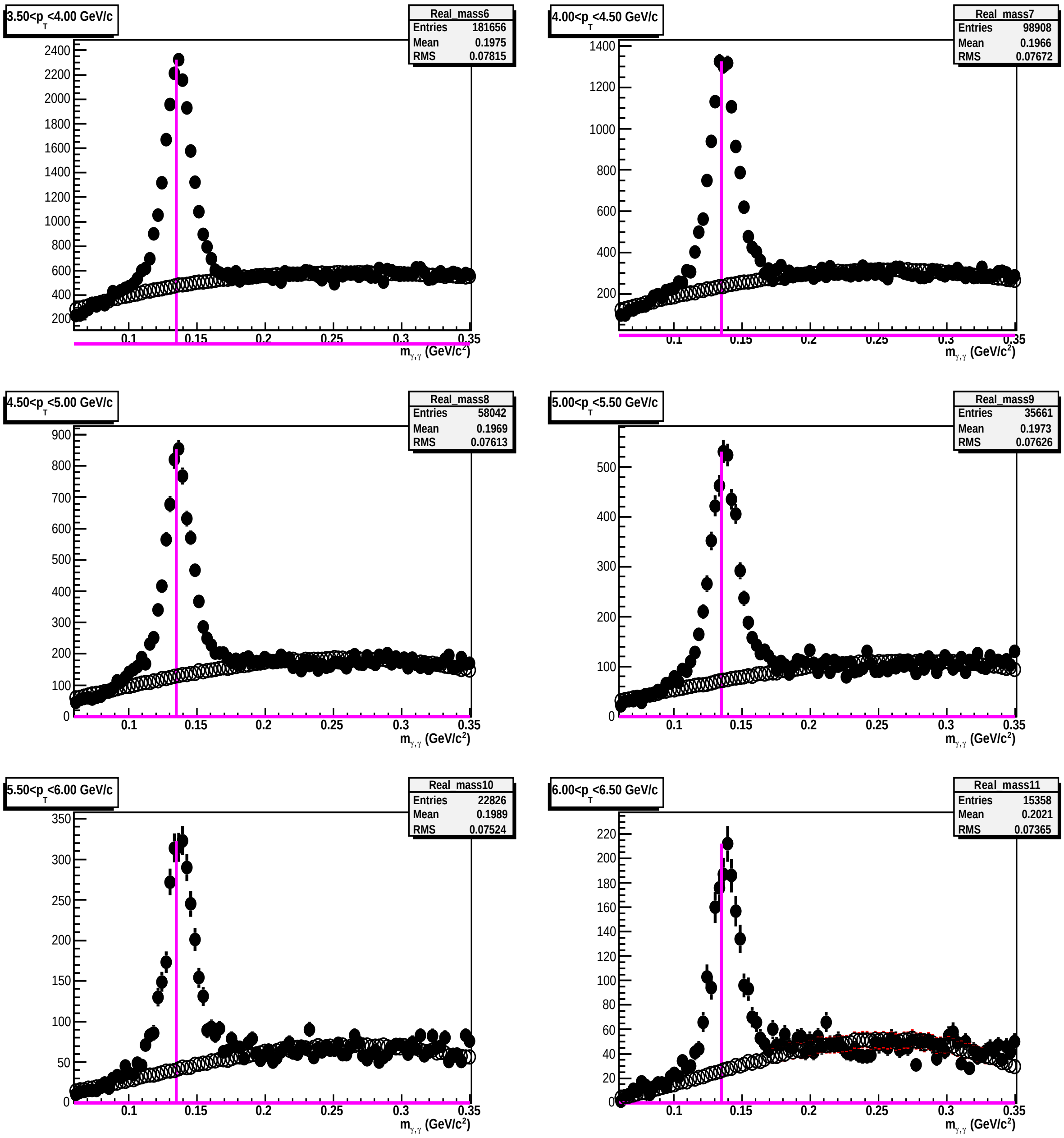

Figure 7.8: EMCAL, in pp collisions at 7 TeV: Real and normalized background distributions at $3.5 < p_T < 6.5$ GeV/c fitted by a Gaussian and polynomial function.

Signal after the background subtraction

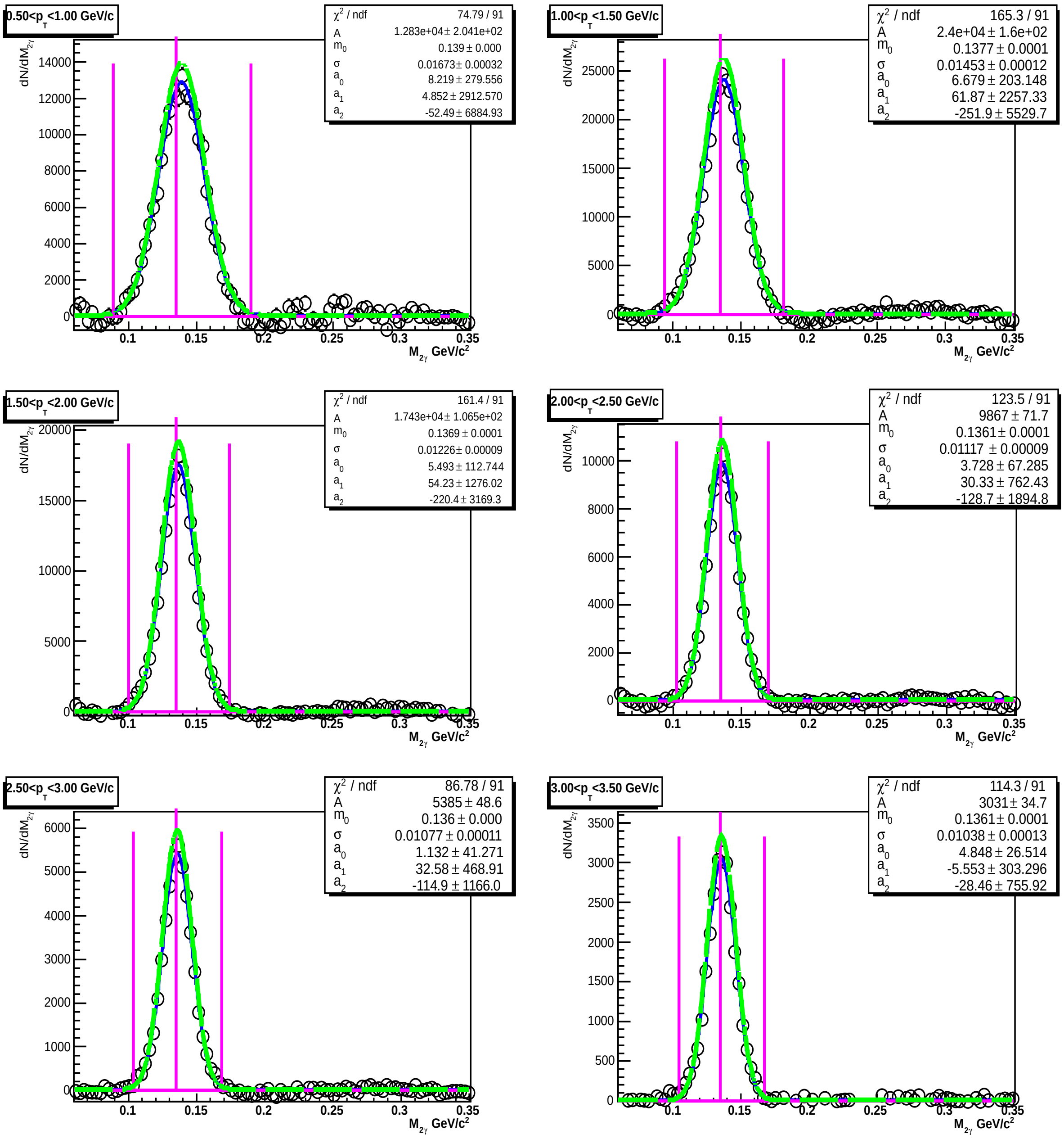

Figure 7.9: EMCAL, in pp collisions at 7 TeV: Signals after the background subtraction at $0.5 < p_T < 3.5\ GeV/c$ fitted by a Gaussian and polynomial function.

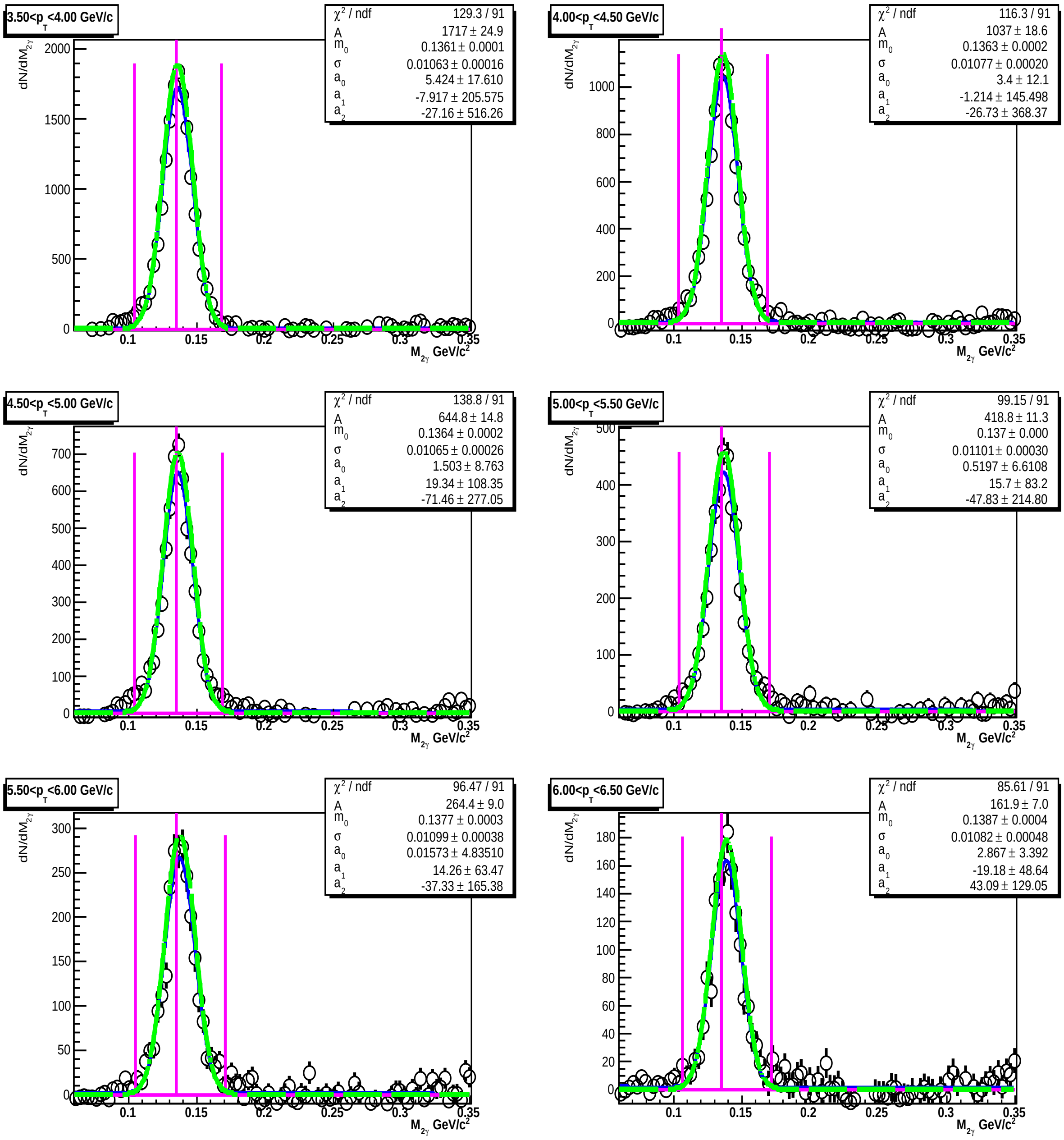

Figure 7.10: EMCAL, in pp collisions at 7 TeV: Signals after the background subtraction at $3.5 < p_T < 6.5$ GeV/c fitted by a Gaussian and polynomial function.

Acknowledgment

I would like to thank lots of people during the past three years of my doctoral study in IOPP/CCNU, China and IPHC-UdS, France. Thanks for the fund support from CSC and FCPPL, which grant me to be a co-joint PhD student between the two affiliates (CCNU and UDS).

I specially thank both of my supervisors, Prof. ZHOU Daicui, ROY Christelle and SCHUTZ Yves, for their guidance and support on my physics analysis and activities. Their wisdom, human touch and international horizon explain me the spirit of collaboration and competition, which have been of great impact on my research and personality. It's self-evidence that Prof. ZHOU shows great energy and enthusiasm in ALICE experiment since 1990's and set us a super example for me in pursuing a career.

During the writing and review of my thesis, I had discussions with C. D. Zaida and got lots of comments from her although the busy season of ALICE data analysis. I also got the helps from C. B. Gustavo, KHARLOV Yuri and other ALICE PHOS and EMCAL colleagues. I would like to say thank you sincerely.

I thank Prof. CAI Xu, Prof. YANG Yadong, Prof. WANG Enke, Prof. LIU Feng, et al from IOPP for providing us a strong academic atmosphere and their teaching. I thank IPHC ALICE colleagues KUHN Christian, HIPPOLYTE Boris, BELIKOV Yuri and MARIE Antonin for their enthusiastic helps during my stay in France, as well as the Chinese friends in France, WANG Jia, WEI Xiaomin, ZHANG Ying et al. It's pleasure to work with Dr. YIN Zhongbao and Dr. WANG Yaping, ALICE-Wuhan-group members YUAN Xianbao, WANG Dong, WANG Mengliang, ZHU Xiangrong, ZHOU Fengchu, ZHANG Xiaoming, ZHU Jianlin, ZHANG Fan and MAO Yaxian etc., as well as my friends ZHENG Hua, GUO Long, CHEN Jiayun, LI Hanlin et al.

I would like to express my great appreciations to my father, mother and my elder sister, for their understanding and support in my "LONG-MARCH" towards the PhD. Finally, I thank my wife Dr. YANG Fan. We share the joy and painful experience for a long term from the master to doctor. It's the true love to hold us together to be a "Doctor couples".

WAN Renzhuo
Strasbourg, France
March 20, 2011

List of Publications

- **Daicui ZHOU, Renzhuo WAN**, Yaxian MAO, Zhongbao YIN, Chuncheng Xu, Nanshan YU, Xu CAI *Atomic energy science and technology 42* (7) 2008: 655-657
- **Renzhuo WAN**, Daicui ZHOU, Zhongbao YIN, *China Physics C* **32** (08) 2008 620-623
- **Renzhuo WAN**, Daicui ZHOU, Zhongbao YIN, *ALICE-INT* 2008-017
- Wenchang XIANG, **Renzhuo WAN**, Daicui ZHOU, *China Physics Letter*, *25* (11) 2008: 3912
- Wenchang XIANG, Daicui ZHOU, **Renzhuo WAN**, Xianbao YUAN, *China Physics C* , *33* (02) 2009
- **Renzhuo WAN**, Daicui ZHOU, Zhongbao YIN, *QM2008*
- Daicui ZHOU, Yaxian MAO, **Renzhuo WAN**, Y. SCHUTZ, Z. B. YIN, Y. P. WANG, K. MA, X. CAI, G. Conesa, Y. KHARLOV *Nuclear Physics A* , *834* 2010: 291
- **Daicui ZHOU, Renzhuo WAN** , Yaxian MAO, Y. Schutz, M. L. WANG, K. MA, Y. P. WANG, Z. B. YIN, X. CAI, Y. Kharlov, G. Conesa, C. ROY *China Physics C* , *34* (09) 2010
- Yuri KHARLOV, Lamia BENHABIB, **Renzhuo WAN** , *POS*, *089* 2008LHC
- **Renzhuo WAN**, *JPCS*, calor2010, 2010
- **Renzhuo WAN**, *J. Phys.: Conf. Ser. 270 (2011) 012004*
- D. Aleksandrov, ..., **Renzhuo WAN** et. al, for ALICE-PHOS collaboration, *Nuclear Instruments and Methods in Physics Research A*, *620* 2010: 526-533
- K. Aamodt, ..., **Renzhuo WAN**, ..., et. al, for ALICE collaboration, *Eur. Phys. J. C* **65** 2010: 111
- K. Aamodt, ..., **Renzhuo WAN**, ..., et. al, for ALICE collaboration, *Eur. Phys. J. C* **68** 2010: 89

- K. Aamodt, ..., **Renzhuo WAN**, ..., et. al, for ALICE collaboration, *Eur. Phys. J. C* **68** 2010: 345
- K. Aamodt, ..., **Renzhuo WAN**, ..., et. al, for ALICE collaboration, *Phys. Rev. Lett.* **105** No. 7 (2010)
- K. Aamodt, ..., **Renzhuo WAN**, ..., et. al, for ALICE collaboration, *Phys. Rev. D* **82** 052001 2010
- K. Aamodt, ..., **Renzhuo WAN**, ..., et. al, for ALICE collaboration, *Phys. Lett. B* **693** 2010: 53-68
- K. Aamodt, ..., **Renzhuo WAN**,..., et. al, for ALICE collaboration, *Phys. Rev. Lett.* **105** 252302 (2010)
- K. Aamodt, ..., **Renzhuo WAN**,..., et. al, for ALICE collaboration, *Phys. Rev. Lett.* **106** 032301 (2011)
- K. Aamodt, ..., **Renzhuo WAN**,..., et. al, for ALICE collaboration, *Phys.Lett. B* **696** 2011: 328-337
- K. Aamodt, ..., **Renzhuo WAN**, ..., et. al, for ALICE collaboration, *Eur. Phys. J. C* **71** 2011: 1594

Activities

1) Workshop on Photon and jet with ALICE. Dec. 4-6, 2008, Wuhan, China. An oral talk on "Neutal mesons measurement with ALICE PHOS"
2) The 2^{nd} FCPPL workshop, March 21-24, 2009. Wuhan, China
3) NN2009, August 16-21, 2009. Beijing, China
4) QNP2009, Sep. 21-26. Beijing, China
5) The 3^{rd} FCPPL workshop, April 7-9. Lyon, France. An oral talk on "First results from pp 900 GeV in ALICE with EM-Calorimeters"
6) The XIV International Conference on Calorimetry in High Energy Physics (Calor 2010). Beijing, China. May 10 - 14, 2010. An oral talk on "From raw data to physics results with ALICE PHOS"
7) Hot quark 2010. La Londe les Maures, France. June 21 - 26, 2010. An oral talk on "π^0 measurement with ALICE EM-calorimeters"
8) ALICE shifts on DAQ, CTP, DCS, PHOS and offline
9) QM2011 poster on "Studies of $\omega(782) \rightarrow \pi^0\gamma$ in pp collisions at $\sqrt{s_{NN}} = 7\ TeV$ with ALICE electromagnetic calorimeters"

Bibliography

[1] L. Bergstrom and A. Goobar: *Cosmology and particle physics*, ISBN:3-350-43128-4 (2004)

[2] D. H. Perkins: *Particle Astrophysics*, ISBN:0-19-850951-0 (2003)

[3] B. R. Martin: *Nuclear and particle physics*, ISBN: 0-470-01999-9 (2006)

[4] Stephen W. Hawking: *Hawking on the big bang and black holes*, New York, University of Cambridge, 2001

[5] J. Chadwick: *Possible existence of a neutron*, Nature **129** (1932) 312

[6] J. W. Harris, B. Muller: *The search for the quark-gluon plasma*, Annu. Rev. Nucl. Par. Sci. **46** (1996) 71

[7] B. Muller: *The physics of the Quark-Gluon-Plasma*, Lecture Notes in Physics, Vol. **225**, Springer, Heidelberg (1985)

[8] C. Y. Wong: *Introduction of high energy heavy ion collisions*, World Scientific, Singapore (1944)

[9] L. McLerran: *The physics of the Quark-Gluon-Plasma*, Rev. Mod. Phys. **58** 1012 (1986) 24

[10] G. Dissertori, I. Knowles, and M. Schmelling: *Quantum Chromodynamics - High Energy Experiments and Theory*, Oxford Universidy Press (2003)

[11] D. J. Gross and F. Wilczek: *Ultraviolet behavior of non-abelian gauge theories*, Phys. Rev. Lett., **30** (1973)1343

[12] D. J. Gross: *Twenty five years of asymptotic freedom*, Nucl. Phys. B., **74** (1999) 426

[13] F. Karsch, E. Laermann: *The Pressure in 2, 2+1 and 3 Flavour QCD* , A. Peikert. Phys. Lett. B **478** (2000) 447

[14] J. Engels et al.: *The onset of deconfinement in SU(2) lattice gauge theory*, Z. Phys. C **42** (1989) 341

[15] V. Goloviznin and H. Satz: *The refractive properties of the gluon plasma in SU(2) gauge theory*, Z. Phys. C **57** (1993) 671

[16] F. Karsch: *Lattice Results on QCD Thermodynamics*, Nucl. Phys. A **698** (2002) 199c

[17] S. Gupta, X. F. Luo, B. Mohanty, H. G. Ritter, N. Xu: *Scale for the Phase Diagram of Quantum Chrmodynamics*, Science **332** no. 6037 (2011) 1525

[18] A. Gray et al.: *Υ spectrum and m_b from full lattice QCD*, Phys. Rev. D**72**, 094507 (2005)

[19] STAR collaboration:*An Experimental Exploration of the QCD Phase Diagram: The Search for the Critical Point and the Onset of De-confinement*, arXiv:1007. 2613

[20] M. Gyulassy, L. McLerran: *New Forms of QCD Matter Discovered at RHIC*, Nucl. Phys. A **750** (2005) 30

[21] B. Muller: *From Quark-Gluon Plasma to the Perfect Liquid*, Acta Phys. Polon. B**38** (2007) 3705

[22] T. Hirano: *Hydrodynamic approaches to relativistic heavy ion collisions*, ACTA PHYSICA POLONICA B, vol. **36** (2005)

[23] S. A. Bass et. al.: *Signatures of quark-gluon plasma formation in high energy heavy-ion collisions: a critical review*, J. Phys. G: Nucl. Part. Phys. **25** (1999)

[24] X. N. Wang and M. Gyulassy: *Gluon Shadowing and Jet Quenching in A+A Collisions at $\sqrt{s}$ = 200 GeV*, Phys. Rev. Lett. **68** (1992) 1480

[25] PHENIX Collaboration: *Suppression pattern of π^0 at high transverse momentum in Au+Au collisions at $\sqrt{s}_{NN}$ = 200 GeV and constraints on medium transport coefficients*, Phys. Rev. Lett. **101**, 232301 (2008)

[26] PHENIX Collaboration: *High transverse momentum η production in p+p, d+Au, and Au+Au collisions at $\sqrt{s}_{NN}$=200 GeV*, Phys. Rev. C **75**, 024909 (2007)

[27] PHENIX Collaboration: *Suppression of Hadrons with Large Transverse Momentum in Central Au+Au Collisions at $\sqrt{s}$ = 130 GeV*, Phys. Rev. Lett. **88**, 022301 (2002)

[28] M. Miller, K. Reygers, S. Sanders and P. Steinberg: *Glauber Modeling in High-Energy Nuclear Collisions*, Ann. Rev. Nucl. Part. Sci. **57** (2007) 205

[29] PHENIX Collaboration: Quark Matter 2009

[30] K. Aamodt, ..., **Renzhuo WAN**..., (ALICE collaboration): *Suppression of Charged Particle Production at Large Transverse Momentum in Central Pb-Pb Collisions at* $\sqrt{s}_{NN} = 2.76\ TeV$, Phys. Lett. B **696** (2011) 30

[31] STAR collaboration: *Azimuthal di-hadron correlations in d+Au and Au+Au collisions at* $\sqrt{s}_{NN} = 200\ GeV$ *from STAR*, arxiv:1004.2377

[32] STAR collaboration: *Jet properties from dihadron correlations in p+p collisions at* $\sqrt{s} = 200\ GeV$, Phys. Rev. D **74**, 072002 (2006)

[33] STAR collaboration: *Jet structure from dihadron correlations in d+Au collisions at* $\sqrt{s} = 200\ GeV$, Phys. Rev. C **73**, 054903 (2006)

[34] PHENIX collaboration: *Dihadron azimuthal correlations in Au+Au collisions at* $\sqrt{s}_{NN} = 200\ GeV$, Phys. Rev. C **78**, 014901

[35] T. Renk, J. Ruppert: *Mach cones in an evolving medium*, Phys. Rev. C **73**, 011901

[36] V. Koch, A. Majumder, X. N. Wang: *Cherenkov Radiation from Jets in Heavy-Ion Collisions*, Phys. Rev. Lett **96**, 172302

[37] I. Vitev: *Large Angle Hadron Correlations from Medium-Induced Gluon Radiation.* PLB **630**, 78 (2005); A. D. Plolosa et al.: *Jet shapes in opaque media*, Phys. Rev. C **75**, 041901

[38] Armesto: *Low-*p_T *collective flow induces high-*p_T *jet quenching*, Phys. Rev C **72**, 064910; Charles B Chiu, et al.: *Proton-*Λ *correlations in central Au+Au collisions at* $\sqrt{s}_{NN} = 200\ GeV$, Phys. Rev. C **74**, 064909

[39] Hanzhong Zhang, J. F. Owens, Enke Wang, and Xin-Nian Wang: *Tomography of High-Energy Nuclear Collisions with Photon-Hadron Correlations*, Phys. Rev. Lett. **103**, 032302 (2009)

[40] PHENIX Collaboration: *Photon-hadron jet correlations in p+p and Au+Au collisions at* $\sqrt{s}_{NN}$*=200* GeV, Phys. Rev. C **80**, 024908 (2009)

[41] R. Baier, Y. L. Dokshitzer, A. H. Muller, S. Peigne and D. Schiff: *Radiative energy loss of high energy quarks and gluons in a finite-volume quark-gluon plasma*, Nucl. Phys. B **483** (1997) 291

[42] R. Baier, Y. L. Dokshitzer, A. H. Muller, S. Peigne and D. Schiff: *Radiative energy loss and* p_T*-broadening of high energy partons in nuclei*, Nucl. Phys. B **484** (1997)265

[43] R. Baier, Y. L. Dokshitzer, A. H. Muller and D. Schiff: . Phys. Rev. C **58** (1998) 1706

[44] R. Baier, Y. L. Dokshitzer, A. H. Muller and D. Schiff: *Medium-induced radiative energy loss: equivalence between the BDMPS and Zakharov formalisms*, Nucl. Phys. B **531** (1998) 403

[45] B. G. Zakharov: *Fully quantum treatment of the Landau-Pomeranchik-Migdal effect in QED and QCD*, JETP Lett. **63**, 952 (1996) 299

[46] N. Armesto, C. A. Salgado and U. A. Wiedemann: *Medium-induced gluon radiation off massive quarks fills the dead cone.* Phys. Rev. D **69** (2004) 114003

[47] U. A. Wiedemann: *Jet quenching versus jet enhancement: a quantitative study of the BDMPS-Z gluon radiation spectrum*, Nucl. Phys. A 690 (2001) 731

[48] C. A. Salgado and U. A. Wiedemann: *Calculating quenching weights*, Phys. Rev. D **68** 014008 (2003)

[49] U. A. Wiedemann: *Gluon radiation off hard quarks in a nuclear environment: opacity expansion*, Nucl. Phys. B **588**, 303 (2000)

[50] M. Gyulassy, P. Levai and I. Vitev: *Non-Abelian Energy Loss at Finite Opacity*, Phys. Rev. Lett. **85**, 5535 (2000)

[51] M. Gyulassy, P. Levai and I. Vitev: *Reaction operator approach to non-abelian energy loss*, Nucl. Phys. B **594**, 371 (2001)

[52] M. Gyulassy, P. Levai and I. Vitev: *Jet Tomography of Au+Au Reactions Including Multi-gluon Fluctuations* , Phys. Lett. B **538**, 282 (2002)

[53] M. Gyulassy and X. N. Wang: *Multiple collisions and induced gluon bremsstrahlung in QCD*, Nucl. Phys. B **420**, 583 (1994)

[54] M. Gyulassy, P. Levai and I. Vitev: *Jet quenching in thin quark-gluon plasmas I: formalism*, Nucl. Phys. B **571**, 197 (2000)

[55] X. F. Guo and X. N. Wang: *Multiple Scattering, Parton Energy Loss, and Modified Fragmentation Functions in Deeply Inelastic eA Scattering*, Phys. Rev. Lett. **85**, 3591 (2000)

[56] X. N. Wang and X. F. Guo: *Multiple parton scattering in nuclei: parton energy loss*, Nucl. Phys. A **696**, 788 (2001)

[57] B. W. Zhang and X. N. Wang: *Multiple parton scattering in nuclei: beyond helicity amplitude approximation*, Nucl. Phys. A **720**, 429 (2003)

[58] M. Luo, J. W. Qiu and G. Sterman: *Anomalous nuclear enhancement in deeply inelastic scattering and photoproduction*, Phys. Rev. D **50**, 1951 (1994)

[59] P. Arnold, G. D. Moore and L. G. Yaffe: *Photon Emission from Quark-Gluon Plasma: Complete Leading Order Results* , JHEP **0112**, 009 (2001)

[60] P. Arnold, G. D. Moore and L. G. Yaffe: *Photon and Gluon Emission in Relativistic Plasmas*, JHEP**0206**, 030 (2002)

[61] P. Arnold, G. D. Moore and L. G. Yaffe: *Photon Emission from Ultra-relativistic Plasmas* , JHEP **0111**, 057 (2001)

[62] S. Turbide, C. Gale, S. Jeon and G. D. Moore: *Energy loss of leading hadrons and direct photon production in evolving quark-gluon plasma*, Phys. Rev. C **72**, 014906 (2005)

[63] K. Reygens: *Direct-photon production in heavy-ion collisions from SPS to RHIC energies*, Eur. Phys. J. C (2005)

[64] M. M. Aggarwal et al.: *Direct Photon Production in 158A GeV*^{208}*Pb*+^{208}*Pb Collisions*, nucl-ex/0006007 v2

[65] F. Arleo et al.: *Photon Physics in Heavy Ion Collisions at the LHC*, hep-ph/0311131

[66] Paul Stankus: *Direct photon productoin in relativistic heavy-ion collisions*, Anuu. Rev. Nucl. Part. Sci. **55** (2005)

[67] Thomas Peitzmann, Markus H: *Direct photons from Relativistic Heavy-ion Collisions*, Phys. Rept. **364** (2002) 175-246

[68] S. Voloshin and Y. Zhang: *Flow study in relativistic nuclear collisions by Fourier expansion of azimuthal particle distributions*, Z. Phys. C **70** (1996) 665

[69] PHENIX Collaboration: *Systematic studies of elliptic flow measurements in Au+Au collisions at* $\sqrt{s}_{NN} = 200\ GeV$, Phys. Rev. C **80**, 024909 (2009)

[70] R. S. Bhalerao, N. Borghini and J. Y. Ollitrault: *Analysis of anisotropic flow with Lee-Yang zeroes*, Nucl. Phys. A**727** (2003) 373 or nucl-th/0310016

[71] R. S. Bhalerao, N. Borghini and J. Y. Ollitrault: *Genuine collective flow from Lee-Yang zeroes*, Phys. Lett. B**580** (2004) 157-162 or nucl-th/0307018

[72] R. S. Bhalerao: *Anisotropic flow from Lee-Yang zeroes: a practical guide*, J. Phys. G**30** (2004)

[73] A. M. Poskanzer and S. A. Voloshin: *Methods for analyzing anisotropic flow in relativistic nuclear collisions*, Phys. Rev. C **58**, 1671 (1998)

[74] N. Borghimi, P. M. Dinh and J. Y. Ollitraul: *Flow analysis from multiparticle azimuthal correlations*, Phys. Rev. C **64**, 054901(2001)

[75] STAR collaboration: *Experimental and Theoretical Challenges in the Search for the Quark Gluon Plasma: The STAR Collaboration's Critical Assessment of the Evidence from RHIC Collisions*, Nucl. Phys. A **757** (2005) 102

[76] G. Kestin, U. W. Heinz: *Hydrodynamic radial and elliptic flow in heavy-ion collisions from AGS to LHC energies*, Eur. Phys. J. C **61**, 545 (2009)

[77] D. Teaney: *Effect of shear viscosity on spectra, elliptic flow, and Hanbury Brown Twiss radii*, Phys. Rev. C **68**, 034913 (2003)

[78] H. Masui, J. Y. Ollitrault, R. Snellings and A. Tang: *The centrality dependence of v_2/ϵ: the ideal hydro limit and η/s*, Nucl. Phys. A **830**, 463c (2009)

[79] K. Aamodt, ..., **Renzhuo WAN**..., (ALICE collaboration): *Elliptic Flow of Charged Particles in Pb-Pb Collisions at $\sqrt{s}_{NN} = 2.76$ TeV*, Phys. Rev. Lett. **105**, 252302 (2010)

[80] PHENIX Collaboration: *Measurement of the Λ and $\bar{\Lambda}$ particles in Au+Au Collisions at $\sqrt{s}_{NN} = 130$ GeV*, Phys. Rev. Lett. **89**, 092302 (2002)

[81] K. Adams, ..., **Renzhuo WAN**, ... et al, (ALICE collaboration): *Strange particle production in proton-proton collisions at $\sqrt{s} = 0.9$ TeV with ALICE at the LHC*, arXiv: 1012. 3257

[82] T. Matsui and H. Satz: *J/ψ suppression by quark-gluon plasma formation*, Phys. Lett. B **178**, 416 (1986)

[83] PHENIX Collaboration: *Cold Nuclear Matter Effects on J/ψ Yields as a Function of Rapidity and Nuclear Geometry in Deuteron-Gold Collisions at $\sqrt{s}_{NN} = 200$ GeV*, arXiv: 1010.1246

[84] P. Aurenche, J. P. Guille, E. Pilon and M. Werle: *Recent critical study of photon production in hadronic collisions*, Phys. Rev. D **73**, 094007 (2006)

[85] P. Aurenche, M. Fontannaz, J. P. Guille, B. Kniehl, E. Pilon and M. Werlen: *A Critical phenomenological study of inclusive photon production in hadronic collisions*, Eur. Phys. J. C **9** (1999) 107-119

[86] S. Catani, M. Fontannaz, J. P. Guillet and E. Pilon: *Cross section of isolated prompt photons in hadron-hadron collisions*, JHEP**05** (2002) 028

[87] J. Pumplin, D. R. Stump, J. Huston, H. L. Lai, P. Nadolsky and W.K. Tung: *New Generation of Parton Distributions with Uncertainties from Global QCD Analysis*, JHEP **0207**, (2002) 012

[88] H. A.Weldon: *Simple rules for discontinuities in finite-temperature field theory*, Phys. Rev. D**28**, 2007 (1983)

[89] C. Gale, J. I. Kapusta: *Vector dominance model at finite temperature*, Nucl. Phys. B**357**, 65 (1991)

[90] J. Kapusta, P. Lichard and D. Seibert: *High-energy photons from quark-gluon plasma versus hot hadronic gas*, Phys. Rev. D **44** (1991) 2774-2788 and Phys. Rev. D **47** (1993) 4171

[91] R. D. Pisarski: *Scattering amplitudes in hot gauge theories*, Phys. Rev. Lett. **63** (1989) 1129

[92] E. Braatern and R. D. Pisarski: *Soft amplitudes in hot gauge theories*, A general analysis. Nucl. Phys. B **337** (1990) 569

[93] R. J. Fries, B. Muller and D. K. Srivastava:*High-energy photons from passage of jets through Quark-Gluon Plasma*, Phys. Rev. Lett. **90**, 132301 (2003)

[94] S. Turbide, C. Gale, S. Jeon and G. D. Moore: *Energy loss of leading hadrons and direct photon production in evolving quark-gluon plasma*, Phys. Rev. C **72**, 014906 (2005) 233

[95] K. Nakamura et al. (Particle Data Group): J. Phys. G **37**, 075021 (2010)

[96] M. Aversa, P. Chiappetta, M. Greco and J.-Ph. Guillet: *QCD corrections to parton-parton scattering processes*, Nucl. Phys. B**327**, 105 (1989)

[97] P. Chiappetta, M. Greco, J.P. Guillet, S. Rolli and M. Werlen: *Next-to-leading order determination of pion fragmentation functions*, Nucl. Phys. B**412**, 3 (1994).

[98] P. Aurenche, P. Chiappetta, M. Fontannaz, J.-Ph. Guillet and E. Pilon: *Next to leading order bremsstrahlung contribution to prompt-photon production*, Nucl. Phys.B**399**, 34 (1993).

[99] A. Majumder, M. van Leeuwen: *The theory and phenomenology of perturbative QCD based jet quenching*, arXiv:1002.2206

[100] ALICE Collaboration: *The ALICE Experiment at the CERN LHC*, J. Instrum. **3**. S08002 (2008)

[101] ATLAS Collaboration: *The ATLAS Experiment at the CERN LHC*, J. Instrum. 3. S08003 (2008)

[102] CMS Collaboration: *The CMS Experiment at the CERN LHC*, J. Instrum. 3. S08004 (2008)

[103] LHCb Collaboration: *The LHCb Experiment at the CERN LHC*, J. Instrum. 3. S08001 (2008)

[104] $http://alimonitor.cern.ch/map.jsp$

[105] ALICE Collaboration: *Technical Design Report of the Inner Tracking System*, CERN/LHCC 99-12

[106] ALICE Collaboration: *Technical Design Report of the Time Projection Chamber*, CERN/LHCC 2000-001

[107] ALICE Collaboration: *Technical Design Report of the Transition Radiation Detector*, CERN/LHCC 2001-021

[108] ALICE Collaboration: *Technical Design Report of the Photon Spectrometer (PHOS)*, CERN/LHCC 99-4

[109] ALICE Collaboration:*ALICE Technical Proposal of EMCal*, CERN-LHCC-2006-014

[110] ALICE Collaboration: *Technical Design Report of the MUON spectrometer*, CERN/LHCC 99-22 and 2000-046

[111] ALICE Collaboration: *Technical Design Report of the Forward Detectors*, CERN/LHCC 2004-025

[112] ALICE Collaboration: *Technical Design Report of the Photon Multiplicity Detector*, CERN/LHCC 99-32

[113] ALICE Collaboration: *Technical Design Report of the Zero Degree Calorimter*, CERN/LHCC 99-5

[114] C. Pagliarone, A. Fernandez-Tellez: *Cosmic Ray Physics with ACORDE at LHC*, JPCS **110** (2008) 062021

[115] ALICE Collaboration: *Technical Design Report of the Time Of Flight System*, CERN/LHCC 2000-12

[116] ALICE Collaboration: *Technical Design Report of the High Multiplicity Particle identification Detector*, CERN/LHCC 98-19

[117] ALICE Collaboration: *ALICE Physics Performance Report I*, J. Phys. G: Nucl. Part. Phys. **30** (2004) 1517

[118] ALICE Collaboratio: *ALICE Physics Performance Report II*, J. Phys. G: Nucl. Part. Phys. **32** (2006) 1295

[119] R. Fruhwirt: *Application of Kalman filtering to track and vertex fitting*, Nucl. Inst. Meth. A**262** (1987) 444-450

[120] K. Aamodt, ..., **Renzhuo WAN**, ..., (ALICE collaboration): *Thansverse momentum spectra of charged particles in proton-proton collisions at* $\sqrt{s} = 900$ *GeV with ALICE at the LHC*, Phys. Lett. B **693**, 53 (2010)

[121] J. Alme et al.: *The ALICE TPC, a large 3-dimentional tracking device with fast readout for ultra-high multiplicity events*, Nucl. Instrum. Meth. A **622** (2010) 316

[122] K. Aamodt, ..., **Renzhuo WAN**, ..., (ALICE collaboration).: *Production of pions, kaons and protons in pp collisions at* $\sqrt{s} = 900\ GeV$ *with ALICE at the LHC*, hep-ex/1101.4110 (to be submitted to Euro. Phys. J. C.)

[123] D. C Zhou (for the ALICE Collaboration): *ALICE PHOton Spectrometer*, J. Phys. G: Nucl. Part. Phys. **34** (2007) S719-S723; talked at Quark Matter 2006, 13-20, Nov. 2006, Shanghai.

[124] D. V. Aleksandrov et al.: *A high resolution electromagnetic calorimeter based on lead-tungstate crystals*, Nucl. Instr. Meth. A**550** (2005) 169-184

[125] A. M. Blick et al.: *Charged Particle Veto Detector for the PHOS Spectrometer*, Internal Note/PHOS, ALICE 99-08

[126] Z. Yin and D. Zhou: *Performance of the ALICE PHOS Front-End Electronics*, HEP&NP, Vol. **30**, No. 12 (2006) 1165

[127] H. Muller et al.: *Trigger electronics for the ALICE PHOS detector*, Nucl. Instrum. Meth. A **518** (2004) 525

[128] ALICE Collaboration: *EMCAL Techinical Design Report*, CERN-LHCC-2008-014

[129] ALICE collaboration: *ALICE DAQ and ECS users guide*, ALICE-INT-2005-015

[130] S. Bagnasco, L Betev et. al. AliEn: *ALICE environment on the GRID*, J. Phys.: Conf. Ser. **119** (2008) 062012

[131] $http://aliweb.cern.ch/Offline/AliRoot/Releases.html$

[132] $http://root.cern.ch/drupal/$

[133] Yuri KHARLOV, Lamia BENHABIB, **Renzhuo WAN**: *Physics with photons in ALICE*, *POS*: *089* 2008LHC

[134] Sjostrand T., Mrenna S. and Skands P.: *PYTHIA 6.4 Physics and Manual* , arXiv: hep-ph/0603175

[135] **Renzhuo WAN**: π^0 *measurement with ALICE EM-calorimeters*, J. Phys.: Conf. Ser. 270 (2011) 012004

[136] https://aliceinfo.cern.ch/static/alirootnew/html/roothtml/AliGenBox.html

[137] CDF collaboration: *Measurement of the inclusive isolated prompt photon cross section in ppcollisions at* $\sqrt{s} = 1.96\ TeV$ *using the CDF detector*, Phys. Rev. D **80** (2009) 111106

[138] D0 collaboration: *Measurement of the Isolated Photon Cross Section in* $p-\bar{p}$ *Collisions at* $\sqrt{s} = 1.96\ TeV$, Phys. Lett. B **639** (2006) 151

[139] **Renzhuo WAN** Daicui ZHOU and Zhongbao YIN: *Track matching study from TPC to PHOS in ALICE*, China Physics C, Vol. **32**, No. 8 (2008) 620

[140] G. Conesa Balbastre et al.: *Detector performance studied and particles identification with PHOS*, ALICE-INT-2005-053

[141] G. Conesa Balbastre et al.: *Bayesian approach for the identification of particles detected in PHOS*, ALICE-INT-2005-016

[142] G. Conesa Balbastre et al.: *Prompt photon identification in the ALICE experiment: The isolation cut method* , Nucl. Instrum. Meth. A **580** (2007) 1446

[143] Ichou R. and d'Enterria D.: *Sensitivity of isolated photon production at TeV hadron colliders to the gluon distribution in the proton*, Phys. Rev. D**82**, 014015 (2010)

[144] http://aliceinfo.cern.ch/static/aliroot-pro/html/roothtml/AliPhysicsSelection.html

[145] https://twiki.cern.ch/twiki/bin/viewauth/ALICE/CaloQA

[146] http://indico.cern.ch/categoryDisplay.py?categId=1l8

[147] C. Tsallis: *Possible generalization of Boltzmann-Gibbs entropy*, J. Sta. Phys. **52** (1988) 479

[148] PHENIX collaboration: *Measurement of neutral mesons in p+p collisions at* $\sqrt{s} = 200\ GeV$ *and scaling properties of hadron production*, arXiv: 1005. 3674

[149] PHENIX collaboration: *Detailed study of high-*p_T *neutral pion suppression and azimuthal anisotropy in AuAu collisions at* $\sqrt{s_{NN}} = 200\ GeV$, Phys. Rev. C **76**, 034904 (2007)

[150] PHENIX collaboration: *Production of* ω *mesons at large transverse momenta in p+p and d+Au collisions at* $\sqrt{s}_{NN} = 200\ GeV$, Phys. Rev. C **75**, 051902 (2007)

[151] R. Witt (for the STAR collaboration): $< p_T >$ *systematics and* m_T *scaling*, arXiv: nucl.ex/0403021

[152] M. J. Tannenbaum: x_T *scaling of high* p_T π^0 *production in Au+Au collisions at RHIC*, DNP2002